

Fall 12-18-2020

# Thermo-Fluid Characterizations of the Powder-Bed Fusion Additive Manufacturing Processes using Laser and Electron Beam

M Shafiqur Rahman  
*University of New Orleans, New Orleans, mrahman3@uno.edu*

Follow this and additional works at: <https://scholarworks.uno.edu/td>



Part of the [Computer-Aided Engineering and Design Commons](#), [Fluid Dynamics Commons](#), [Heat Transfer, Combustion Commons](#), [Manufacturing Commons](#), and the [Metallurgy Commons](#)

---

## Recommended Citation

Rahman, M Shafiqur, "Thermo-Fluid Characterizations of the Powder-Bed Fusion Additive Manufacturing Processes using Laser and Electron Beam" (2020). *University of New Orleans Theses and Dissertations*. 2842.

<https://scholarworks.uno.edu/td/2842>

This Dissertation is protected by copyright and/or related rights. It has been brought to you by ScholarWorks@UNO with permission from the rights-holder(s). You are free to use this Dissertation in any way that is permitted by the copyright and related rights legislation that applies to your use. For other uses you need to obtain permission from the rights-holder(s) directly, unless additional rights are indicated by a Creative Commons license in the record and/or on the work itself.

This Dissertation has been accepted for inclusion in University of New Orleans Theses and Dissertations by an authorized administrator of ScholarWorks@UNO. For more information, please contact [scholarworks@uno.edu](mailto:scholarworks@uno.edu).

Thermo-Fluid Characterizations of the Powder-Bed Fusion Additive Manufacturing Processes  
using Laser and Electron Beam

A Dissertation

Submitted to the Graduate Faculty of the  
University of New Orleans  
in partial fulfillment of the  
requirements for the degree of

Doctor of Philosophy  
in  
Engineering and Applied Science  
Mechanical Engineering

by

M Shafiqur Rahman

B.S. Islamic University of Technology, 2011  
M.S. University of New Orleans, 2016

December, 2020

## **Dedication**

To

### **My Parents**

who brought me in this world, support me unconditionally, and taught me never to lose hope,

and

### **My Wife and Our Loving Son**

who are the inspirations of my life and the main reasons to have a blessed life.

## Acknowledgement

First, I would like to express my sincere gratitude to my advisor, Dr. Uttam K. Chakravarty, for allowing me to work on this topic. His continuous support, motivation, and guidance helped me to pursue my Ph.D. study and research. His sense of professionalism, enthusiasm, and in-depth knowledge inspired me not only to accomplish the dissertation but also to enhance my skills in analyzing and solving practical problems and writing technical reports, which have significantly contributed in my professional development.

I want to thank the rest of my dissertation committee members, Dr. Paul J. Schilling, Dr. Paul D. Herrington Dr. Kazim M. Akyuzlu, Dr. Martin Guillot, and Dr. Ashok Puri for their encouragement, insightful comments, critical questions, and helpful suggestions that improved my conceptions on my research topic. This research is supported by the National Science Foundation (NSF) through cooperative agreement OIA-1541079 and the Louisiana Board of Regents. The NSF project allowed me to be a part of the Louisiana Consortium for Innovation in Material and manufacturing (CIMM), where I contributed as a Graduate Student Researcher for five years. Through the CIMM, I was able to collaborate with Louisiana State University (LSU), for conducting experiments that significantly complement my Ph.D. work. I express my gratitude to Prof. Shengmin Guo, Department of Mechanical Engineering, LSU, and his students Congyuan Zeng and Wen Hao, for their collaboration and help in running experiments. I also thank my former labmates Pratik Sarker, Jose E Rubio, Iftekhar Riyad, Md Mosleh Uddin, and current labmate Mohammad Khairul Habib Pulok for the stimulating discussions, help in the experiments and software simulations, and for all the pleasant time we have had in the last five years. Especially, Mr. Pulok deserves an honorable mention as he was always there to help me in my academic and extracurricular activities. I am thankful to the Mechanical Engineering

Department and the University of New Orleans for giving me the opportunity to achieve my dream and for being a wonderful part of my life over the past six years.

I heartily thank my father, Mohammed Habibur Rahman Badal, and my mother, Aklima Jahan, who brought me in this world and supported me unanimously throughout my life. I thank my sisters and all my family members and friends for their support. Finally, I thank my wife Ferdousi Mojumder for being my soul mate, staying beside me in every will and woe, and making me a proud father by giving birth to our son Saihaan S. Rahman. I am thankful to God for the life I have been living.

## Table of Contents

List of Figures.....	vii
List of Tables.....	xi
Nomenclature.....	xii
Abstract.....	xvi
<b>Chapter 1 Introduction .....</b>	<b>1</b>
1.1 Powder-bed Fusion Additive Manufacturing.....	1
1.2 State of the Art .....	2
1.3 Motivation of the Work .....	5
1.4 Literature Review.....	7
1.5 Research Objectives and Highlights .....	11
<b>Chapter 2 Fundamentals of the Powder-Bed Fusion Processes.....</b>	<b>13</b>
2.1 Selective Laser Melting Process .....	13
2.2 Electron Beam Additive Manufacturing Process.....	15
2.3 EBAM versus SLM.....	18
2.4 Energy Absorption Mechanism .....	20
2.5 Methodology for Process Investigation .....	22
2.6 Concepts on Multiphysics Modeling .....	25
2.7 Established Functional Relationships .....	27
<b>Chapter 3 Material and Methods.....</b>	<b>29</b>
3.1 Material Modeling .....	29
3.2 Numerical Modeling .....	33
3.2.1 Configuration of the Physical Domain .....	34
3.2.2 Computational Domain.....	35
3.2.3 Mesh Convergence Study .....	37
3.2.4 Simulation Procedure.....	38
3.3 Experimental Analysis .....	39
<b>Chapter 4 Mathematical Model .....</b>	<b>42</b>
4.1 General Assumptions .....	42
4.2 Heat Source Modeling .....	42
4.3 Energy Density and Interaction Time .....	45
4.4 CFD Formulations .....	48
4.4.1 Boundary and Initial Conditions.....	51
4.5 Calculation of Viscosity.....	52
<b>Chapter 5 Results and Discussions .....</b>	<b>54</b>
5.1 Numerical Results.....	54
5.1.1 Simulation Results for the SLM Process .....	54
5.1.1.1 Variation of Thermal Properties .....	57
5.1.1.2 Melt-Pool Geometry .....	59
5.1.2 Simulation Results for the EBAM Process.....	61
5.1.2.1 Variation of Thermo-fluid Properties .....	61
5.1.2.2 Melt-Pool Geometry for EBAM .....	68

5.1.3 Comparison between the SLM and EBAM Processes.....	71
5.1.3.1 Variation of Thermal Properties .....	71
5.1.3.2 Melt-Pool Geometry .....	74
5.1.3.3 Heating and Cooling Rates .....	77
5.1.3.4 Velocity inside the Melt Pool .....	79
5.2 Experimental Results .....	81
5.2.1 Effects of Changing Laser Scanning Speeds .....	81
5.2.2 Effects of Changing Laser Power .....	82
5.2.3 Effects of Changing Laser Spot Size .....	84
Chapter 6 Model Validation.....	86
6.1 Validation with the Classical Stefan Problem of Melting .....	86
6.2 Experimental Validation for the SLM Model .....	89
6.3 Experimental Validation for the EBAM Model.....	93
6.4 Validation with a Lid Driven Cavity Problem.....	94
Chapter 7 Conclusions .....	97
7.1 Concluding Remarks.....	97
7.2 Proposed Future Work .....	99
References .....	101
Vita.....	111

## List of Figures

Figure 1.1: Market share of AM technology throughout the world.....	3
Figure 1.2: Worldwide annual expenditure on the production of AM parts.....	3
Figure 1.3: Research highlights .....	12
Figure 2.1: Schematic diagram of the SLM Process.....	14
Figure 2.2: A schematic view of the heat transfer and melt-pool evolution in SLM .....	15
Figure 2.3: Flow chart of the EBAM process .....	16
Figure 2.4: Electron beam melting systems schematic with scanning electron microscope view of Ti-6Al-4V powder (numbers denote the system components): (1) electron gun, (2) beam focus lens, (3) beam deflection coils, (4) powder cassettes, (5) powder layer rake, (6) build product, and (7) build table (lowered with each layer addition).....	17
Figure 2.5: Comparison between SLM and EBAM in terms of rating on a scale of ten .....	20
Figure 2.6: Laser or electron beam penetration in powder-bed .....	21
Figure 3.1: Scope of the study showing the analytical, numerical, and experimental methods ....	29
Figure 3.2: Temperature dependent thermal conductivity of Ti alloy powder .....	31
Figure 3.3: Temperature dependent specific heat of Ti alloy powder .....	31
Figure 3.4: Temperature dependent density of Ti alloy powder.....	31
Figure 3.5: Schematic of the SLM Process.....	33
Figure 3.6: Schematic of the EBAM Process .....	34
Figure 3.7: Physical domain of the 3-D model with laser or electron beam travel specifications	35
Figure 3.8: 3-D computational domain with structured mesh .....	36
Figure 3.9: 2-D views of the computational domains with initial and boundary conditions for the (a) SLM and (b) EBAM models .....	37
Figure 3.10: Convergence of the melt-pool temperature with the increase of degrees of freedom at $t = 0.009$ s.....	38
Figure 3.11: Schematic diagram of laser system setup.....	40
Figure 4.1: (a) Conical volumetric heat source and (b) heat flux for a beam power of 240 W ....	43
Figure 4.2: Comparison of the beam penetration functions for laser and electron beam .....	45
Figure 4.3: Conduction and keyhole modes for melt-pool evolution .....	46

Figure 4.4: Variation of heat density with electrical power at different efficiencies of the heat source .....	47
Figure 4.5: Temperature dependent viscosity of Ti-6Al-4V alloy .....	53
Figure 5.1: Keyhole mode confirmation for the laser melting of solid specimen .....	57
Figure 5.2: Contour plot for temperature (K) at the scanning path of the beam at $t = 0.016$ s.....	58
Figure 5.3: Contour plot for temperature (K) at the longitudinal section at $t = 0.016$ s .....	58
Figure 5.4: Contour plot for thermal conductivity (W/m-k) at the cross-section at $t = 0.016$ s ....	59
Figure 5.5: Melt-pool geometry for $26 \text{ J/mm}^3$ energy density and 1.212 ms laser interaction time where the left image is viewed from the bottom of the domain and the right one is viewed at the longitudinal section at $y = 7 \text{ mm}$ and $t = 0.016$ s .....	60
Figure 5.6: Simulated melt-pool width and depth at $58 \mu\text{m}$ spot size and 200 w laser power .....	60
Figure 5.7: (a) Modified geometry of the EBAM model, and (b) contour plot for temperature (K) at the scanning path of the beam at $t = 0.09$ s .....	62
Figure 5.8: Contour plot for temperature (K) at the longitudinal section at $t = 0.09$ s .....	63
Figure 5.9: Contour plot for temperature (K) at the cross-section at $t = 0.09$ s .....	63
Figure 5.10: Contour plot for density ( $\text{kg/m}^3$ ) at the longitudinal section at $t = 0.09$ s .....	64
Figure 5.11: Contour plot for density ( $\text{kg/m}^3$ ) at the cross-section at $t = 0.09$ s .....	64
Figure 5.12: Contour plot for thermal conductivity (W/m-K) at the longitudinal section at $t = 0.09$ s .....	65
Figure 5.13: Contour plot for specific heat (J/kg-K) at the longitudinal section at $t = 0.09$ s .....	66
Figure 5.14: Contour plot for enthalpy (J/kg) at the longitudinal section at $t = 0.09$ s .....	66
Figure 5.15: Contour plot for thermal conductivity (W/m-k) at the cross-section at $t = 0.09$ s ....	67
Figure 5.16: Contour plot for specific heat (J/kg-K) at the cross-section at $t = 0.09$ s .....	67
Figure 5.17: Contour plot for enthalpy (J/kg) at the cross-section at $t = 0.09$ s .....	68
Figure 5.18: The maximum length and width of the melt pool at $t = 0.09$ s as viewed from the top and bottom, respectively .....	69
Figure 5.19: The maximum depth of the melt pool at $t = 0.09$ s as viewed from the longitudinal section .....	69
Figure 5.20: Estimation of the melt pool size from the contour plot for temperature (K) on the scanning path of the beam at (a) 630 mm/s and (b) 930 mm/s .....	70

Figure 5.21: Variation of maximum width, depth, and length of the melt pool (mm) with the increase in the beam scanning speed (mm/s) at $t = 0.09$ s .....	71
Figure 5.22: Contour plots for temperature (K) at the top surface at $y = 7.5$ mm in the (a) SLM and (b) EBAM models .....	72
Figure 5.23: contour plots for temperature (K) at the cross-section at $y = 7.5$ mm in the SLM and EBAM models .....	72
Figure 5.24: contour plots for thermal conductivity (W/m.K) at the cross-section at $y = 7.5$ mm in the SLM and EBAM models.....	73
Figure 5.25: contour plots for enthalpy (J/kg) at the cross-section at $y = 7.5$ mm in the SLM and EBAM models .....	74
Figure 5.26: The maximum length and width (as viewed from the bottom) of the melt pool at $y = 7.5$ mm .....	75
Figure 5.27: The maximum depths of the melt pool at different powers of the heat source .....	76
Figure 5.28: The maximum depths of the melt pool at different scanning speeds of the heat source .....	77
Figure: 5.29: Variation of temperature with time at a fixed point during the (a) SLM and (b) EBAM processes.....	78
Figure 5.30: Heating and cooling rates versus time plots for the (a) SLM and (b) EBAM processes .....	78
Figure 5.31: Contour plots for velocity (m/s) at the longitudinal section at $y = 7.5$ mm in SLM and EBAM .....	79
Figure 5.32: Fluid flow patterns in the SLM model at (a) the longitudinal section, and (b) the cross-section for 300 mm/s scanning speed with 200 W power and $58 \mu\text{m}$ spot size.....	81
Figure 5.33: Ti-6Al-4V powder-bed specimen after laser scanning.....	82
Figure 5.34: SEM images showing the melt pool features of single tracks treated with varying laser scanning speeds - (a) 100 mm/s, (b) 300 mm/s, (c) 750 mm/s, and (d) 1000 mm/s. The white lines indicate the boundary between heat-affected zone and the substrate, while the red dashed line demonstrates the boundary of melt zone and heat-affected zone .....	83
Figure 5.35: SEM images showing the melt-pool features of single tracks treated with varying laser powers - (a) 200 W, (b) 150 W, and (c) 100 W. The white line indicates the boundary between heat-affected zone and the substrate, while the red dashed line demonstrates the boundary of melt zone and heat-affected zone .....	84
Figure 5.36: SEM images showing the melt pool features of single tracks treated with varying laser spot sizes - (a) $400 \mu\text{m}$ , (b) $300 \mu\text{m}$ , and (c) $200 \mu\text{m}$ . The white line indicates the boundary between heat-affected zone and the substrate, while the red dashed line demonstrates the boundary of melt zone and heat-affected zone .....	85

Figure 6.1: Schematic of the 1-D Stefan problem of solid-liquid phase change .....	86
Figure 6.2: Contour plots for liquid fraction in melting of pure Ti at two different times .....	88
Figure 6.3: Change in melt front position with respect to time for melting of pure Ti .....	88
Figure 6.4: Solid Ti-6Al-4V disk specimen after laser scanning.....	89
Figure 6.5: SEM images of the cross-sections of the single tracks on the solid Ti-6Al-4V specimen with different laser scanning speeds – (a) 100 mm/s, (b) 300 mm/s, (c) 750 mm/s, and (d) 1000 mm/s. The white lines indicate the boundary between heat-affected zone and the substrate, while the red dashed line demonstrates the boundary of melt zone and the heat-affected zone .....	90
Figure 6.6: Mesh convergence plot for the modified SLM model considering the variation of melt-pool temperature with the increase of degrees of freedom at $y = 6$ mm, and $t = 0.04$ s .....	91
Figure 6.7: Comparison of the experimental results for 100 mm/s scanning speed with the modeling results at $y = 6$ mm, and $t = 0.04$ s, showing (a) the SEM image of the microstructure, (b) the temperature contour, and (c) the liquid fraction contour .....	92
Figure 6.8: EBAM model validation by comparing the numerical results for (a) melt-pool width versus scanning speed, and (b) melt-pool depth versus scanning speed with the EBAM experimental results .....	94
Figure 6.9: (a) Physical domain of the square cavity, (b) velocity streamline for the benchmark case at $Re = 400$ , and (c) velocity streamline obtained from Fluent simulation at $Re = 400$ .....	95
Figure 6.10: Comparison of Fluent results with the benchmark case for (a) normalized $u$ , and (b) normalized $v$ velocities.....	96

## List of Tables

Table 2.1: Comparison between EBAM and SLM processes.....	19
Table 3.1: Chemical composition of Ti-6Al-4V (grade 5) as mass percentage.....	30
Table 3.2: Thermal properties of Ti-6Al-4V used as user defined functions .....	32
Table 3.3: A sample set of solver settings in Fluent .....	39
Table 3.4: Packing density of Ti-6Al-4V powders.....	40
Table 5.1: List of the SLM simulation parameters .....	55
Table 5.2: Different laser irradiation conditions for the powder layer thickness of 70 $\mu\text{m}$ .....	55
Table 5.3: Thermophysical parameters for the keyhole mode calculation .....	56
Table 5.4: List of the EBAM simulation parameters.....	61
Table 5.5: Comparison of the melt-pool dimensions at $y = 7.5 \text{ mm}$ .....	75
Table 6.1: List of the simulation parameters for Ti melting.....	87
Table 6.2: Comparison between analytical and numerical results for temperature .....	89
Table 6.3: Melt-pool width and depth at 100 mm/s scanning speed .....	93

## Nomenclature

$A$	absorbance
$A_w$	atomic weight, g/mol
$a$	absorption coefficient, $1/\mu\text{m}$
$B$	a computational constant to avoid division by zero
$C$	a constant for viscosity calculation
$C_M$	a constant regarding mushy zone morphology
$c_p$	specific heat capacity, J/kg-K
$c_{p,l}$	specific heat capacity of liquid material, J/kg-K
$E$	activation energy, kcal/mol
$E_D$	energy density of the heat source, J/mm <sup>3</sup>
$f_L$	liquid fraction
$g_z$	gravitational acceleration, m/s <sup>2</sup>
$H$	total enthalpy, J/kg
$H_S$	the Gaussian heat source
$h$	convective heat transfer coefficient, W/m <sup>2</sup> -K
$I_b$	electron beam current, mA
$I_Z$	penetration function
$k$	effective thermal conductivity, W/m-K
$k_l$	thermal conductivity of liquid material, W/m-K
$L_f$	latent heat of fusion, kJ/K
$l_t$	powder layer thickness, mm or $\mu\text{m}$

$P$	pressure, Pa
$P_H$	power of the heat source, W
$\dot{Q}'''(x, y, z, t)$	volumetric heat flux, W/m <sup>3</sup>
$R$	molar gas constant, kcal/mol-K
$S$	penetration depth, $\mu\text{m}$
$S_H$	remaining source terms in the heat equation, W/m <sup>3</sup>
$S_L$	optical penetration depth of laser, $\mu\text{m}$
$S_E$	optical penetration depth of electron beam, $\mu\text{m}$
$Ste$	Stefan number
$s$	melt front position with respect to time
$T$	temperature, K
$T_L$	liquidus temperature, K
$T_m$	melting temperature, K
$T_{preheat}$	preheat temperature, K
$T_S$	solidus temperature, K
$T_{ref}$	reference temperature, K
$T_w$	wall temperature, K
$t$	time, s
$u, v, w$	velocity components in the $x$ -, $y$ -, and $z$ -directions, respectively, m/s
$u_i, u_j$	velocity along the Cartesian coordinates, m/s
$V$	acceleration voltage of the electron beam, kV
$V_m$	atomic volume, m <sup>3</sup> /mol
$v_s$	beam scanning speed, mm/s

$x_i$	distance along the Cartesian coordinates, mm
$x_s$	instantaneous position of heat source in the $x$ -direction
$y_s$	instantaneous position of heat source in the $y$ -direction
$z$	distance in the direction of penetration, mm

## Greek Symbols

$\alpha_l$	thermal diffusivity of liquid, $m^2/s$
$\beta_{ref}$	coefficient of volume expansion at the reference temperature, $1/K$
$\varepsilon$	emissivity
$\eta$	efficiency of laser or electron beam
$\lambda$	parameter in interfacial melt front equation
$\mu$	absolute viscosity, $N.s/m^2$ or $Pa.s$
$\mu_m$	viscosity of liquid metal, $N.s/m^2$ or $Pa.s$
$\sigma$	Stefan-Boltzmann constant, $W/m^2-K^4$
$\sigma_T$	temperature coefficient of surface tension, $N/m-K$
$\tau_{xz}$	Marangoni shear stress due to the $x$ component of velocity, $N/m^2$
$\tau_{yz}$	Marangoni shear stress due to the $y$ components of velocity, $N/m^2$
$\rho$	density of the material, $kg/m^3$
$\rho_l$	density of liquid, $kg/m^3$
$\rho_{ref}$	density of liquid at the reference temperature, $kg/m^3$
$\Phi$	laser or electron beam diameter, mm
$\Phi_V$	viscous dissipation term

## Abbreviations

AM	Additive Manufacturing
CFD	Computational Fluid Dynamics
EBAM	Electron Beam powder-bed fusion
FD	Finite Difference
FE	Finite Element
FV	Finite Volume
HAZ	Heat Affected Zone
SLM	Laser powder-bed fusion
SEM	Scanning Electron Microscope
PBF	Powder-Bed Fusion
PCM	Phase Change Material
UDF	User-Defined Functions

## Abstract

The powder-bed fusion (PBF) process is a subdivision of Additive Manufacturing (AM) technology where a heat source at a controlled speed selectively fuses regions of a powder-bed material to form three-dimensional (3-D) parts. Two of the most effective PBF processes are selective laser melting (SLM) and electron beam additive manufacturing (EBAM), which can fabricate full-density metallic parts in a layer-by-layer fashion. In this study, thermal behavior and melt-pool dynamics in the PBF process are investigated by developing 3-D multiphysics-based thermo-fluid models for both SLM and EBAM, containing Ti-6Al-4V alloy as a powder-bed material. The laser and electron beams are modeled as conical volumetric heat sources having the Gaussian distribution. The temperature-dependent properties of Ti-6Al-4V and the heat source parameters are incorporated in the models as the user-defined functions. The melt-pool geometry and its thermo-fluid behavior are investigated numerically using computational fluid dynamics, and results for temperature profile, variation in thermo-physical properties, the melt-pool velocity and geometry, and cooling rate are obtained under various heat source specifications. The modeling results for SLM and EBAM under the same irradiation conditions are compared to describe their deterministic features to be considered for industrial applications. The comparison shows that under the same energy density and beam interaction time, the SLM process gives a smaller melt-pool volume but a faster average cooling rate than those in the EBAM process. The thermo-fluid models are validated by comparing the simulation results for the melt-pool geometry with experimental results and resembling the numerical melt-front position with the analytical solution for the classical Stephan problem of melting of a phase-change material.

**Keywords:** Powder-bed fusion, SLM, EBAM, CFD, Ti-6Al-4V, Fluent, melt pool, cooling rate

# Chapter 1

## Introduction

Additive manufacturing (AM), a technology of building three-dimensional (3-D) objects by adding layer-upon-layer of materials ranging from plastics to metals and composites, has led to tremendous flexibility in the design and manufacturing of materials with tailored properties. In recent years, advancements in metal AM technology based on the consolidation process of the commercially available atomized metallic or alloyed powders has been enhancing the capability of AM from rapid prototyping to direct digital manufacturing of functional engineering components. It has been recognized as a progressive and effective 3-D microfabrication technology during the two decades of its evolution [1, 2]. AM technologies for 3-D microcomponents play a vital role in the development of very functional and sophisticated applications such as biochips, microelectromechanical systems (MEMS), microfluidic devices, and photonic crystals. A common background of these manufacturing technologies is that they are undergoing a rapid evolution from a welding-based or rapid prototyping background to customized manufacturing processes, suited to low-volume production of components over a wide range of applications in the aerospace, automotive, and medical sectors. Laconically, AM processes are hailed as an interruptive or step-change technology, opening the freedom of design space from computer-aided designs (CAD) to the net-shape finished products by simply pressing a button.

### 1.1 Powder-bed Fusion Additive Manufacturing

Powder-bed fusion (PBF) process is a relatively new but very effective AM technology that involves layer-by-layer fabrication of metals and non-metals at various scales with the

application of a moving heat source. The conventional manufacturing technologies (e.g., casting and forging) used for fabricating medical implants and components for automotive, aerospace, and space applications, constrain the customization of complex geometries, and consume a significant amount of material and time. The PBF process overcomes these limitations by providing the advantage of cost-effective customization with reduced assembly [2] and allows convenient processing of a wide range of materials, including metals and the alloys of titanium, copper, nickel, iron, aluminum, and chromium. The PBF processed parts show better corrosion resistance, less oxidation, and smaller heat affected zone as compared to the conventionally manufactured parts, which ultimately makes the PBF process a superior AM technology in the present era.

## **1.2 State of the Art**

From the perspective of increased competitiveness, AM offers lower cost components, more flexibility in customization, and more rapid product development to the manufacturing industry. AM technology has shown a significant impact on both the environment and sustainable manufacturing, with large waste-reductions in material and highly intricate and integrated components with room for optimized improvements (e.g., light weight and improved heat transfer characteristics). That is why, United States continues to lead the industrialization of AM over the last two decades [3] with a significant market share as shown in Fig.1.1.

The market for the metal AM technology will keep experiencing a trend in the following decade too [3]. Studies by the industrialists show that the metal AM market will worth \$5.51 billion by 2027 with a compound annual growth rate of 27.8% from 2020 to 2027. Figure 1.2 shows the data for the money spent on the final AM parts annually by the industries worldwide as published in the Wohlers Report 2020 [4].

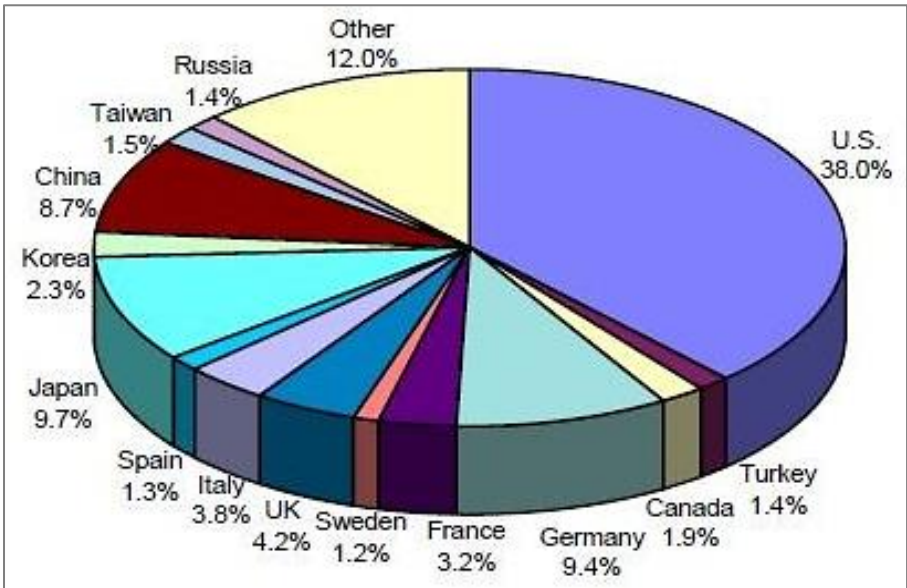


Figure 1.1: Market share of AM technology throughout the world [3]

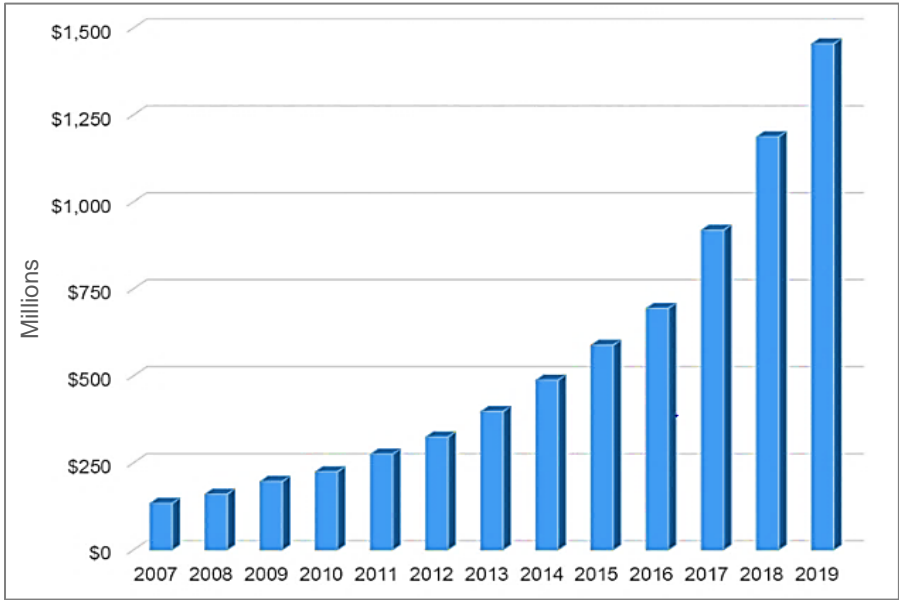


Figure 1.2: Worldwide annual expenditure on the production of AM parts [4]

The key advantages of AM technology when compared to the conventional techniques, are mentioned below.

- (i) High-speed manufacturing: AM allows a quick or sudden change in design and makes the lead time faster than that in conventional techniques.
- (ii) Flexibility of part geometry: Unlike the conventional processes, AM can produce parts of almost any desired shape and can overcome the geometrical constraints.
- (iii) Savings in materials and costs: In an AM technique, the material is added, not subtracted [2]. The part is obtained directly from its 3-D CAD model, which allows automation and digital interfaces, making it almost free from human errors.
- (iv) Full-density final parts and cellular components: AM allows the fabrication of free-form enclosed structures. AM technologies are capable of manufacturing free-form channels as well as different forms of metamaterial and lattice-structured material.

The raw materials for metal AM (which are either metal or alloy) usually come under powder state. Different alloys are widely studied as powder-bed material as they are very productive in AM technology. Titanium (Ti) and titanium alloys (e.g., Ti-6Al-4V) are materials with outstanding mechanical properties such as low density, high strengths, good chemical resistance, and excellent biocompatibility. The combination of these properties in a special structure has many potential applications in the areas of medical, aerospace, aeronautics, and automotive systems. A high energy heat source is required to melt the metallic or alloy powder at the targeted zones of the powder bed. Based on the heat source facility, two different PBF techniques are available for 3-D metallic or alloy parts:

1. Laser-based technologies, and
2. Electron beam-based technologies.

According to the terminology formulated by ASTM International, the relevant categories which employ these techniques of manufacturing are powder-bed fusion (PBF) and directed

energy deposition (DED) [5]. Examples of some popular AM technologies are stereolithography, binder jetting, fused deposition modeling (FDM), direct metal laser sintering (DMLS), selective laser sintering (SLS), selective laser melting (SLM), and electron beam additive manufacturing (EBAM), where the last four belong to the category of PBF technique.

Although the PBF process thrives in the current AM industry, optimizing the process parameters and controlling the phase formation, melt-pool dynamics, powder properties, surface roughness, and mechanical properties of the material are extremely challenging yet crucial for maximizing its benefit as a superior manufacturing technology. Therefore, extensive research on the PBF process, including analytical, experimental, and numerical approaches, is required to address the challenges and overcome the limitations.

### **1.3 Motivation of the Work**

SLM and EBAM have the potential to offer innovative solutions to many challenges and difficulties faced in the manufacturing industry. The applications of SLM and EBAM in manufacturing industry as the latest AM technology provides the following benefits:

- (i) Ample opportunity for customization,
- (ii) Lower lead time in manufacturing,
- (iii) Enhanced mechanical properties and durability of products,
- (iv) Elimination of waste or scrap,
- (v) Excellent energy efficiency,
- (vi) Low operating costs in manufacturing complex geometries, and
- (vii) Enormous prospect in future AM market size.

Despite extensive advantages over conventional technologies, SLM and EBAM still exhibit several deficiencies in obtaining desirable metallurgical behavior, part accuracy, reliability, and quality consistency [6]. The complex physics of the process has neither been fully understood, nor has the process metrology (e.g., temperature) been thoroughly studied, thus hindering part quality, efficient process development, and process optimizations for better usage of them. Hence, accurate physical models addressing the heat source and heat transfer mechanisms are required to investigate thermal phenomena and determine appropriate process parameters based on process variables. As the melt-pool geometry strongly affects the build part microstructures, a method to control the melt-pool geometry as a function of temperature is of great interest to the researchers. All these facts define the motivation of this research, and thereby, significant concentration is subjected to the understanding of the correlation among the process parameters, melt-pool geometry, and part microstructures, which can offer useful information about determining the performance and efficiency of these processes.

Studies on the SLM and EBAM processes indicate that researchers, over the years, have focused heavily on individual investigations rather than the comparison between the two methods [5–10]. However, a comparative study of the process parameters, melt-pool geometry, and part microstructures can offer more valuable information than the individual studies and can facilitate the characterization of the pros and cons of the SLM and EBAM processes evidently [11–17]. Robust numerical modeling characterizing the thermo-fluid properties along with the experimental validation can be the most effective means to conduct a strong comparative analysis between the SLM and EBAM processes [18]. The outcome of this comparative study can provide a vivid picture to select the appropriate technology to be commercialized in manufacturing industries [18].

## 1.4 Literature Review

With an incessant growth of interest in AM technologies, there have been a surge of research activities in the AM field. Several efforts have been made to investigate the behavior of the SLM and EBAM processes which can be classified into three main categories including experimentation, numerical modeling, and analytical study. However, controlling the phase formation, melt-pool dynamics, surface roughness, and mechanical properties of the material in the SLM and EBAM processes requires optimization of the process parameters which is extremely challenging. Most of the studies emphasize the application-based experimental analyses such as build-part microstructure, morphological characteristics, powder metallurgy, and mechanical properties of the material [5, 6]. A number of useful reviews on the AM process behavior were published in the past few years. Everton *et al.* [6] reviewed the inspection methodologies compatible with AM processes and explored the identification of typical material discontinuities and failure criteria. Fottovvati *et al.* [7] provided excellent reviews of keyhole and melt-pool behavior during deep penetration welding which are also largely applicable to AM. More reviews on the PBF process behavior, material characterizations, and modeling strategies were presented by Debroy *et al.* [8], Sames *et al.* [9], and Bikas *et al.* [10]. Researchers have also focused on the comparison between the laser-based and electron-beam based AM processes which are evinced by the reviews of Sing *et al.* [11], Zhao *et al.* [12], Gong *et al.* [13], Rafi *et al.* [14], Chastand *et al.* [15], Wysocki *et al.* [16], and Gokuldoss *et al.* [17]. However, a comparison between the SLM and EBAM based the thermo-fluid characterizations was not outlined in those studies.

Before making the comparison between the SLM and EBAM processes, it is important to investigate the thermo-physical phenomena by reviewing research works on the welding and AM

techniques using laser [19–34] and electron beam [35–63] separately. The studies covered both numerical and experimental analyses where some researchers concentrated on experimental methods while some highlighted the numerical modeling. In general, the heat source is modeled as a conical volumetric heat flux due to the resultant keyhole formed by the incident laser or electron beam under the surface of the workpiece. Modeling of SLM requires incorporation of convection with the inert gas environment at room temperature [19]. While studying the laser-based PBF process, Qi *et al.* [20] developed a self-consistent numerical model for studying the heat transfer, phase change, and fluid flow within the melt pool. Cho *et al.* [21] studied the melt-pool dynamics during laser beam welding (LBW) of structural steel using 3-D numerical simulation while Moraitis and Labeas [22] investigated residual stresses and distortions of aluminum in the LBW process using thermo-mechanical numerical model based on the keyhole theory. Wang *et al.* [23] developed a 3-D computational procedure to measure the real-time melt-pool shape and obtained the distribution of temperature in laser keyhole welding. More works on laser-based methods, covering both numerical and experimental analyses, were presented by Lankalapalli *et al.* [24], Roberts *et al.* [25], Yang *et al.* [26], Andreotta *et al.* [27], Sadowski *et al.* [28], Ladani *et al.* [29, 30], Ahsan and Ladani [31], Riedlbauer *et al.* [32], Wen *et al.* [33], Wang *et al.* [34], Rai *et al.* [35], Raplee *et al.* [36], Li *et al.* [37], Yuan and Gu [38], and Le *et al.* [39]. In contrast to the laser-based technique, the electron beam method requires preheating of the material at high vacuum that needs to be characterized accurately in the numerical model. Studies on electron beam PBF, especially, numerical modeling of heat transfer and fluid flow in the EBAM process were conducted by many researchers, including Roy [40], Liu *et al.* [41], Lacki and Adamus [42], Shen and Chou [43], Gong *et al.* [44], Murr *et al.* [45], Gong *et al.* [46], Galati *et al.* [47], Rouquette *et al.* [48], Attar [49], Biamino *et al.* [50], Cheng *et al.* [51], Chen *et*

*al.* [52], Zah and Lutzmann [53], Rai *et al.* [54, 55], Chahine *et al.* [56], Jamshidinia *et al.* [57–59], and Rahman *et al.* [60–65]. All these studies suggest that numerical modeling of heat transfer and fluid flow in the melt pool can provide helpful quantitative information about the part geometry, thermal cycle, cooling rate, and solidification process.

Studies show that understanding the correlation between the PBF process parameters and the process outcomes without costly experimentation requires comprehensive numerical modeling. Development of a robust numerical model for SLM or EBAM requires the concepts of complex heat transport, material phase change, and intricate relations among the thermal, mechanical, and metallurgical phenomena [18] which make it extremely challenging to implement. While developing a robust thermal model, it is important to find a convenient numerical scheme that can accurately estimate the melt-pool geometry and determine the temperature distribution in the build part by taking into considerations of the heat source parameters and material properties. Many researchers developed thermal models using finite difference (FD) [20] and finite element (FE) methods at various length and time scales [25–32, 41–47]. Traditionally, the FE models dominate the number of numerical techniques implemented by the researchers because of its accuracy and ability to handle complex geometry while incorporating the Gaussian heat source, porosity of the powder, and temperature dependent thermal properties to simulate the transient heat transfer in the PBF processes [25, 26, 51, 52]. Recent progress on FE analyses to investigate the effect of process parameters in PBF can be attributed to the studies of Andreotta *et al.* [27], Sadowski *et al.* [28], Ladani *et al.* [29, 30], Ahsan and Ladani [31], Riedlbauer *et al.* [32], and Galati *et al.* [47]. All these studies included numerical and/or experimental analyses of either the SLM or EBAM process, but the comparison

between the two processes, which could facilitate the selection of the suitable one in industry, was not documented precisely.

Numerical studies showed that computational fluid dynamics (CFD) models could influence the modeling results by adding the features of fluid flow. Thermo-fluid models based on CFD and finite volume (FV) methods become more effective than FE thermal models when fluid flow and heat convection in the melt pool are dominant factors in the process outcomes [33]. Studies show that thermo-fluid models using CFD can effectively provide quantitative information about the melt-pool geometry, velocity, thermal history (including heating and cooling rates), and properties of solidification with the same accuracy as the FE models [33, 34]. Wang *et al.* [33] developed a 3-D volume-of-fluid method to measure the real-time melt-pool shape and obtained the distribution of temperature in laser keyhole welding. Rai *et al.* [35] and Li *et al.* [37] showed that fluid convection inside the melt pool resulted in an increase in heat transfer and gave better correlation between numerical and experimental results of the melt-pool geometry. Yuan and Gu [38] used FV simulation and laser experiments to investigate the melt-pool evolution and thermal behavior of TiC/AlSi10Mg powder-bed in SLM process. Le *et al.* [39] developed a 3-D CFD-based model to investigate the heat transfer and melt-flow dynamics in the SLM process with IN718 powder-bed. Attar [49] developed a 2-D lattice Boltzmann model to investigate the melting and solidification of a randomly packed powder bed under the irradiation of a Gaussian electron beam. Rai *et al.* [54, 55] again used the CFD modeling to investigate the heat transfer and fluid flow during electron beam melting. Chahine [56] used CFD to study the effects of the electron beam current and exposure time on the temperature distribution and fluid flow of a melt spot. Jamshidinia *et al.* [57–59] developed 3-D thermal and fluid flow models of EBAM, where the influence of fluid convection on the melt-pool geometry

was investigated and the effects of changing process parameters were studied numerically and experimentally. Rahman *et al.* [60–67] conducted CFD-based thermo-fluid modeling of Ti-6Al-4V melt pool to study the thermal features and melt-pool dynamics in PBF processes. However, the comparison between SLM and EBAM processes based on thermo-fluid modeling is yet to be studied rigorously.

## 1.5 Research Objectives and Highlights

A comprehensive study on the process parameters, the geometry of the melt pool, and part microstructures can provide helpful information to characterize the performance and efficiency of the PBF processes. However, instead of individual studies, a comparative study offers more valuable information to select the appropriate technology in AM industry. Therefore, the objectives of the research are listed below.

- i) To investigate the thermal and fluid flow behavior of the Ti-6Al-4V melt pool formed in both the SLM and EBAM process and compare the results to establish a standard to choose the appropriate process for advanced manufacturing.
- ii) To develop 3-D thermo-fluid models for both SLM and EBAM incorporating the thermo-physical properties of Ti-6Al-4V and investigate the effects of the laser and electron beam parameters on temperature distribution, melt-pool geometry, melt-pool dynamics, and the criteria for melting and solidification involved in these processes.
- iii) To develop mathematical formulations using the concepts of CFD, phase change, and heat transfer.
- iv) To design and create user defined functions for the Gaussian heat source and temperature-dependent properties for the SLM and EBAM models and run the simulations with appropriate settings.

- v) To validate the numerical models by comparing the numerical results with the experimental and analytical results.

The outcomes of this research have been reported to the NSF and Louisiana Board of Regents every year since 2016, showing the progress made and the milestone achieved in each reporting period [65–67]. The highlight of the research under a strategic framework is illustrated in Fig. 1.3. The overall study, combining analytical, numerical, and experimental analyses, suggests that the experimentally-validated multiphysics CFD model is a cost-effective and reliable tool for predicting the heat transfer and melt-pool evolution of any materials in the powder-bed fusion AM processes.

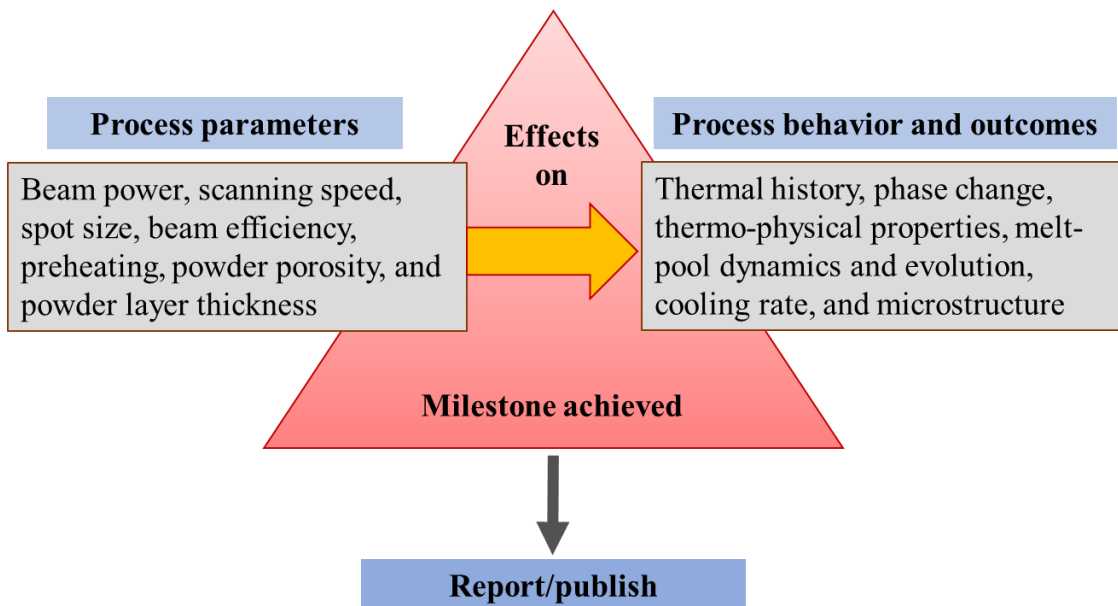


Figure 1.3: Research highlights

## Chapter 2

### Fundamentals of the Powder-Bed Fusion Process

Powder-Bed Fusion Process implements a rapid-prototyping strategy where the thermal energy of a computer-controlled heat source is used for selective melting and sintering of regions of a powder-bed [1]. Two of the most common types of powder-bed fusion processes are the selective laser melting (SLM) and electron beam additive manufacturing (EBAM) which have brought about a revolution in the field of metal additive manufacturing (AM) technology. The SLM process uses finely focused monochromatic coherent photons, i.e., laser while the EBAM process uses a beam of electrons as the heat source for melting the powder bed. This chapter represents the description of the fundamentals in these two PBF processes with detailed concepts on the methods and physics involved.

#### 2.1 Selective Laser Melting Process

Selective laser melting, also known as the laser powder-bed fusion (L-PBF) process, is a newly established branch of AM that can produce complex shaped metal components from powder materials [10–13]. In this process, the thermal energy of laser (i.e., monochromatic coherent photons) selectively fuses regions of a powder-bed on top of a substrate [63]. The 3-D part to be fabricated is mathematically sliced into thin layers at the beginning according to the object's computer-aided design (CAD) model. Then the final part is created by selective fusion and consolidation of the deposited powder layers with a moving laser heat source in a layer-by-layer manner. The melting of a selected region of the powder bed forms a melt pool which is rapidly cooled and consolidated in a convective medium, usually in an inert gas environment (such as argon). A process schematic of the SLM process is shown in Fig. 2.1. Once a layer of an

object is completed, the building platform is lowered, and more powder is spread over (usually, rolled on) the build area for a new scan. The process ends with a postprocessing step of removing all the unbound powder [2] from the fabricated object. The processing parameters in SLM can be broadly classified into four main groups, namely: (1) the laser parameters (e.g., the laser spot size and laser power); (2) the scanning strategy (e.g., the scanning speed and scanning pattern); (3) the powder bed parameters (e.g., the powder layer thickness and powder particle size distribution); and (4) the thermal parameters (e.g., the preheat temperature) [39].

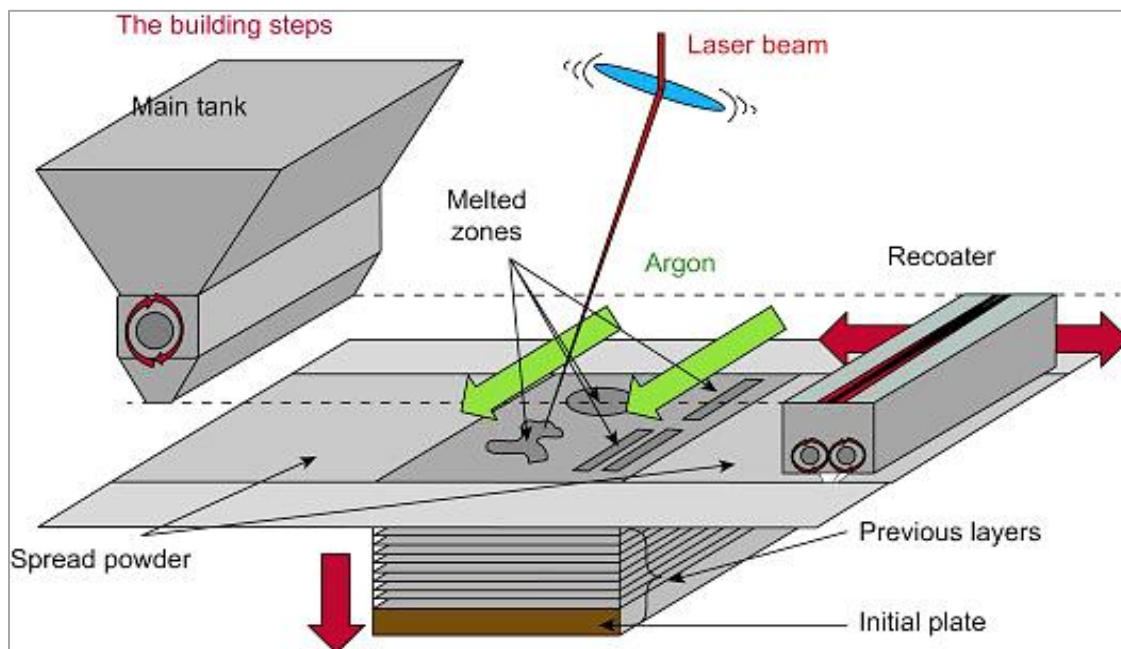


Figure 2.1: Schematic diagram of the SLM Process [68]

During the SLM process, heat transfer mechanism mainly includes heat radiation to powder layer from laser beam, heat conduction among powder particles, and heat convection between powder bed and ambient atmosphere. The three coupled heat transfer mechanisms make the thermal behavior during the SLM process become very complex. The physical, chemical, and metallurgical phenomena during the interaction of the moving Gaussian laser heat source and

powder-bed affect the heat transfer and melt-pool evolution in the SLM process. The schematic of the complex phenomena during the laser scanning is depicted in Fig. 2.2.

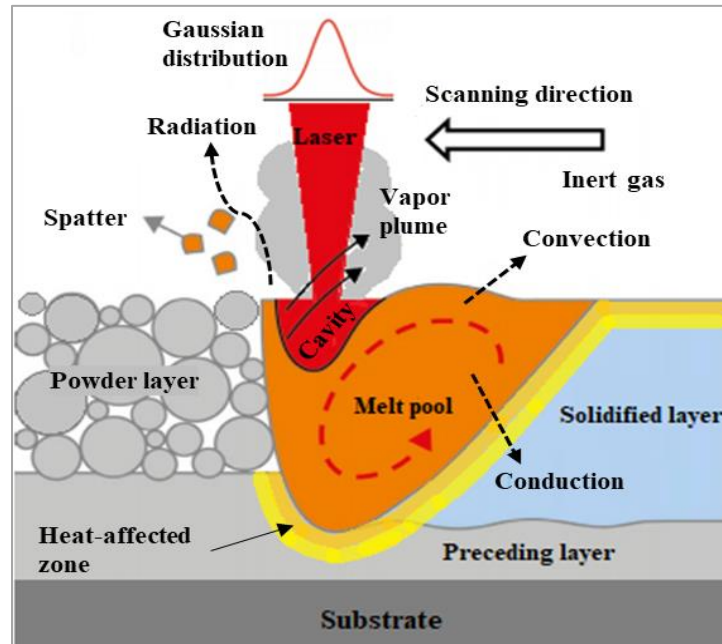


Figure 2.2: A schematic view of the heat transfer and melt-pool evolution in SLM [65, 69]

With the protective inert gas fed into the sealed building chamber, the interior oxygen content can be reduced below a required standard. Under this condition, the formation of oxide films on the surfaces of the melt can be alleviated. However, the laser–powder interaction is so quick that the powder materials undergo a solid–liquid–solid transition in a very short time, which results in the large temperature gradient and thermal stress; and may cause cracks in the final products.

## 2.2 Electron Beam Additive Manufacturing Process

EBAM was invented in 2002 by ARCAM AB in Sweden [62]. As compared to the SLM process, EBAM provides faster build-up due to higher beam efficiency, faster scanning speed, and minimal reflection. The power spectrum of electron beam has a very wide range that makes

it possible to melt almost all types of materials. However, metallic alloy powders (especially, high entropy alloys such as Ti-6Al-4V) are applied as powder-bed materials for the EBAM process in most cases. In building each layer, the process starts with processing the electronic data, usually generated from a CAD software. The process flow chart of EBAM [40] is illustrated in Fig. 2.3.

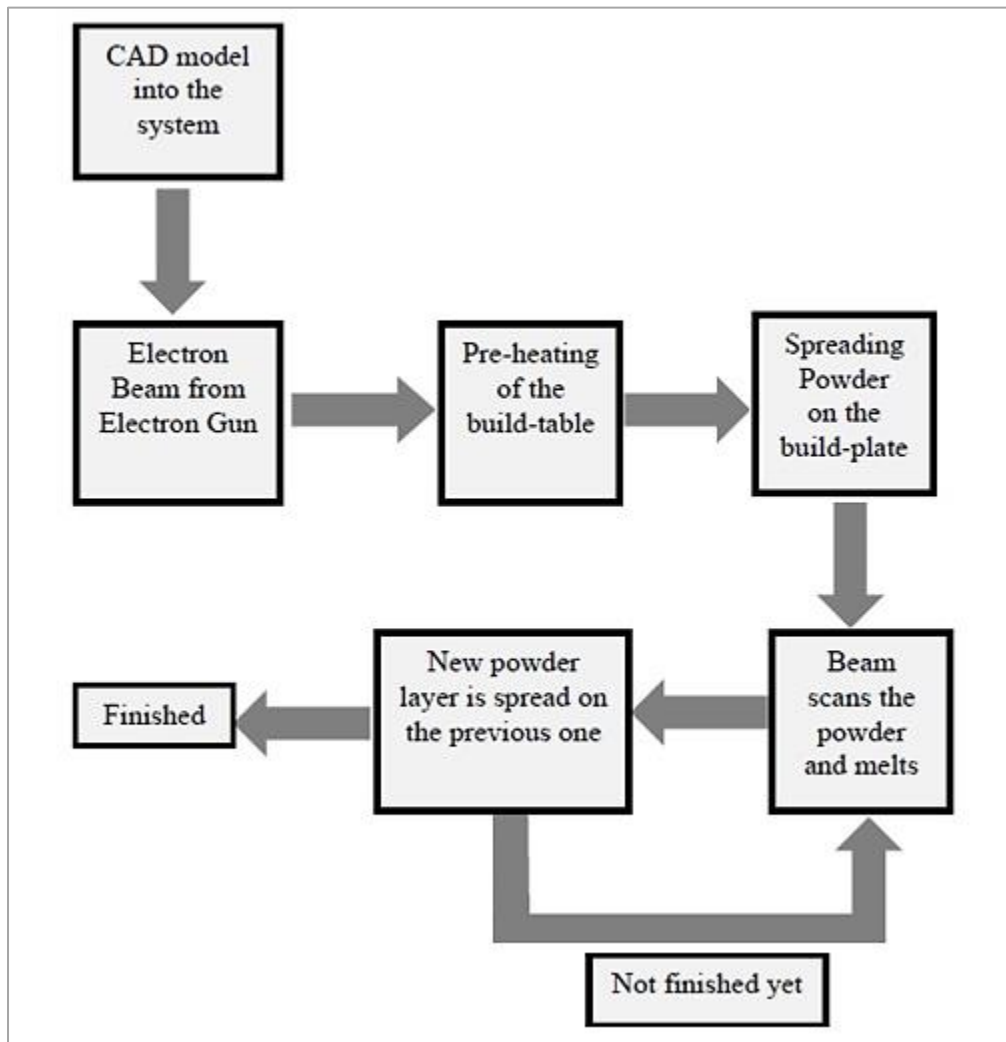


Figure 2.3: Flow chart of the EBAM process [40]

In the first step, a compatible build file needs to be created. A 3-D CAD model can be sliced into several layers by using the software that accompanies the EBAM machine. The

buildup file provides the required process information including the dimensions. Electrons are produced by heating the tungsten filament. The high voltage potential applied between the anode and cathode accelerates the speed of electrons. In the next step, electrons pass through three coils which increase the beam intensity and stir the beam. The kinetic energy of electrons is transformed into heat upon striking the target material. The emitting electrons start to preheat the substrate (stainless steel plate) to a specific temperature. The preheating of the substrate serves multiple purposes, such as minimizing the thermal gradient and avoiding the powder spreading phenomenon. When the desired preheating temperature is reached, the powder rake applies the first powder layer on the substrate. The thin layer of powder is exposed to the electron beam that melts down the Ti-6Al-4V powder. The process schematic is shown in Fig. 2.4 [45].

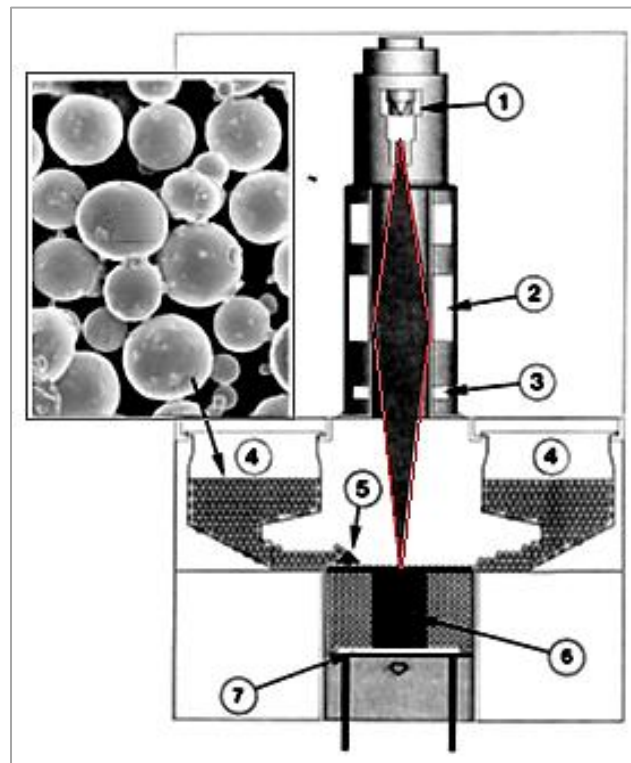


Figure 2.4: Electron beam melting systems schematic with scanning electron microscope view of Ti-6Al-4V powder (numbers denote the system components): (1) electron gun, (2) beam focus lens, (3) beam deflection coils, (4) powder cassettes, (5) powder layer rake, (6) build product, and (7) build table (lowered with each layer addition) [45]

In building each layer, the process involves powder spreading, preheating, and melting. In powder spreading, a metal rake is applied to uniformly distribute one layer of powder. Then, preheating is done to reach a high temperature across the entire powder-bed surface using a single beam at a high speed, with multi-pass scans. After that, contour, or hatch-melting stages take place with the electron beam scanning at a lower speed. Once a layer is built, the system is cooled down and then the entire powder-bed is retrieved from the machine for cleaning (usually by a blasting process) and post-processing. The typical pressure of residual gases in an EBAM machine is  $10^{-1}$  Pa in the vacuum chamber and  $10^{-3}$  Pa in the electron gun [38]. During the melting process, low pressure of inert helium gas ( $10^{-1}$  Pa) is added to the vacuum chamber to avoid the build-up of electrical charges in powder. When all layers are completed, the built part is cooled inside the process chamber, which is then filled up with helium to assist cooling. Providing rapid self-cooling criteria for the liquid melt pool, the EBAM can produce fully melted metallic parts with fine microstructures and superior mechanical properties through computer-controlled machines. Because of radiation from electrons, the process observation is not as accessible as other AM technologies, only through a leaded-glass viewport. Therefore, what exactly happens inside the build chamber is difficult to perceive when compared to other AM processes.

### **2.3 EBAM versus SLM**

In EBAM, a finely focused beam of electrons is used, while in SLM, monochromatic coherent photons, i.e., the laser is used for melting the powder layers. In both cases, the kinetic energy of the electrons or photons is turned into heat energy when they scan the powder layer. Table 2.1 shows the advantages and disadvantages of both processes in the context of industrial applications.

**Table 2.1: Comparison between EBAM and SLM processes [18, 70]**

<b>Features</b>	<b>EBAM</b>	<b>SLM</b>
<b>Penetration and depth to width ratio</b>	60 kV 6 kW beam power gives over 20 mm penetration at regular working condition	Solid state lasers (e.g., Nd:YAG) have lower power resulting in low penetration
	Weld depth to width ratio up to 40:1	Weld depth to width ratio 10:1
<b>High speed</b>	High speed deep penetration welds possible	High welding speeds achievable but lacks penetration
<b>Process Automation</b>	Can be highly automated with the allowance of chamber evacuation time. Typical cycle times in automotive industry are around 40 seconds per component.	Can be highly automated with production rates higher than that for EBAM as there is no evacuation time for chamber (non-vacuum process)
<b>Component size restriction</b>	Component size is restricted by the size of vacuum chamber. Chamber volumes are kept to a minimum to reduce evacuation times	Not restricted by component size. Nd:YAG fibre optic delivery systems allows remote welding from the power source
<b>Weld quality</b>	High quality weld due to inert atmosphere, very stable and repeatable	Some porosity is normally found as the shield gas does not eliminate air from the weld area entirely
	Deep penetration welds on a wide variety of materials possible	Inferior weld quality when subjected to deep penetration but surface finish is better than EBAM
<b>Vacuum Environment</b>	Vacuum aids in the weld quality as it tends to pull out contamination from the melt pool	Vacuum is not applied. Laser uses atmosphere with additional shielding gas
<b>Shielding gas</b>	Not required	Needs the shielding gas (e.g., argon) to stop oxidization of the weld area and the melt pool
<b>Running cost elements</b>	Requires cooling water (normal quality), pump oils, electricity, and compressed air (for valve actuation)	Requires high purity water in cooling system held at a constant temperature, shield gas, and constant electricity
<b>Power efficiency</b>	80-90% achievable	7-10% achievable (however, absorption efficiency can be higher based on the material)
<b>Initial cost</b>	Higher than SLM	Lower than EBAM
<b>Cost (approximate)</b>	60 kV 4 kW (610 mm <sup>3</sup> ) electron beam including CNC controlled systems costs around \$311,000.00	4 kW laser excluding work manipulation system costs around \$353,500.00 [40]

Typically, electron beam is usually better solution than using laser beam for a process that requires a penetration of 5 mm or more. To obtain penetrations exceeding 10 mm, electron beam is the most cost-effective method [70]. A visual representation on the comparison of the SLM and EBAM is shown in Fig. 2.5, where the performance metrics are rated on a scale of ten [68]. The SLM method gives a better outcome in terms of surface finish, material range, accuracy, and component size. However, the EBAM method gives better productivity as it can melt a larger volume of material with the same energy input.

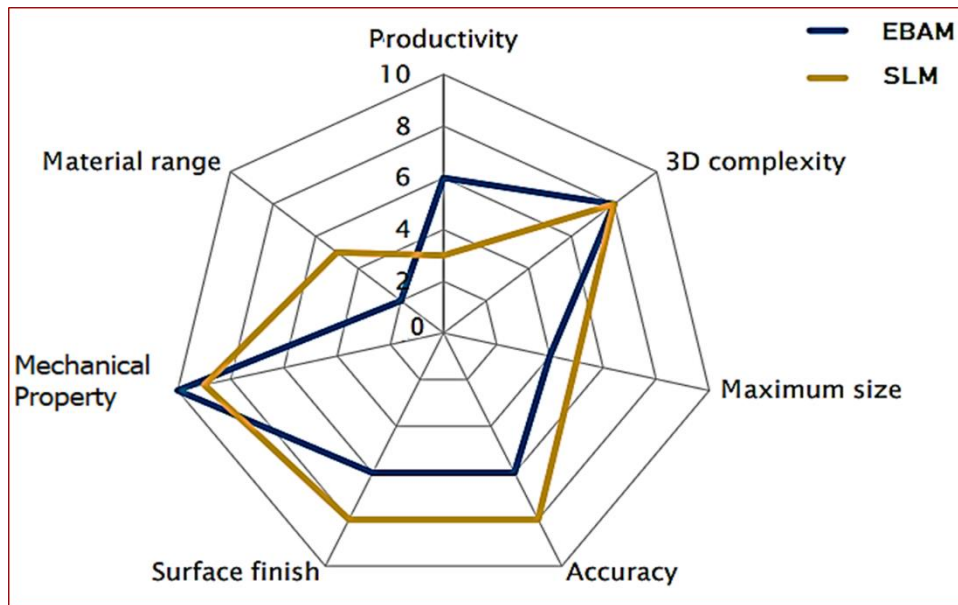


Figure 2.5: Comparison between SLM and EBAM in terms of rating on a scale of ten [68]

## 2.4 Energy Absorption Mechanism

The PBF process, in general, involves a non-equilibrium complex phenomenon of physical, chemical, and metallurgical processes, showing an intricate mechanism of heat and mass transfer [5]. Therefore, a good understanding of the energy absorption by the material and the physics of laser-material or electron beam-material interaction is necessary before conducting a numerical simulation of the thermal behavior and melt-pool evolution in the process. During

the PBF process, the entire amount of energy of the heat source is focused on the powder bed in a protective inert gas chamber. When a laser beam impinges on a particle, part of the energy is absorbed by the particle, part of the energy is reflected, and the rest is radiated after transmission. A simple schematic diagram is presented in Fig. 2.5 showing the laser penetration mechanism inside the powder layer.

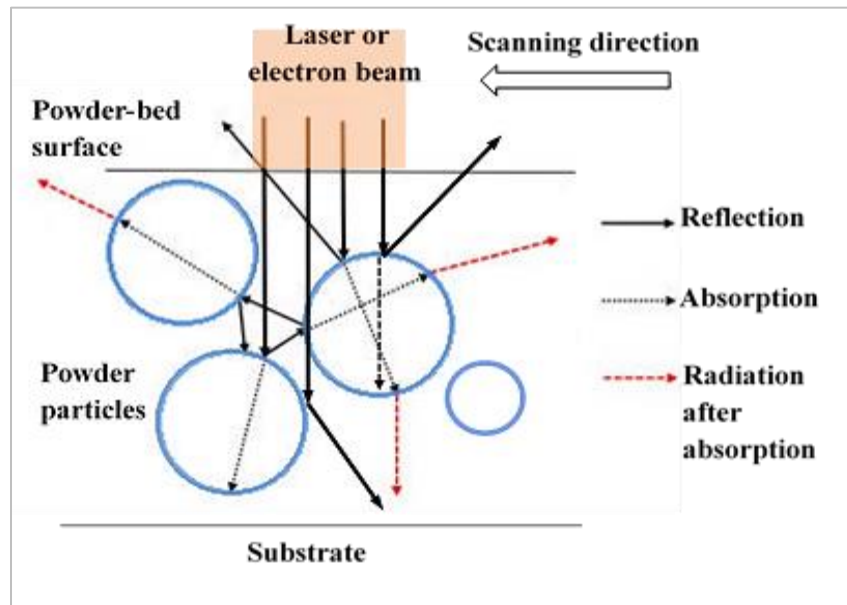


Figure 2.6: Laser or electron beam penetration in powder-bed [65]

As the beam undergoes multiple reflections within the powder layer, the coefficient of beam absorption by the powder bed becomes higher than the Fresnel absorption coefficient of the liquid surface [5]. The particle size in the powder-bed, packing density, and material properties strongly affect the heat absorption mechanism. The absorption coefficient values for a material are usually different for the laser and electron beams and depend on a number of factors including the beam control, beam focusing, vacuum or convective environment, inclination angle, and the energy absorption by the target material [63]. The values of the optical penetration depth (also known as the absorption depth) for laser and electron beam are also different as their

wavelengths and extinction coefficients are not the same. Therefore, studying the material absorption properties for laser and electron beam is crucial while investigating the PBF process outcomes.

## **2.5 Methodology for Process Investigation**

The common approaches for investigating of the process parameters involved in SLM and EBAM can be broadly classified into three methods:

- (i) Experimental method,
- (ii) Computational modeling and simulation, and
- (iii) A combination of experimental and computational methods.

The experimental approach, covering both the macroscopic and microscopic studies, addresses the challenges to be overcome more precisely to increase the acceptance by the industry. These range from business considerations (e.g. limited build speed and sizes) to technical or inherent differences in the process from industry standards, which manifest themselves in the as-built material properties [71]. When compared with subtractive processes (e.g., machining, forging, and forming) and in common with other net-shape processes (e.g., casting, molding, and powder compaction), there are process parameters which lead to porosity at various scales, these in turn affect strength and life properties of the components, but they can be controlled. Other notable aspects are surface roughness, minimization of the residual stresses and anisotropic elasticity properties, which are related to build directions.

Computational modeling, pursued by both researchers and commercial software providers, has a vital role to play in addressing these challenges in the AM processes, when compared with its role in other manufacturing processes. The digital nature of the process

combined with the high flexibility or freedom of design immediately places the onus on a virtual development of the design. This eventually leads to the necessity of the multi-scale simulations by which the operators and industry almost expect a seamless and rapid development of the link between the preliminary CAD design stage and a final optimized part, which is optimal from both the process as well as a functional perspective [71]. Modeling is typically undertaken using analytical or numerical solutions using self-developed codes which are typically based on finite element, finite volume, or finite difference method, or using commercial codes including ANSYS (Fluent/CFX), ABAQUS, COMSOL Multiphysics, and so on. The broad objectives are to accurately predict part properties and performance, and to understand the sensitivities of the process outcomes to important process parameters. Besides characterizing the parameters for optimum part quality, a reliable model can play a role in process qualification and part certification. Thus, the ultimate aim of a simulation-based approach is to actively control the AM production process, using feedback from process diagnostics [5].

There are a few key areas which are being looked at while using computational modeling, namely:

- (i) Thermal/thermo-fluid modeling of melting and solidification,
- (ii) Residual stress modeling, and
- (iii) Topological and shape optimization of components.

Thermal/thermo-fluid modeling is the fundamental and the most important modeling of the SLM and EBAM processes. Most of the works undertaken in this type of modeling either start with a Fourier equation of thermal base, or from a fluid-flow Navier-Stokes equation considering various length and time scales. During the application of the heat source to a powder bed, the understanding from these models gives helpful information about controlling the levels of

porosity, heat source specification, and formation of the microstructures, by this means giving an insight into the resulting material properties. The thermal history of a part is also the starting point for the residual stress analysis shape optimization. Thermal and CFD models for the analysis of melt-pool characteristics range from the analyses that neglect convective heat transfer, to models that solve 3-D heat transfer and fluid flow, along with tracking of the solid-liquid interface. The mechanical properties of a part produced by the EBAM depend on the preheating and high vacuum that need to be characterized accurately in the simulation. On the other hand, modeling of SLM requires incorporation of convection with the inert gas environment at room temperature.

The essential physics which needs to be captured by a comprehensive thermal model should include the followings:

- (a) Melting and solidification,
- (b) Free-surface re-construction, giving an indication of residual porosity including the compensation for shrinkage effects during solidification,
- (c) Multiple phases including liquid, gas, and solid,
- (d) Forced and natural convection of gas by either conjugating the gas convective, conduction or radiation heat transfer, or through heat transfer coefficient boundary conditions,
- (e) Laser or electron beam as an energy source (either indirectly as moving thermal boundary condition or directly by radiative modeling),
- (f) Introducing significant non-linearity into the solution with temperature dependent properties (e.g., thermal conductivity, density, specific heat capacity) of solid and powder and radiative properties (e.g., absorption, reflectivity and emissivity),

- (g) Temperature dependent surface tension of liquid metal in contact with powder – a property which determines to which extent the melt-pool flows are dominated by the Marangoni convection, and the levels of capillary infiltration of the melt-pool into the powder-bed, and
- (h) Incorporating phase-change of alloys which might identify regions of specific phases or even evaporative properties of alloys even on the sub-micron level.

The third approach is the combination of the experimental and numerical methods which is more versatile and robust compared to a single approach in terms of acceptance. The current study is based on the combination approach where significant focus has been given on the numerical modeling and the numerical results are validated by the analytical and experimental results.

## **2.6 Concepts on Multiphysics Modeling**

While developing a multiphysics model, it is important to find a convenient scheme to design the heat source, estimate the melt-pool geometry, and determine the temperature distribution in the build part as the melt-pool geometry strongly affects the build part microstructures. Consequently, the melting temperature, thermal conductivity, latent heat of fusion, and the specific heat of work materials are intuitively the dominant factors to be considered for the size estimation of the melt pool. Besides these thermal properties, the application of metallic or alloy powder adds one more important parameter to be considered – the porosity level. With the increase in the porosity level, temperature increases in the melt pool, causing an increase in the depth of the melt pool. Therefore, a robust thermal model must consider the correlations among temperature-dependent process parameters, the melt-pool

geometry, and heat source specifications to offer valuable information about the performance of the SLM or EBAM process.

As the laser beam continues to scan and melt the target material, the molten material coalesces and leaves a thin track of consolidated metal behind. Repetition of the single-track deposit with a specified overlap (i.e., hatching space) forms a complete layer and repeating the layer-by-layer deposition constructs the entire part. Therefore, the PBF simulation requires a coupled solution of heat transfer and fluid flow incorporating several physics as listed below [5, 65]:

- Heating and melting of powder particles,
- Formation of a melt pool,
- Surface tension and capillarity within the partially melted powder and the substrate [5],
- Fluid dynamics in the melt pool with thermal buoyancy forces,
- Convection and radiation from the metal surfaces,
- Evaporation of liquid and recoil pressure,
- Solid-liquid-solid phase change of metal and latent heat release or absorption,
- Temperature-dependent surface tension and the Marangoni effect,
- Formation of porosity, and
- Free-surface profile of the melt pool and its movement.

The variation of the PBF process parameters (namely, the laser power, scanning speed, spot size, hatching space, and powder layer thickness) yields various local melting and solidification conditions which significantly affect the microstructure and part quality. For instance, a high-power laser results in a large volume of melt pool. A faster scanning speed lowers the melt-pool volume and provides higher thermal shock to the powder particles. All the

material and process parameters mutually influence each other which leads to the necessity of understanding the degree of effect on the process outcome by each parameter. Therefore, studying the single-track deposit under various laser irradiation conditions provides a fundamental but all-inclusive understanding of the process envelop with the concept of optimizing the process parameters for numerous metals and alloy systems [65].

## **2.7 Established Functional Relationships**

While the thermal models incorporating melting and solidification of powder materials are somewhat more complicated, the following functional relationships are nevertheless valid universally [46, 70].

- The melt-pool size is larger with a higher maximum temperature in the powder layer than the solid layer. Given that the other parameters are the same, the size increases as the power or intensity of the heat source increases.
- The diameter of the melt pool is proportional to the diameter of the electron or laser beam under a given specification. For a given diameter, the melt-pool width generally increases with a decrease in the scanning speed and with an increase in beam power.
- At the same scanning speed and power, the melt-pool length generally decreases with the increase in the beam diameter. At a given diameter and scanning speed, the length increases as the power increases.
- The melt-pool depth generally decreases with an increase in the beam diameter and scanning speed but increases with an increase in beam power.
- A larger beam diameter will reduce the maximum temperature in the melt pool and temperature gradients can be much smaller, giving a lower cooling rate.

- The melting temperature and thermal conductivity of work materials are intuitively the two most dominant factors for the size of the melt pool [46, 51]. The latent heat of fusion and the specific heat may also affect the shape of the melt pool to some extent.
- Besides these thermal properties, the application of metallic or alloy powder adds one more important parameter to be considered during the process – the porosity level. With the increase in the porosity, temperatures are higher in the melt pool, causing an increase in the size (especially, the depth) of the melt pool.
- Both the heating and cooling rates decrease with the increase in the porosity level.

## Chapter 3

### Material and Methods

This chapter contains the description of the material of interest, numerical modeling, and experimental methods used in the overall analysis. The material properties and the heat source are added in the numerical model as the user-defined functions (UDFs). Figure 3.1 illustrates the overall scope of the study combining the analytical, numerical, and experimental methods. The explanations of the numerical and experimental methods are mainly focused in this chapter whereas the analytical method is illustrated in chapter 4 (Mathematical Model) and chapter 6 (Model Validation).

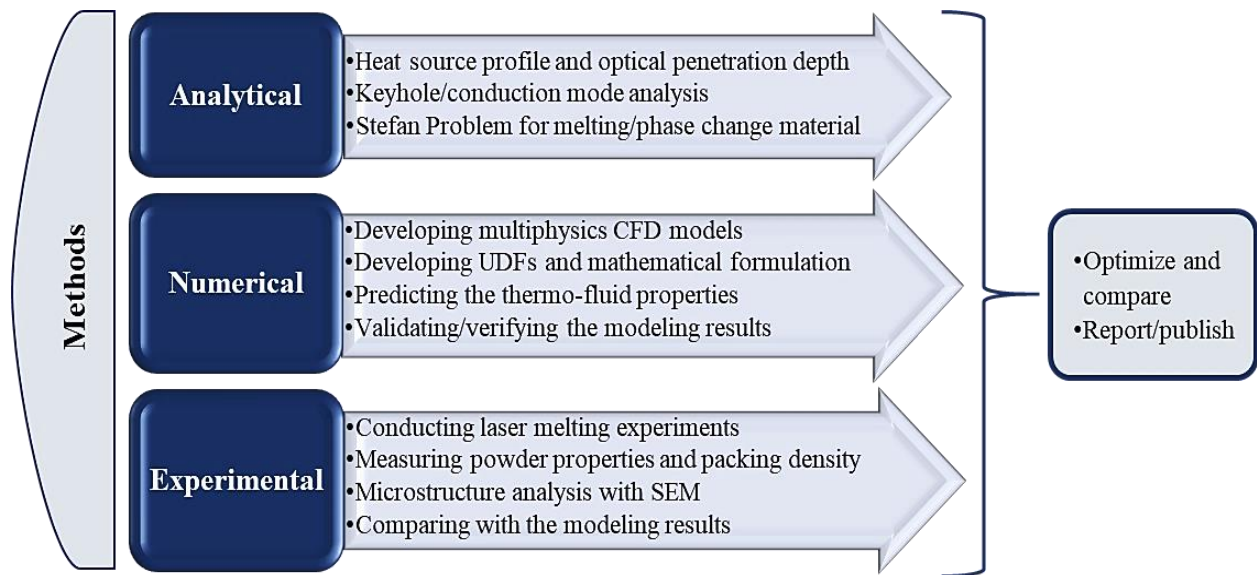


Figure 3.1: Scope of the study showing the analytical, numerical, and experimental methods

### 3.1 Material Modeling

Selection of an appropriate material for the analyses of SLM and EBAM processes is an important step because, the material behavior significantly affects the process outcome. The material selected for this analysis is Ti-6Al-4V, which is a high entropy alloy having outstanding

mechanical properties such as low density, high strengths, good chemical resistance, and excellent biocompatibility. The chemical composition of Ti-6Al-4V is given in Table 3.1.

**Table 3.1: Chemical composition of Ti-6Al-4V (grade 5) as mass percentage [60]**

N	C	H	Fe	O	Al	V	Ti
0.05	0.08	0.015	0.40	0.20	5.5-6.75	3.5-4.5	Bal.

It is well known that the thermal properties of metallic powder materials are significantly different from those of the corresponding solid bulk material [72–76], especially, in thermal conductivity, melting point, specific heat capacity, and density. Li *et al.* [75] experimentally determined the density, specific volume, and viscosity of Ti-6Al-4V by the electrostatic levitation method. The porosity of the powder material has a great impact on the thermal responses that govern the process performance and part quality. The thermal conductivity of the powder decreases as the porosity increases [51]. Again, the effect of thermo-fluid properties of Ti-6Al-4V on the PBF process is substantial because, these properties determine the nature of preheating, melting, and solidification which eventually play a significant role in the characterization of the quality and mechanical properties of the build part. Therefore, the simulation of a thermo-fluid model accounts for the specific powder properties to achieve better exposure, desired results, and scope for further improvements. With a view to understanding the thermal responses of the process parameters, the temperature-dependent thermal conductivity, specific heat, and density as reported by Jamshidinia *et al.* [57, 58], Mills [76], and Dai *et al.* [77] are presented in Figs. 3.2, 3.3, and 3.4, respectively. The temperature-dependent properties of Ti-6Al-4V, shown in Table 3.2, are used to create the UDFs for the CFD models. The UDFs are written and saved as C-programming files containing subroutines and macros.

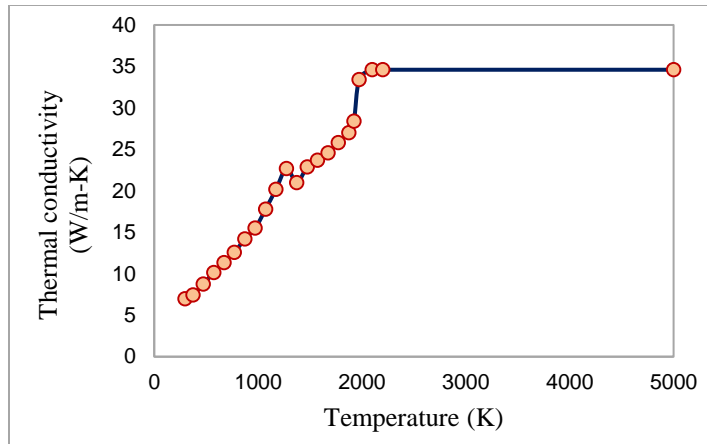


Figure 3.2: Temperature dependent thermal conductivity of Ti-6Al-4V powder

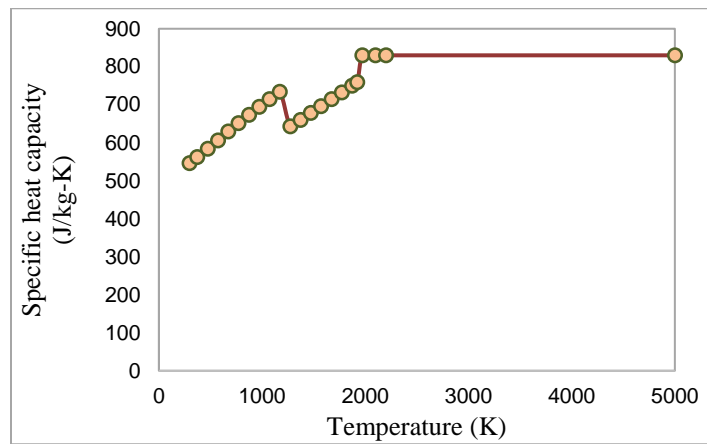


Figure 3.3: Temperature dependent specific heat of Ti-6Al-4V powder

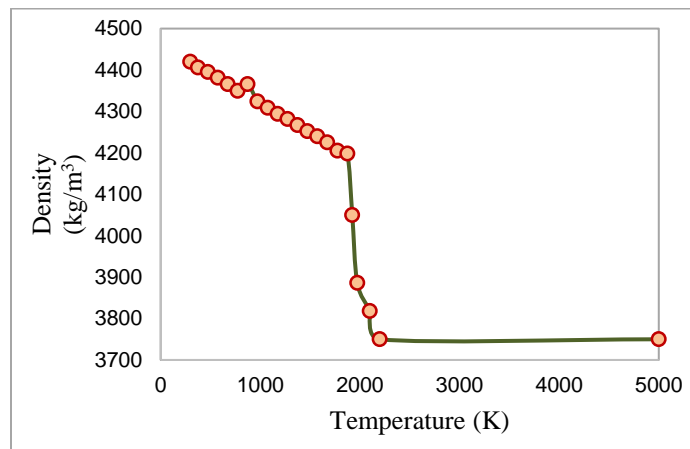


Figure 3.4: Temperature dependent density of Ti-6Al-4V powder

**Table 3.2: Thermal properties of Ti-6Al-4V used as the user-defined functions [63, 78]**

Properties	Material State	Temperature Range (°C)	Polynomial Functions
Specific Heat Capacity, $C_p$ (J/kg.K)	Powder	23<T<1650	$C_p = (0.52036 - (8.34 \times 10^{-6}) T (\text{°C}) - (4.46 \times 10^{-7}) T^2 (\text{°C}) + (5.44 \times 10^{-10}) T^3 (\text{°C})) \times 1000$
	Solid	23<T<1650	$C_p = (0.54058 + (1.02 \times 10^{-4}) T (\text{°C}) + (1.35 \times 10^{-7}) T^2 (\text{°C}) - (6.50 \times 10^{-11}) T^3 (\text{°C})) \times 1000$
	Liquid	1650<T<3200	830
Thermal Conductivity, $k$ (W/m.K)	Powder	23<T<1650	$k = 0.9315 - 0.00339T (\text{°C}) + (6.55 \times 10^{-6}) T^2 (\text{°C}) - (1.41 \times 10^{-9}) T^3 (\text{°C})$
	Solid parallel	23<T<1650	$k = 6.95757 + 0.00224T (\text{°C}) + (1.69 \times 10^{-5}) T^2 (\text{°C}) - (7.58 \times 10^{-9}) T^3 (\text{°C})$
	Solid orthogonal	23<T<1650	$k = 8.23346 - 6.30 \times 10^{-2} T (\text{°C}) + (1.43 \times 10^{-5}) T^2 (\text{°C}) - (2.97 \times 10^{-9}) T^3 (\text{°C})$
	Liquid	1650<T<3200	$k = -1.6614 + 0.0183T (\text{°C})$
Emissivity, $\varepsilon$	Melt-pool front	23<T<1650	$\varepsilon = 0.43356 + (2.94 \times 10^{-4}) T (\text{°C}) + (5.48 \times 10^{-7}) T^2 (\text{°C}) - (5.53 \times 10^{-10}) T^3 (\text{°C})$
	Practical contact area	23<T<1650	0.83
	Powder	23<T<1650	0.6
	Melt-pool front	1650<T<2700	0.4
Density, $\rho$ (kg/m <sup>3</sup> )	Solid	23<T<1650	$\rho_{solid} = (4420 - 0.154 (T - 25\text{°C}))$
	Powder	23<T<1650	$\rho_{powder} = (1 - \text{porosity}) \times \rho_{solid}$
	Liquid	1650<T<3200	$\rho_{liq} = (3920 - 0.68 (T - 1650\text{°C}))$

The material properties presented in Table 3.2 play an important role in the numerical implementation, as they are functions of temperature and undergo a large variation from room temperature to above the melting temperature during the PBF processes. The temperature-dependent properties require a coupling of the momentum equations with the energy equation and give rise to a strong nonlinearity in the conservation equations. The equations are illustrated in chapter 4 where the temperature-dependent behavior of viscosity is also outlined.

### 3.2 Numerical Modeling

The numerical analysis for the PBF process is performed by developing 3-D transient CFD models with Ti-6Al-4V as the powder-bed material. The modeling results for thermo-fluid properties are obtained by using the finite volume method in ANSYS Fluent R19.2. Simulations for the SLM and EBAM processes are conducted separately with their corresponding UDFs, and the obtained results are compared at the same irradiation conditions. The two PBF cases are:

- a) The SLM Model (considering an inert gas environment and laser scanning)
- b) The EBAM Model (considering vacuum and an electron beam scanning)

Both models have the same geometry when compared to each other, but the UDFs and boundary and initial conditions are different. The macros for the temperature-dependent properties are the same in the UDFs for SLM and EBAM since the material is not changing. However, the subroutine for the heat source in the UDFs must be different as the SLM model employs a laser while the EBAM model uses an electron beam. The schematics of the SLM and EBAM processes showing the differences in physics are shown in Figs. 3.5 and 3.6, respectively.

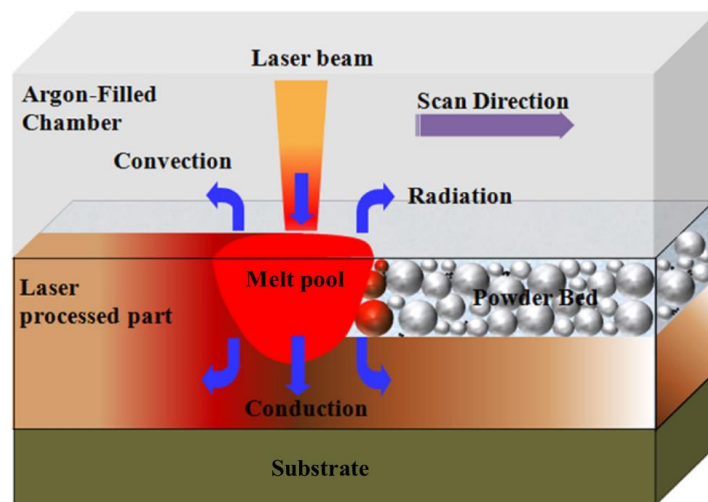


Figure 3.5: Schematic of the SLM Process [38]

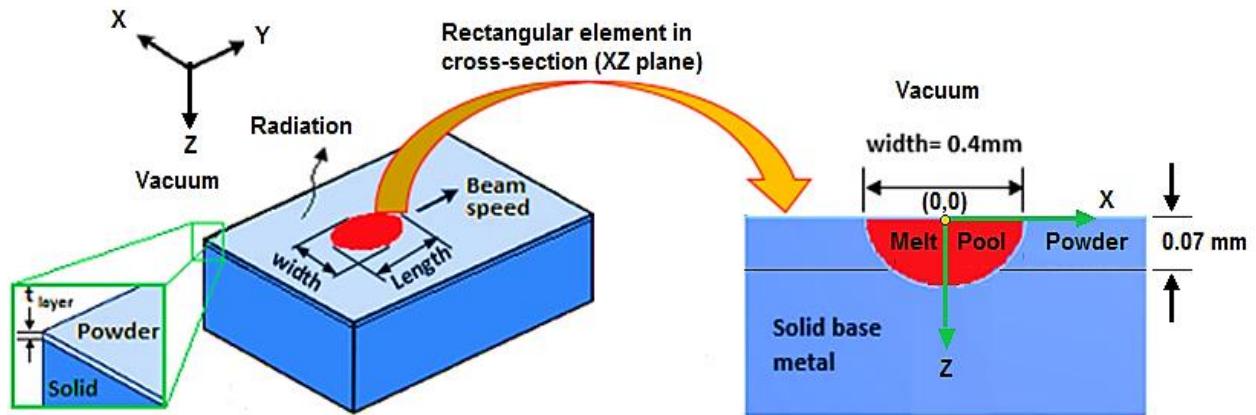


Figure 3.6: Schematic of the EBAM Process [51, 62]

### 3.2.1 Configuration of the Physical Domain

Configuration of the 3-D model is shown in Fig. 3.6 where the physical domain consists of a solid Ti-6Al-4V substrate and a layer of Ti-6Al-4V powder on top of the substrate. The substrate is considered as a rectangular solid block of  $14 \text{ mm} \times 4 \text{ mm} \times 4 \text{ mm}$  volume while the powder layer is modeled on top of the block as  $14 \text{ mm} \times 4 \text{ mm} \times 0.07 \text{ mm}$  volume. Therefore, the cross-section in  $xz$ -plane had the dimensions of  $4 \text{ mm}$  width and  $4.07 \text{ mm}$  height including the powder layer thickness of  $0.07 \text{ mm}$ . It is assumed that the maximum heat of the laser or electron beam (i.e., the center of the heat source) is located at the center of a target surface, and the intensity varies radially along the heat source. The laser or the electron beam scans the top surface of the powder-bed in  $y$ -direction. For all simulations, only one unidirectional scan is considered for both SLM and EBAM. The geometry of the melt pool largely depends on the specifications of the heat source. For a given porosity of the powder and beam scanning speed, the melt-pool size increases as the power of the beam increases. However, both the electron beam and laser (considered for the comparative study) have the same diameter of  $0.4 \text{ mm}$  and the

same scanning speed of 330 mm/s. They scan the top surface of the domain starting from (0, 2 mm, 0) to the end-point at (0, 12 mm, 0) as shown in Fig. 3.7.

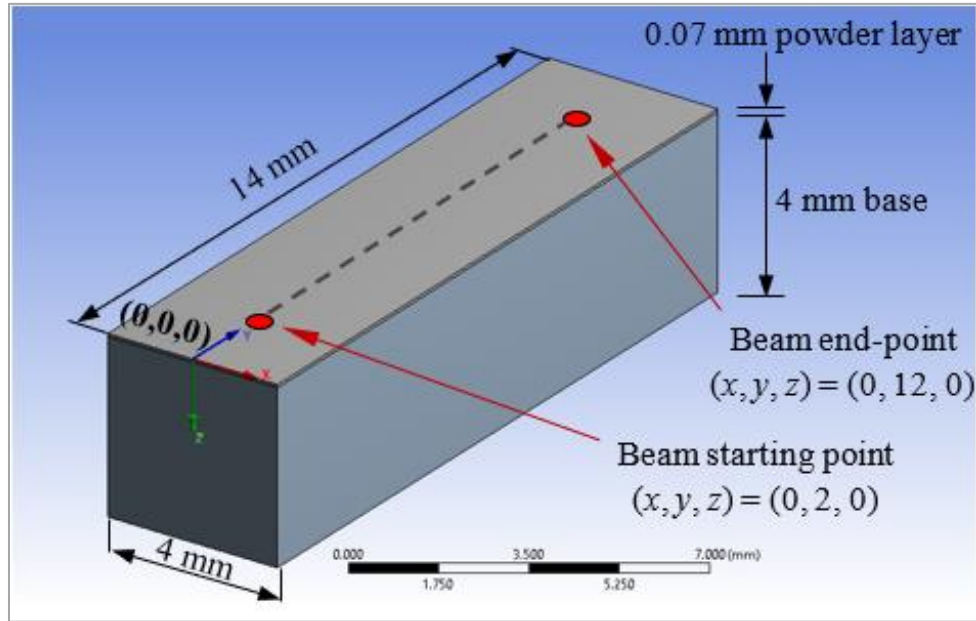


Figure 3.7: Physical domain of the 3-D model with laser or electron beam travel specifications

The configuration shown above is used for the comparative study on the SLM and EBAM processes. However, a separate geometry with large dimensions is also considered for the EBAM simulation, which is discussed in chapter 5 (Results and Discussion). Furthermore, a modified version of the SLM model is created to compare the numerical results with the SLM experimental results, which is illustrated in chapter 6 (Model Validation).

### 3.2.2 Computational Domain

The computational domain for the comparative study contains the same geometry as the physical domain shown in Fig. 3.7. As the powder at the top is melted by the heat source, the liquid melt pool is assumed to be a pseudo-incompressible Newtonian fluid with laminar flow. The powder layer shrinkage is ignored to avoid the effect of density change during the melting of

alloy powders. The top surface of the melt pool is assumed to be flat and all the nodes remained in their positions. Heat transfer by convection on the top surface is neglected in EBAM due to the vacuum environment. The 3-D computational domain considered for the analysis is discretized using a structured mesh with hexahedral cells. Figure 3.8 shows the 3-D mesh of the computational domain where 190,040 hexahedral cells are connected with 200,889 nodes. The structured mesh is formed by biasing the grid in the powder layer region and around the scanning path of the moving heat source to have a very fine mesh in the target zone.

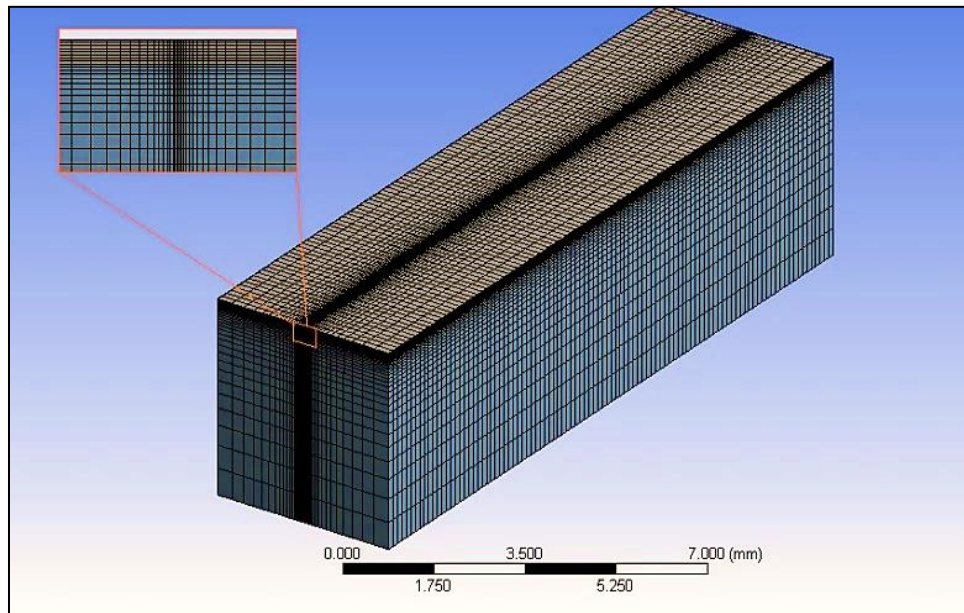


Figure 3.8: 3-D computational domain with a structured mesh

The thermal boundary conditions applied in the simulations of SLM and EBAM are similar, but unlike EBAM, SLM included convection heat transfer on the top. The top surface is exposed to radiation with an ambient temperature of 298 K for both SLM and EBAM. The side walls and bottom of the domain in EBAM are in adiabatic condition with 1003 K temperature. As SLM does not require preheating, the side walls and bottom of the domain are kept in adiabatic condition with 298 K. The 2-D cross-sectional views of the domains for the SLM and

EBAM models are shown in Fig. 3.9, where the boundary and initial conditions for the two models are depicted in terms of temperature and velocity components.

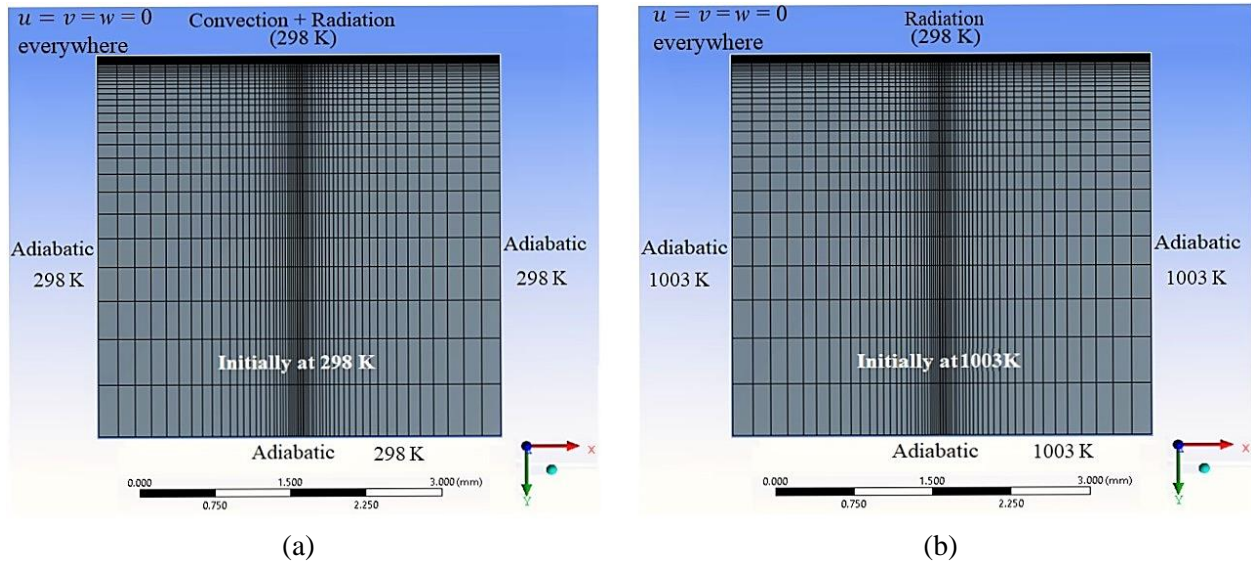


Figure 3.9: 2-D views of the computational domains with initial and boundary conditions for the (a) SLM and (b) EBAM models

### 3.2.3 Mesh Convergence Study

A mesh independence or convergence study is conducted for the structured mesh of the 3-D domain considering the variation of melt-pool temperature with the increase of number of nodes. The temperature at location  $(x, y, z) = (0 \text{ mm}, 5 \text{ mm}, 0.03 \text{ mm})$  is monitored for several different mesh densities at 0.009 s when the beam diameter is 0.4 mm, scanning speed is 330 mm/s, and the effective power is 216 W. The value of temperature inside the melt pool converges to 2571 K with the increase of number of nodes in the domain. Figure 3.10 depicts the results for the mesh convergence study where the temperature at the fixed point remains unchanged after 200,889 nodes corresponding to 190,040 hexahedral cells. Results for both SLM and EBAM models are obtained for the converged mesh.

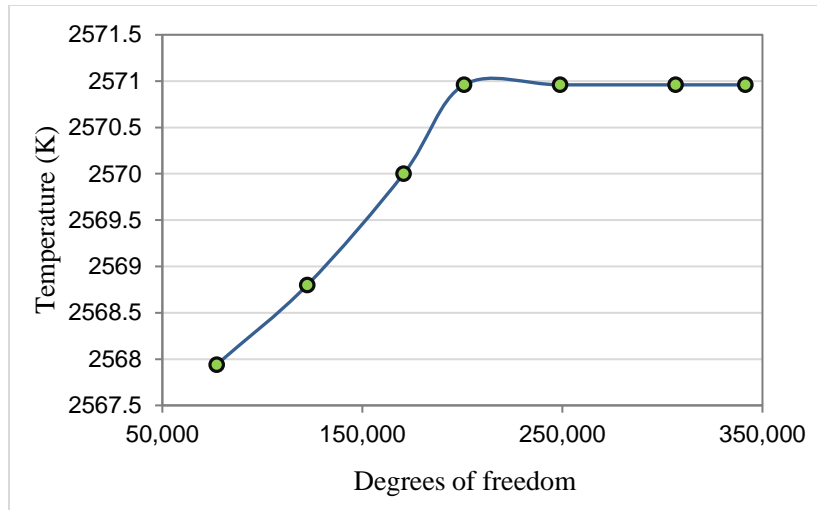


Figure 3.10: Convergence of melt-pool temperature with the increase of degrees of freedom at  $t = 0.009$  s

### 3.2.4 Simulation Procedure

The simulations are performed in ANSYS Fluent R19.2 covering a transient thermo-fluid analysis of the 3-D domain. The thermal properties and the specifications of the moving heat source are assigned as UDFs to simulate the transient melting and solidification for both SLM and EBAM models. The mass, momentum, and energy conservation equations are discretized and solved using the control volume method with appropriate boundary conditions. ANSYS Design Modeler is used to create the geometry, Mesh tool is used to generate the structured mesh, and the mathematical model is followed to define the boundary types of the 3-D computational domain. During the simulations, the UDF is loaded before each iteration to insert the heat source term and the material properties. The finite volume approach ensures that the numerical scheme is locally and globally conservative, while the enthalpy formulation can treat phase change in a straightforward and unified manner. Once new temperature field is obtained, the thermo-physical properties are updated. The pressure-based coupled algorithm solves a coupled system of equations comprising the momentum equations and the pressure-based

continuity equation. Since the governing equations are nonlinear and coupled to one another, the solution process involves iterations wherein the entire set of governing equations is solved repeatedly until the solution converges. The rate of solution convergence is significantly higher in a coupled algorithm than that in the segregated algorithm. A representative set of solver specification used in Fluent for a typical PBF simulation is shown in Table 3.3.

**Table 3.3: A sample set of solver settings in Fluent**

<b>Description</b>	<b>Settings</b>
Problem setup – solver	Pressure based
Energy	On
Viscous	Laminar
Solidification & melting	On
Pressure-velocity coupling	Coupled
Courant number	1
Gradient discretization	Green Gauss cell based
Pressure discretization	Second order upwind
Density discretization	Second order upwind
Momentum discretization	Second order upwind
Energy	Second order upwind
Transient formulation	First order upwind
Residual criteria	$10^{-4}$
Time step size	0.005 s
Max iterations/time step	$42 \text{ s}^{-1}$

### 3.3 Experimental Analysis

A custom designed laser system is used to conduct laser melting experiments on a solid Ti-6Al-4V specimen to study the effects of various laser irradiation conditions on the melt-pool geometry. The laser system setup is equipped with an ytterbium fiber laser (IPG model: YLR-200-AC-Y11), an IPG D25 Collimator, a Cambridge Technology ProSeries II scan head, and a Jenoptik F-theta lens as shown in Fig. 3.11.

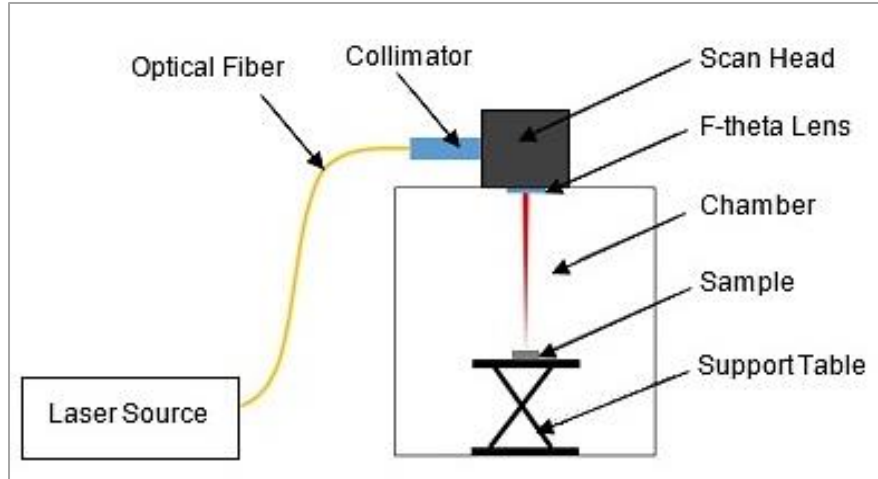


Figure 3.11: Schematic diagram of laser system setup [79]

Spherical Ti-6Al-4V powders with an average size of  $25\ \mu\text{m}$  are utilized, and a powder bed with a thickness of  $70\ \mu\text{m}$  is deposited on top of a  $25.4\ \text{mm} \times 25.4\ \text{mm}$  Ti-6Al-4V stage, i.e., the solid substrate having a thickness of 2 mm. The porosity of the powder is measured manually using the powder density and the bulk density of Ti-6Al-4V. Table 3.4 shows the density data for the measurement of the powder porosity which is found to be 58.76%.

**Table 3.4: Packing density of Ti-6Al-4V powder**

Powder volume (mL)	Mass (g) (powder + measuring cylinder)	$\Delta$ mass (g) (reference to 6 mL case)	Density ( $\text{g}/\text{cm}^3$ )	Average density ( $\text{g}/\text{cm}^3$ )	Bulk density ( $\text{g}/\text{cm}^3$ )	Porosity (%)
6	16.8437	0	-			
7	19.4073	2.5636	2.5636	$2.603 \pm$	4.43	58.76
8	22.1883	5.3446	2.6723	0.060		
9	24.5672	7.7235	2.5745			

The specimen is placed in a custom designed laser system for laser processing. Several laser scans are performed to investigate the effects of changing scanning speed, power, and spot size on the melt-pool evolution. After laser scanning, the Ti-6Al-4V specimens is cut vertically to

the laser scanning direction using a low speed saw. Then the cross section is ground with SiC papers (320, 600, 800, 1000, and 1200 grit successively), polished with the MetaDiTM Supreme polycrystalline diamond suspension (1  $\mu\text{m}$ ), rinsed ultrasonically in acetone, ethanol, and deionized water for 20 min each, and finally etched with the Kroll's Reagent to reveal the cross-section of the laser scanning tracks. The microstructures of the cross-sectional areas are examined by a Quanta™ 3D Dual Beam™ FEG FIB-SEM scanning electron microscope (SEM) with an accelerating voltage of 20 kV.

The SEM images of the microstructures are shown in chapter 5 (Results and discussion). Experiments are conducted with both the solid and the powder-bed Ti-6Al-4V specimens. However, results for the melt-pool evolution in the solid specimen are compared with the numerical results for melt-pool width and depth in order to validate the SLM model, which are described in chapter 6 (Model Validation).

## Chapter 4

### Mathematical Model

The mathematical model for the 3-D PBF configurations is developed based on the concepts of CFD. In this chapter, the conservation and heat source equations corresponding to the three case studies have been presented with necessary assumptions.

#### 4.1 General Assumptions

The assumptions of the mathematical formulation for the PBF Models are given below:

- (1) The melt flow within the melt-pool is compressible, Newtonian, and laminar,
- (2) The entire domain is initially at a temperature of 1003K for EBAM and at the room temperature, i.e., 298 K for SLM,
- (3) Flat top surface during melting and solidification,
- (4) Negligible powder shrinkage during melting,
- (5) No Convection at the top boundary for EBAM,
- (6) The top surface is exposed to convection and radiation with 298 K for SLM whereas EBAM has only radiation,
- (7) The side walls and bottom wall are in adiabatic conditions,
- (8) No evaporation,
- (9) The heat source follows Gaussian distribution, and
- (10) The powder layer shrinkage is neglected to avoid the effect of change in density.

#### 4.2 Modeling of the Heat Source

Both the laser and electron beams are modeled as conical volumetric heat source with a Gaussian distribution, where the maximum power intensity is at the center and the intensity

decreases with the increase in the depth and width. The amount of absorbed energy in the material decreases exponentially through the thickness, as predicted by the Beer–Lambert law [5]. The 3-D conical volumetric Gaussian heat source model is expressed by Eqs. (1)–(3) [58, 62, 63]. These equations are used to create the subroutine for the heat source in the UDF.

$$\dot{Q}'''(x, y, z, t) = \eta \times \frac{H_s \times I_z}{S} \quad (1)$$

with

$$I_z = \frac{1}{0.75} \left( -2.25 \left( \frac{z}{S} \right)^2 + 1.5 \left( \frac{z}{S} \right) + 0.75 \right) \quad (2)$$

$$H_s = \frac{2P_H}{\pi\Phi^2} \exp \left\{ -\frac{2[(x - x_s)^2 + (y - y_s)^2]}{\Phi^2} \right\} \quad (3)$$

A schematic of the conical volumetric heat source and a representative contour for the distribution of heat flux on the top surface of the PBF material are shown in Fig. 4.1.

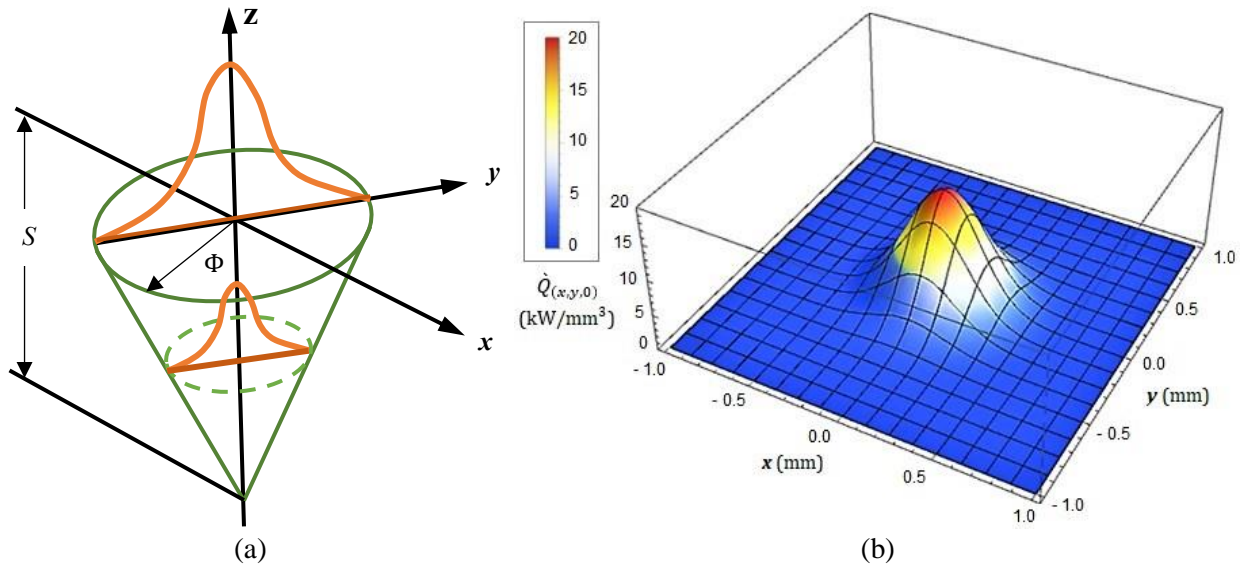


Figure 4.1: (a) Conical volumetric heat source, and (b) heat flux for a beam power of 240 W

In Eq. (3),  $x_s$  and  $y_s$  are the instantaneous positions of heat source in the  $x$ - and  $y$ -directions, respectively, which can be calculated by multiplying the velocity of the heat source with elapsed computational time. The power of the electron beam is given by  $P_H = VI_b$ , where  $V$  is the acceleration voltage and  $I_b$  is the beam current. The values of efficiency  $\eta$  for the laser and the electron beam are usually different which are shown in the results section. The penetration depth  $S$  of the electron beam in Ti-6Al-4V powder is given by

$$S = S_E = 2.1 \times 10^{-5} \frac{V^2}{\rho} \quad (4)$$

where  $S_E$  is the penetration depth of electron beam in  $\mu\text{m}$ ,  $V$  is the electron beam potential in V, and  $\rho$  is density of powder-bed in  $\text{kg/m}^3$  [58]. Using a voltage of 60 kV and a powder density of  $2150 \text{ kg/m}^3$ , the value of  $S_E$  is found to be  $35.16 \mu\text{m}$ . In case of laser, the parameter  $S$  is set to be the optical penetration depth  $S_L$  which is defined as the depth along the propagation direction at which the intensity of the laser drops to  $1/e$  of its initial value at the interface [86], and can be determined by the following relation [63]:

$$S = S_L = \frac{1}{a} = \frac{1}{2.303 \times \frac{A}{l_t}} \quad (5)$$

where  $a$  is the absorption coefficient [80–82] in  $1/\mu\text{m}$ ,  $l_t$  is the powder layer thickness in  $\mu\text{m}$ , and  $A$  is the optical absorbance [83] of the laser beam while penetrating the Ti-6Al-4V powder-bed. The absorbance of electron beam in Ti-6Al-4V powder-bed is higher than that of the laser beam because the photons are mostly deflected rather than absorbed into the material [84]. Taking  $l_t = 70 \mu\text{m}$  and  $S = 35.16 \mu\text{m}$  in Eq. (12), the value of  $A$  for electron beam is found 0.8645. Considering a solid state yttrium-aluminum garnet doped with neodymium ions

(Nd:YAG) laser with a wavelength of 1060 nm, the absorbance of laser beam in Ti-6Al-4V alloy is considered as 0.49 [85] which gives  $S_L = 62 \mu\text{m}$  for the SLM simulations. Figure 4.2 shows the values of beam penetration function for the static laser and electron beams along the vertical coordinate of the domain where the  $z$  values are taken such that  $0 \leq z \leq S$ . The higher value of  $S$  for laser beam results in deeper distribution of its intensity as compared to the intensity of the electron beam within the specified range of vertical coordinate  $z$ .

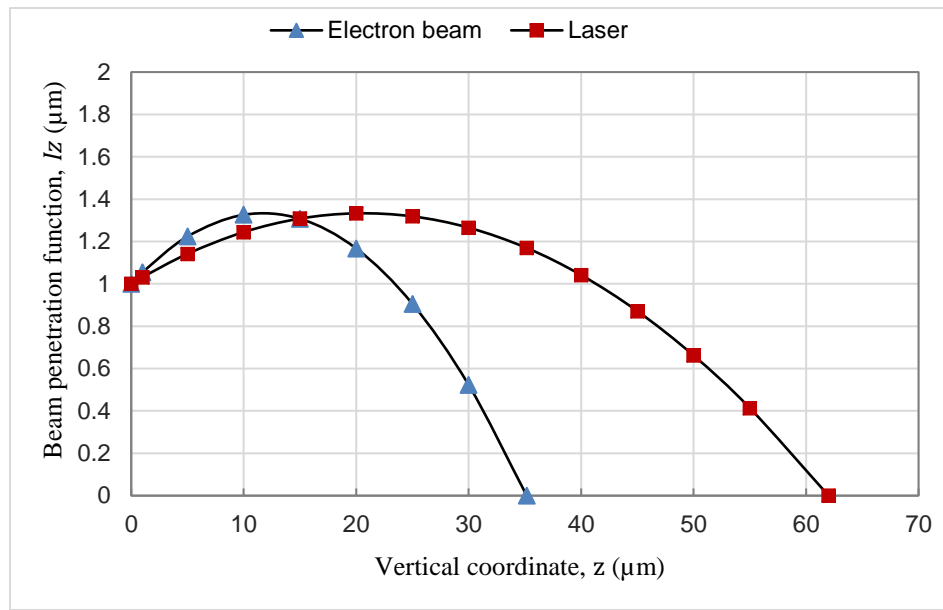


Figure 4.2: Comparison of the beam penetration functions for laser and electron beam

### 4.3 Energy Density and Interaction Time

The effect of changing process parameters on the heat transfer and melt-pool dynamics in the SLM process can be effectively studied by altering the laser irradiation conditions which necessitate the calculation of volumetric energy density and laser interaction time. The energy density  $E_D$  for single scan and heat source interaction time  $t_i$  are defined by the following relations [86, 87]:

$$E_D = \frac{P_H}{v_s \times l_t \times \Phi} \quad (6)$$

$$t_i = \frac{\Phi}{v_s} \quad (7)$$

Energy distribution of the collimated fiber laser beam on the focused spot follows the Gaussian distribution. The intensity is high at the center which causes deep penetration and temperature gradients in the melt pool. The intensity of the beam decays from the center to the periphery inducing a lack of fusion [86]. The fusion of material takes place either in keyhole mode or in conduction mode as shown in Fig. 4.3.

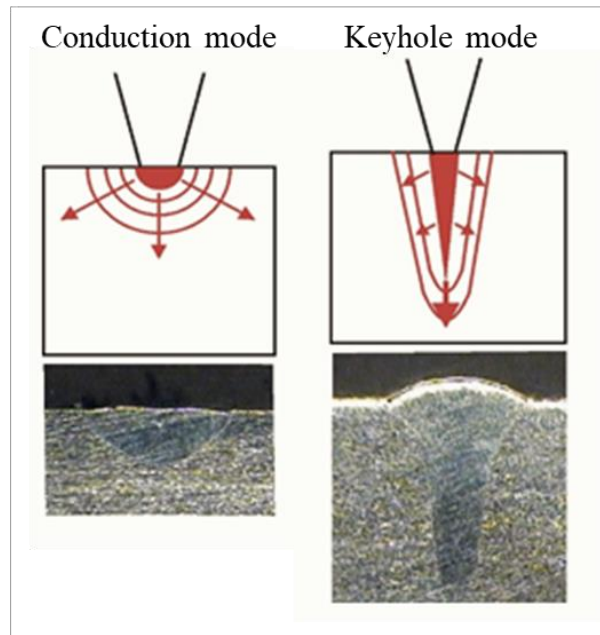


Figure 4.3: Conduction and keyhole modes for melt-pool evolution [88]

The threshold for keyhole mode can be rewritten based on laser processing parameters [89] as follows:

$$\frac{P_H}{\sqrt{v_s \Phi^3}} \geq \frac{kT_b \sqrt{\pi^3}}{A\sqrt{D}} \quad (8)$$

where  $k$  is the thermal conductivity,  $D$  is the thermal diffusivity,  $A$  is the laser absorptivity in powder layer (equivalent to the optical absorptance), and  $T_b$  is the boiling temperature of the material.

Keyholing in the melt pool usually occurs due to a high power-density at the center causing re-melting of the previous layer in exchange for excessive irradiation and resulting in a deeper penetration than the conduction mode. Keyhole mode is more common because it produces narrow heat affected zones (HAZs) [89]. However, keyhole oscillations and closures result in instabilities of the melt pool, leading to creation of pores in the welded zones. On the other hand, there is more stability in the conduction mode since vaporization is minimal. Conduction-mode fusion are produced by using low-power beams which create shallower melt pool than the keyhole-mode fusion.

The maximum power density versus electrical power of the heat source at various beam efficiency is shown in Fig. 4.4.

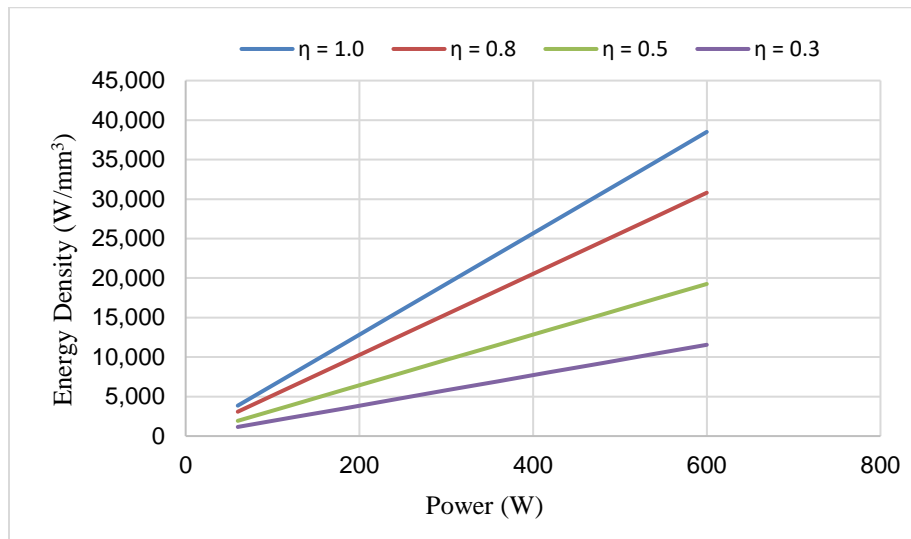


Figure 4.4: Variation of heat density with electrical power at different heat source efficiencies

The plot of heat density as a function of electrical power demonstrates their linearly proportional relationship following Eqs. (1) and (3). The assumptions for the two-dimensional plot are as follows:

- Beam speed, layer thickness, and spot size are constants.
- Energy densities of the heat source are considered at their maximum conditions, i.e., at the centerline coordinates ( $x = 0, y = 0$ ).

#### 4.4 CFD Formulation

For a 3-D, transient, compressible, laminar, and Newtonian melt flow in the liquid domain, the equations governing the motion and heat transfer in the domain are given by Eqs. (9) through (17).

The conservation of mass, i.e., the continuity equation [58–65] is given by

$$\frac{\partial \rho}{\partial t} + \frac{\partial(\rho u_i)}{\partial x_i} = 0 \quad (9)$$

where,  $\rho$  is the density and  $x_i$  and  $u_i$  are the distance and velocity along the Cartesian coordinates, respectively.

The conservation of momentum equation, in general form, can be given by the following equation [5, 58, 63]:

$$\frac{\partial(\rho u_j)}{\partial t} + \frac{\partial(\rho u_i u_j)}{\partial x_i} = -\frac{\partial P}{\partial x_j} + \frac{\partial}{\partial x_i} \left( \mu \frac{\partial u_j}{\partial x_i} \right) + \rho g_j - C_M \left( \frac{(1 - f_L)^2}{f_L^3 + B} \right) u_j + v_s \frac{\partial(\rho u_j)}{\partial x_i} \quad (10)$$

Considering the Boussinesq approximation, the third term on the right side of Eq. (10) can be modified by defining density as  $\rho = \rho_{ref} - \rho_{ref}\beta_{ref}(T - T_{ref})$  [90, 91] to display the buoyant force. The modified momentum equation then becomes,

$$\begin{aligned} \frac{\partial(\rho u_j)}{\partial t} + \frac{\partial(\rho u_i u_j)}{\partial x_i} = & -\frac{\partial P}{\partial x_j} + \frac{\partial}{\partial x_i} \left( \mu \frac{\partial u_j}{\partial x_i} \right) + \rho_{ref} g_z - \rho_{ref} g_z \beta_{ref} (T - T_{ref}) \\ & - C_M \left( \frac{(1 - f_L)^2}{f_L^3 + B} \right) u_j + v_s \frac{\partial(\rho u_j)}{\partial x_i} \end{aligned} \quad (11)$$

In Eq. (11), the scanning speed  $v_s$  is in the  $y$ -direction and gravitational acceleration  $g_z$  is in the  $z$ -direction. Therefore, only the  $y$ -momentum equation contains the last term associated with  $v_s$  which is the relative motion between the heat source and the work piece. Here,  $P$  is the pressure,  $T$  is the temperature,  $T_{ref}$  is the reference temperature,  $\rho_{ref}$  is the density of liquid at the reference temperature,  $\beta_{ref}$  is the coefficient of volume expansion at the reference temperature (also known as the coefficient of thermal expansion),  $f_L$  is the liquid fraction,  $C_M$  is a constant that accounts for the mushy zone morphology, and  $B$  is a very small computational constant introduced to avoid division by zero [63]. The third, fourth, and fifth terms in the right side of Eq. (10) represent the gravity, buoyancy force, and the frictional drag in the mushy zone during the solid-liquid-solid transition (the Darcy term), respectively.

The transient conservation of energy equation (i.e., the heat equation) states that the total amount of energy in a closed domain is constant. In this study, the energy of the laser or electron beam is inserted into the domain from the top surface and is used to increase the domain temperature, while heat loss by conduction, convection and radiation occurs through the

boundaries. Thus, the thermal energy transportation in the domain can be expressed by the following energy equation [5, 39, 92]:

$$\frac{\partial}{\partial t}(\rho H) + \frac{\partial}{\partial x_i}(u_i \rho H) = \frac{\partial}{\partial x_i} \left( k \frac{\partial T}{\partial x_i} \right) + \dot{Q}'''(x, y, z, t) + S_H \quad (12)$$

where  $k$  is the thermal conductivity,  $H$  is the total enthalpy,  $\dot{Q}'''(x, y, z, t)$  is the heat source as a function of the position and time, and  $S_H$  represents the remaining source terms. The phase change problem can be solved by a simple and flexible enthalpy method [63, 92, 93]. When the temperature is away from the liquidus temperature  $T_L$  or falls between the solidus temperature  $T_S$  and liquidus temperature  $T_L$ , the total enthalpy  $H(T)$  can be defined as the sum of the sensible heat and the latent heat as follows [63, 92, 93]:

$$H(T) = \int_0^T c_p dT + L_f f_L \quad (13)$$

where the liquid fraction  $f_L$  can be expressed as follows [63, 93]:

$$f_L = \begin{cases} 0 & T < T_S \\ \frac{T - T_S}{T_L - T_S} & T_S \leq T \leq T_L \\ 1 & T > T_L \end{cases} \quad (14)$$

Equation (13) can be rearranged with the information of Eq. (14) to yield the relation between the enthalpy and temperature as given by Eq. (15) [62].

$$T = \begin{cases} H/c_p & H < c_p T_S \\ T_S \leq T \leq T_L & c_p T_S \leq H \leq c_p T_L + L_f \\ (H - L_f)/c_p & H > c_p T_L + L_f \end{cases} \quad (15)$$

Considering the motion of the heat source  $v_s$  in  $y$ -direction, the heat equation in terms of temperature [63] can be given by

$$\frac{\partial T}{\partial t} = \frac{1}{\rho(T)c_p(T)} \nabla \cdot (k(T)\nabla T) + \frac{\dot{Q}'''(x,y,z,t)}{\rho(T)c_p(T)} + \frac{g_z w}{c_p(T)} - v_s \frac{\partial T}{\partial x_i} + \frac{\mu(T)}{\rho(T)c_p(T)} \Phi_V \quad (16)$$

where, the viscous dissipation term  $\Phi_V$  for 3-D case [63, 65] is defined as

$$\Phi_V = 2 \left[ \left( \frac{\partial u}{\partial x} \right)^2 + \left( \frac{\partial v}{\partial y} \right)^2 + \left( \frac{\partial w}{\partial z} \right)^2 \right] + \left( \frac{\partial u}{\partial y} + \frac{\partial v}{\partial x} \right)^2 + \left( \frac{\partial v}{\partial z} + \frac{\partial w}{\partial y} \right)^2 + \left( \frac{\partial w}{\partial x} + \frac{\partial u}{\partial z} \right)^2 - \frac{2}{3} \left( \frac{\partial u}{\partial x} + \frac{\partial v}{\partial y} + \frac{\partial w}{\partial z} \right)^2 \quad (17)$$

In the above equations,  $\rho$  is the density of the liquid melt pool,  $k$  is the thermal conductivity,  $c_p$  is the specific heat capacity,  $\mu$  is the absolute viscosity,  $g_z$  is the gravitational acceleration in  $z$ -direction,  $u$ ,  $v$ , and  $w$  are the velocity components in  $x$ -,  $y$ -, and  $z$ -directions, respectively. The fourth term on the right side of Eq. (16) is a source term due to the relative motion  $v_s$  between the heat source and the work piece. During the simulation, the solid cells of the domain are specified by the temperature below the solidus temperature and are assigned with very large value of viscosity. Therefore, the velocity of those cells becomes very small and the transportation terms in the heat equation can be neglected in the solid cells of the domain.

#### 4.4.1 Boundary and Initial Conditions

Since the EBAM process includes preheating of the entire domain to a temperature of 1003 K, the initial conditions are at  $t = 0$ ,  $u = v = w = 0$ , and  $T = T_{\text{preheat}} = 1003$  K, everywhere in the domain. The top surface is exposed to radiation at 298 K while the side walls and the bottom of the substrate are considered as adiabatic surfaces. For SLM, the initial temperature is 298 K and boundary conditions are same as the EBAM model. The top surface is exposed to radiation and convection at 298 K.

The Marangoni-driven flow [94] from the balance between the shear force and the surface tension at the top surface of the melt pool is described by Eqs. (18) and (19) [58].

$$\tau_{xz} = \sigma_T \left( \frac{\partial T}{\partial x} \right)_{Top} \quad (18)$$

$$\tau_{yz} = \sigma_T \left( \frac{\partial T}{\partial y} \right)_{Top} \quad (19)$$

where  $\tau_{xz}$  and  $\tau_{yz}$  are the Marangoni shear stresses due to the  $x$  and  $y$  components of velocity, respectively; and  $(\partial T/\partial x)$  and  $(\partial T/\partial y)$  are the spatial temperature gradients in the  $x$ - and  $y$ -directions, respectively. Furthermore,  $\sigma_T$  is the temperature coefficient of surface tension (also known as the Marangoni coefficient or the surface tension gradient) which is set as  $-2.6 \times 10^{-4}$  N/m-K at the top surface [58]

#### 4.5 Calculation of Viscosity

According to Pei *et al.* [95], the viscosity of a liquid metal at any temperature  $T$  can be calculated by the following relationship:

$$\mu(T) = C e^{\frac{E}{RT}} \quad (20)$$

where  $C$  is a constant,  $E$  is the activation energy, and  $R$  is the molar gas constant. The activation energy (in kcal/mol) can be represented as a function of the melting point  $T_m$  as follows:

$$E = 0.431 T_m^{1.348} \quad (21)$$

Now, at  $T = T_m$ , the viscosity (in cP or mPas) of a liquid metal can be calculated as follows:

$$\mu_m = 5.7 \times 10^{-6} \frac{(A_w T_m)^{1/2}}{V_m^{2/3}} \quad (22)$$

where  $A_w$  is the atomic weight and  $V_m$  is the atomic volume at  $T_m$ . When  $T = T_m$ , the value of the constant  $C$  in Eq. (20) can be found by substituting  $\mu = \mu_m$ . For the Ti-6Al-4V melt pool,  $E$  and  $\mu_m$  are found to be 11.585 kcal/mol and 3.41 cP [95], respectively, by substituting the melting temperature 1935 K, atomic weight 46.75 g/mol, and atomic volume  $11.265 \times 10^{-6}$  m<sup>3</sup>/mol [95] in Eqs. (20) – (22). Figure 4.5 shows the variation of viscosity of Ti-6Al-4V alloy with the change in temperature which is obtained by solving Eqs. (20) – (22).

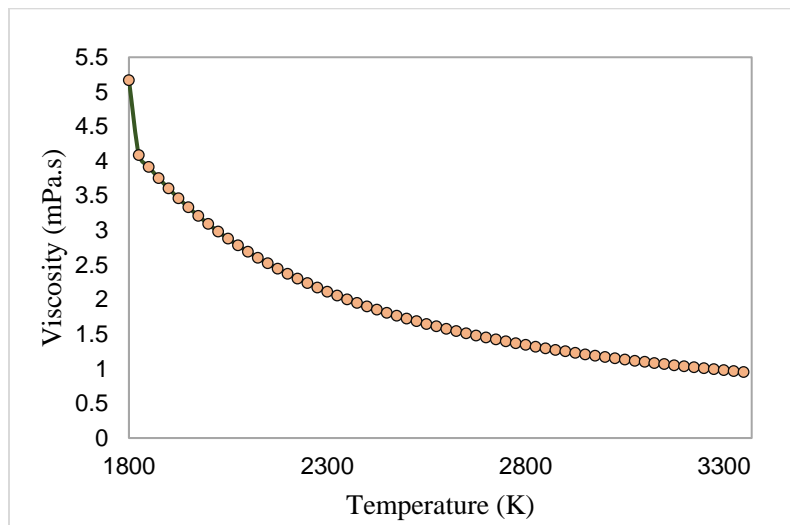


Figure 4.5: Temperature dependent viscosity of Ti-6Al-4V alloy

## Chapter 5

### Results and Discussions

This chapter contains the results for numerical modeling, experimental analyses, and the model validation by comparing the numerical results with experimental and analytical results. The interpretation of the results and other discussions are also embedded for thorough understanding.

#### 5.1 Numerical Results

The numerical results are obtained from the thermo-fluid modeling of the two processes. After representing individual studies, a comparison between the SLM and EBAM is illustrated with the modeling results.

##### 5.1.1 Simulation Results for the SLM Process

Numerical simulations for SLM are conducted using the UDFs for laser heat source and the thermo-physical properties of Ti-6Al-4V under several laser irradiation conditions. The parameters, shown in Table 5.1, are used to generate results for the thermo-fluid properties and melt-pool geometry for a wide range of process parameters and times. All the simulation results are obtained for the converged mesh size using a powder porosity level of 50%. The absorptivity and efficiency of the laser beam and the thickness of the powder layer are considered for the calculation of optical penetration depth. The convective heat transfer coefficient is set considering an argon gas environment above the top surface of the domain.

**Table 5.1: List of the SLM simulation parameters**

Parameters	Values
Solidus temperature, $T_S$ (K)	1878
Liquidus temperature, $T_L$ (K)	1938
Latent heat of fusion, $L_f$ (kJ/kg)	440
Spot size of laser beam, $\Phi$ (mm)	0.4, 0.058
Scanning speed, $v_s$ (mm/s)	100, 300, 330, 750, 1000
Laser power, $P_H$ (W)	200, 240
Initial temperature in SLM, $T_{SLM}$ (K)	298
Laser absorption efficiency, $\eta_t$	0.865
Powder porosity (%)	50
Powder layer thickness, $l_t$ (mm)	0.07
Beam penetration depth, $S$ ( $\mu\text{m}$ )	62.5
Convective heat transfer coefficient, $h$ ( $\text{W}/\text{m}^2\text{-K}$ )	10
Effective viscosity of liquid, $\mu$ (kg/m-s)	UDF
Specific heat, $c_p$ (J/kg-K)	UDF
Thermal conductivity, $k$ (W/m-K)	UDF
Emissivity, $\varepsilon$	UDF
Density, $\rho$ ( $\text{kg}/\text{m}^3$ )	UDF

The scanning speed, power, and spot sizes are varied to create several irradiation conditions. Table 5.2 shows the different laser irradiation conditions considered for the SLM analysis.

**Table 5.2: Different laser irradiation conditions for the powder layer thickness of 70  $\mu\text{m}$** 

Laser power (W)	Spot size ( $\mu\text{m}$ )	Scanning speed (mm/s)	Energy density ( $\text{J}/\text{mm}^3$ )	Laser interaction time (ms)
200	58	100	492.611	0.580
		300	164.204	0.193
		750	65.681	0.077
		1000	49.261	0.058
240	400	330	26	1.212

As shown in Table 5.2, the energy density and interaction time of the laser decrease significantly as the scanning speed increases, resulting in an incomplete melting of the powder layer. However, a higher energy density of 492.611 J/mm<sup>3</sup> is not recommended as it overmelts the target zone including the substrate. The energy density for the spot size of 0.4 mm gives a low value (26 J/mm<sup>3</sup>) when compared to the ones for 58 μm spot size and might seem inadequate for melting. However, the high laser interaction time (i.e., 1.212 ms) allows the material to absorb more heat and eventually aids in the melting process.

Based on Eq. (8), the calculated threshold value for  $\frac{kT_b\sqrt{\pi^3}}{A\sqrt{D}}$  is found  $3.95 \times 10^8 \text{ W}\sqrt{\text{s}}/\text{m}^2$  using the thermophysical parameters shown in Table 5.3. The absorptivity value is assumed as 0.36 based on the literature survey [65].

**Table 5.3: Thermophysical parameters for the keyhole mode calculation [65]**

Thermophysical parameters	Value
Boiling point, $T_b$ (K)	3315
Absorptivity, $A$	0.36
Thermal conductivity, $k$ (Wm <sup>-1</sup> K <sup>-1</sup> )	25.2
Thermal diffusivity, $D$ (m <sup>2</sup> s <sup>-1</sup> )	$1.07 \times 10^{-5}$

The values of  $\frac{P_{Laser}}{\sqrt{v_s}\phi^3}$  with the scanning speeds of 100, 300, 750 and 1000 mm/s are found  $14.3 \times 10^8$ ,  $8.27 \times 10^8$ ,  $5.23 \times 10^8$ , and  $4.53 \times 10^8 \text{ W}\sqrt{\text{s}}/\text{m}^2$ , respectively, which are higher than the threshold value. Therefore, all the laser processing conditions for the cases of 58 μm spot size belong to the keyhole mode. The keyhole threshold plot is shown in Fig. 5.1.

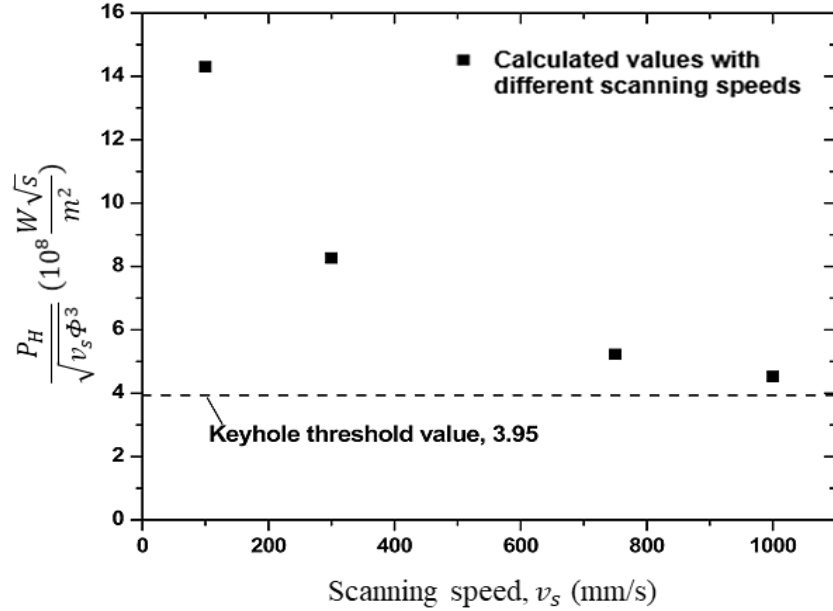


Figure 5.1: Keyhole mode confirmation for the laser melting of solid specimen [65]

#### 5.1.1.1 Variation of Thermal Properties

The laser beam scans the top surface in the  $y$ -direction. As a representative case, the combination of 240 W laser power, 330 mm/s scanning speed, and 0.4 mm spot size is selected to show the results. The contour plots for temperature at the top surface and in  $yz$ -plane (longitudinal section) along the laser scan path, and the cross-sectional thermal conductivity at  $y = 7.0$  mm and  $t = 0.016$  s are shown in Figs. 5.2 to 5.4. The maximum temperature in the melt pool is found 2574 K at the location where the laser beam is pointed. The segment of the domain that experiences temperatures above the liquidus temperature, is in the liquid state and becomes a part of the melt pool. Figure 5.4 shows that the thermal conductivity is higher in the liquid than that in the solid zones. The thermal conductivity of the powder layer (before the application of laser) is less than that of the solid substrate due to the porosity, i.e., presence of voids in the layer.

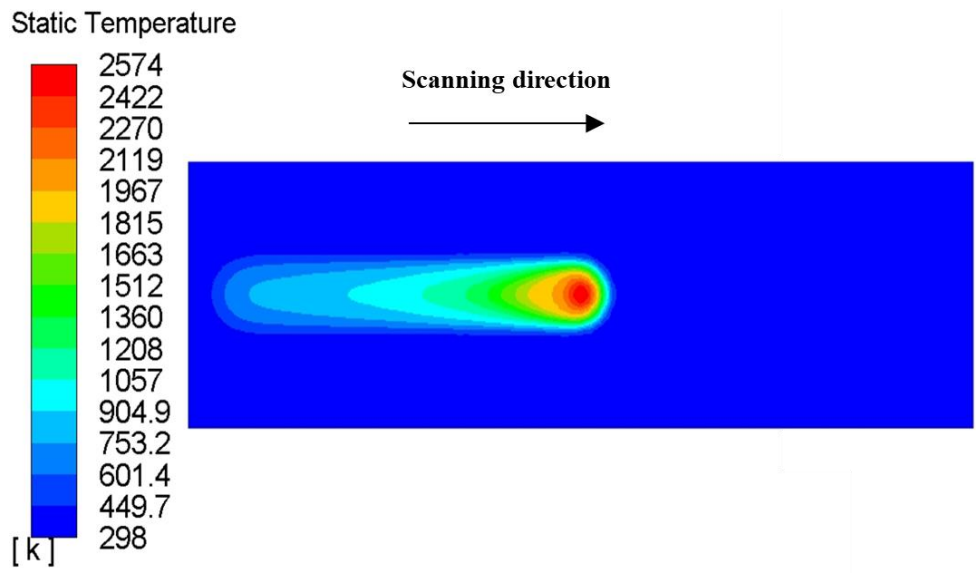


Figure 5.2: Contour plot for temperature (K) at the scanning path of the beam at  $t = 0.016$  s

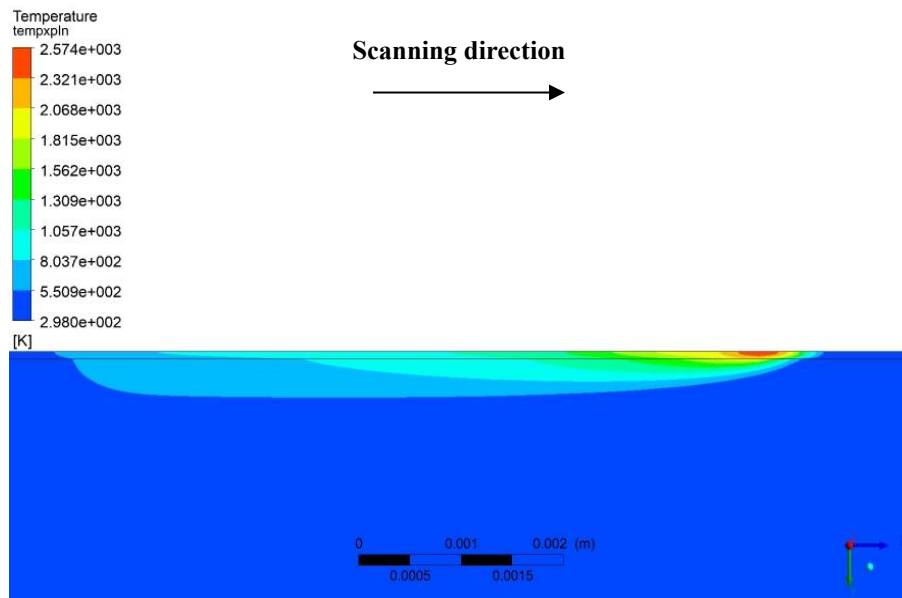


Figure 5.3: Contour plot for temperature (K) at the longitudinal section at  $t = 0.016$  s

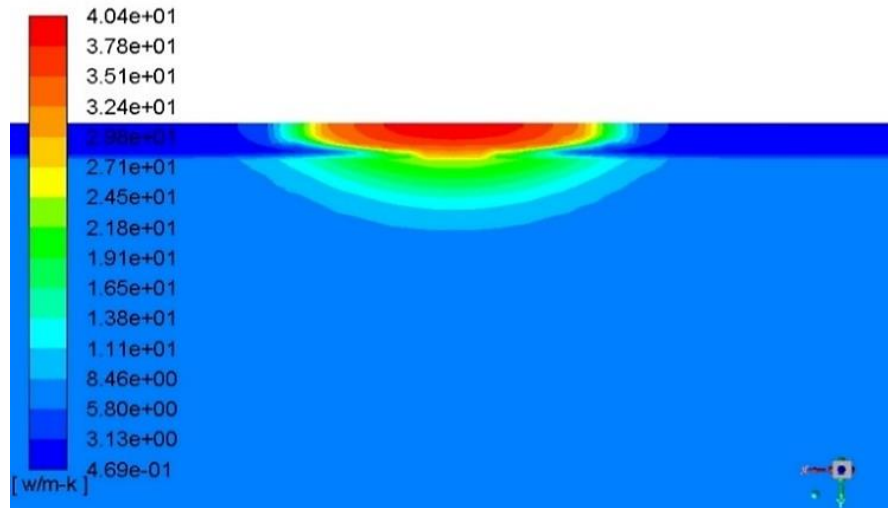


Figure 5.4: Contour plot for thermal conductivity (W/m-K) at the cross-section at  $t = 0.016$  s

### 5.1.1.2 Melt-Pool Geometry

The size of the melt pool depends largely on the properties of the heat source. The depth of the melt pool must be greater than the powder layer thickness in order to avoid partial or incomplete melting. Therefore, optimization of the process parameters is necessary for an efficient manufacturing strategy which can be achieved by studying the melt-pool evolution.

Figure 5.5 shows the melt-pool dimensions at  $y = 7.0$  mm ( $t = 0.016$  s) for a laser power of 240 W, a scanning speed of 330 mm/s, and a spot size of 0.4 mm. The melt-pool dimensions, especially the depth and width, suggest that the laser melting in this case belongs to the conduction mode.

At a given laser power and spot size, the melt-pool volume decreases as the scanning speed increases. The variations of melt-pool width and depth with the change in scanning speeds are shown in Fig. 5.6, where the results are obtained for a laser power of 200 W, a spot size of 58  $\mu\text{m}$ , and a powder layer thickness of 70  $\mu\text{m}$ . The melt-pool width and depth at 1000 mm/s

scanning speed indicate a conduction mode while the dimensions in other three scanning speeds (100, 300, and 750 mm/s) fall under keyhole mode.

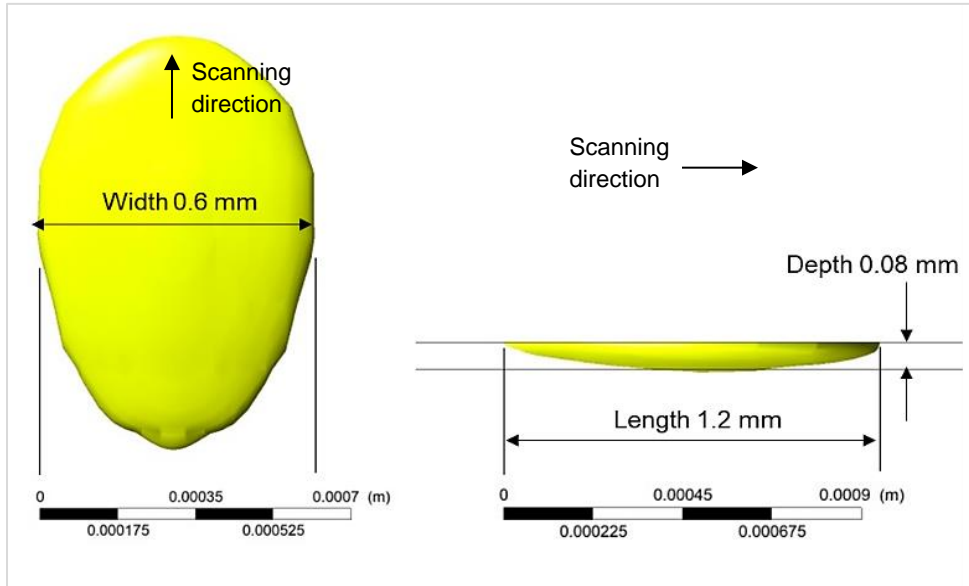


Figure 5.5: Melt-pool geometry for  $26 \text{ J/mm}^3$  energy density and  $1.212 \text{ ms}$  laser interaction time where the left image is viewed from the bottom of the domain and the right one is viewed at the longitudinal section at  $y = 7.0 \text{ mm}$ , and  $t = 0.016 \text{ s}$

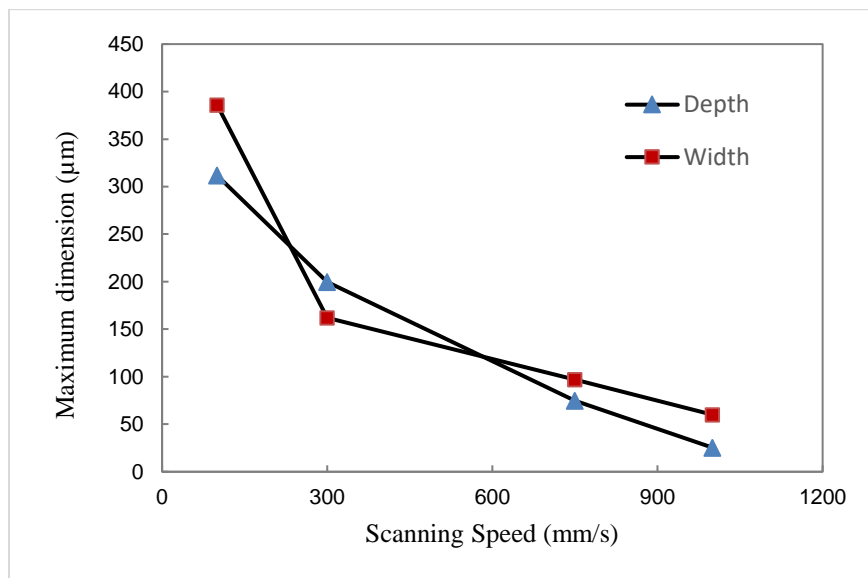


Figure 5.6: Simulated melt-pool width and depth at  $58 \mu\text{m}$  spot size and  $200 \text{ W}$  laser power

## 5.1.2 Simulation Results for EBAM

### 5.1.2.1 Variation of Thermo-Fluid Properties

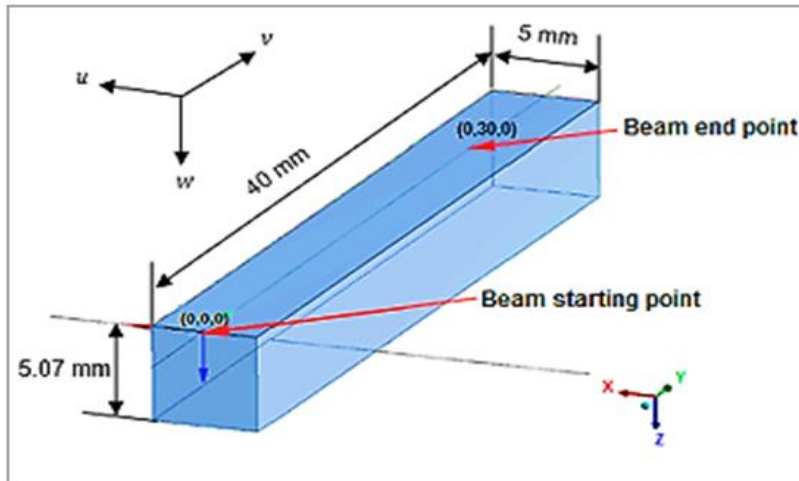
The EBAM simulations are conducted using the UDFs and the solver algorithm of ANSYS Fluent to generate results for the time-dependent-thermo-fluid properties for a wide range of times. The specifications of the heat source and other simulation parameters are listed in Table 5.4. Three different speeds including 330 mm/s, 630 mm/s, and 930 mm/s are used to observe the change in properties keeping the other input parameters constant. Results are presented mainly for the speed of 330 mm/s and the effects of changing the beam scanning speed on the melt-pool geometry are discussed with necessary illustrations. The geometry of the model is modified to a higher scale, i.e., 40 mm × 5 mm × 5.07 mm, in order to track the total tailing effect of the melt pool on the top surface of the domain.

**Table 5.4: List of the EBAM simulation parameters [62]**

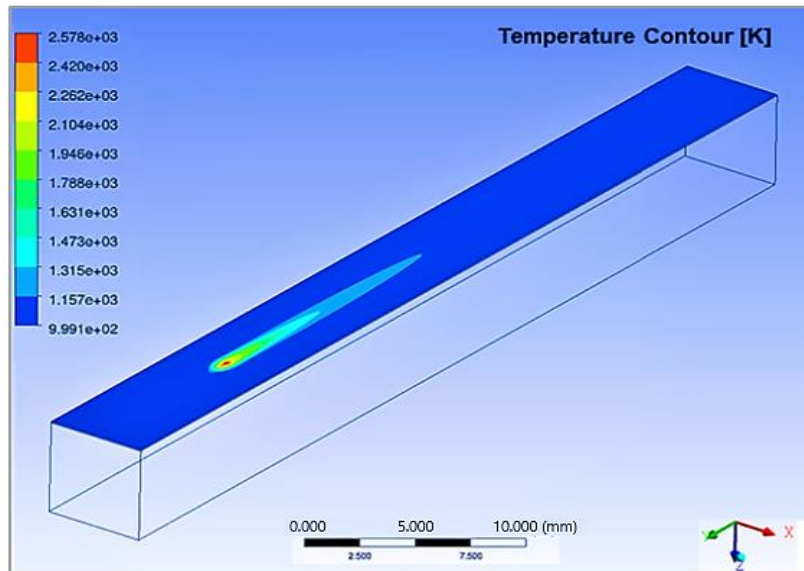
Parameters	Values
Solidus temperature, $T_S$ (K)	1878
Liquidus temperature, $T_L$ (K)	1938
Latent heat of fusion, $L_f$ (kJ/kg)	440
Electron beam diameter, $\Phi$ (mm)	0.4
Beam scanning speed, $v_s$ (mm/s)	330, 630, and 930
Acceleration voltage, $V$ (kV)	60
Current, $I_b$ (mA)	4
Preheat temperature, $T_{preheat}$ (K)	1003
Beam efficiency, $\eta$	0.9
Powder Porosity (%)	50
Effective viscosity of Liquid, $\mu$ (kg/m-s)	0.049
Specific heat, $c_p$ (J/kg-K)	UDF
Thermal conductivity, $k$ (W/m-K)	UDF
Emissivity, $\varepsilon$	UDF
Density, $\rho$ (kg/m <sup>3</sup> )	UDF

Figure 5.7 (a) represents the modified geometry for the EBAM model. This model is used to show the individual results for the EBAM process. However, the geometry presented in Fig.

3.7 in Chapter 3 is used to study the comparison between the SLM and EBAM models. Figure 5.7 (b) shows the contour of temperature along the beam path at  $y = 29.7$  mm (at  $t = 0.09$  s) on the top surface of the domain.



(a)



(b)

Figure 5.7: (a) Modified geometry of the EBAM model, and (b) contour plot for temperature (K) at the scanning path of the beam at  $t = 0.09$  s

Along the  $y$ - $z$  plane corresponding to the origin (i.e., the longitudinal section), the temperature contour when the electron beam is at  $y = 29.7$  mm, is shown in Fig. 5.8.

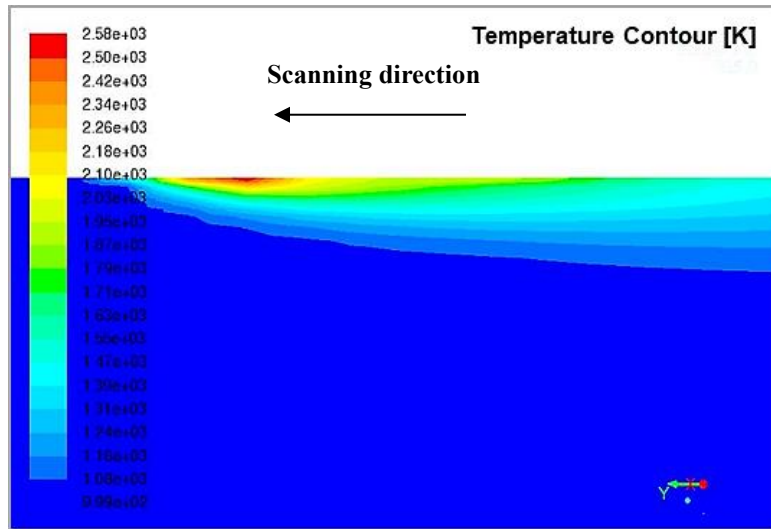


Figure 5.8: Contour plot for temperature (K) at the longitudinal section at  $t = 0.09$  s

To visualize the results along the  $x$ - $z$  plane, a cross-section is considered at  $y = 29.7$  mm which corresponds to the 2-D representation of the model as depicted earlier in chapter 3. The temperature contour at the cross-section is shown in Fig. 5.9 which is symmetric relative to the center of the electron beam.

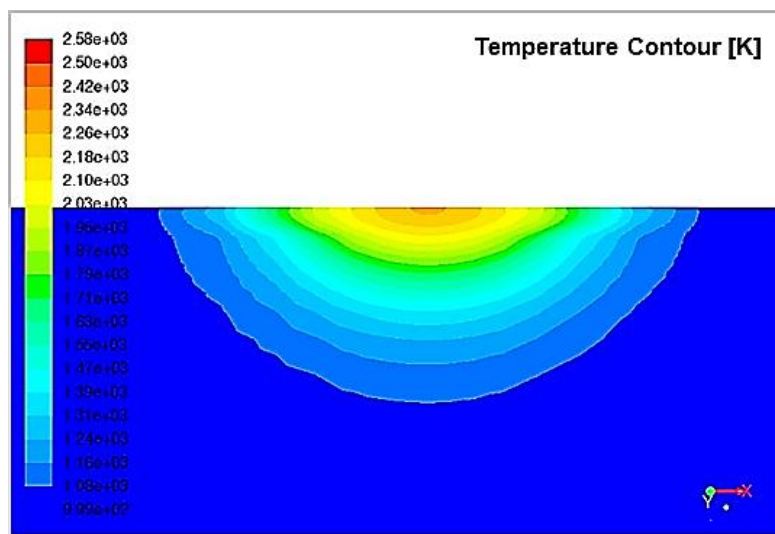


Figure 5.9: Contour plot for temperature (K) at the cross-section at  $t = 0.09$  s

As the density, specific heat capacity, thermal conductivity, and enthalpy are functions of temperature, the variation of these properties can be observed clearly inside the computational domain from which the location and growth of the melt pool can be identified. As the temperature increased, density decreased linearly from the bottom to the top of the liquid melt pool. The contour plots for density in both the longitudinal section and cross section at  $t = 0.09$  s are shown in Figs. 5.10 and 5.11, respectively.

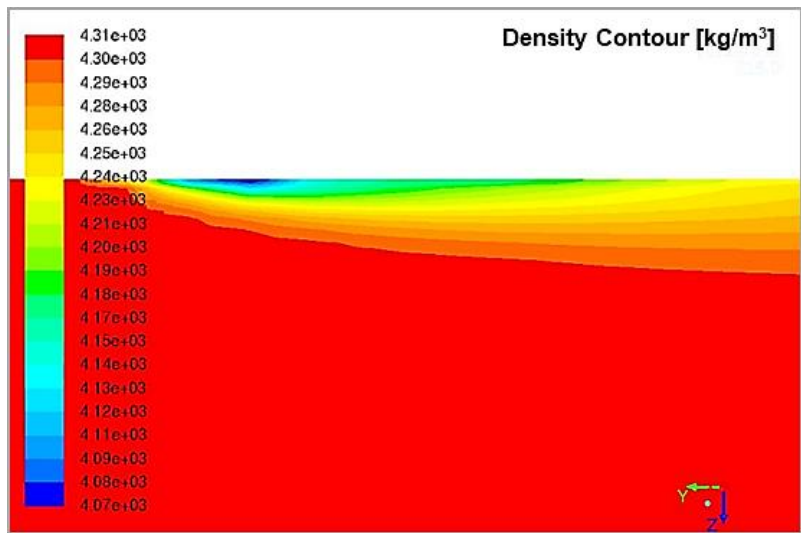


Figure 5.10: Contour plot for density (kg/m<sup>3</sup>) at the longitudinal section at  $t = 0.09$  s

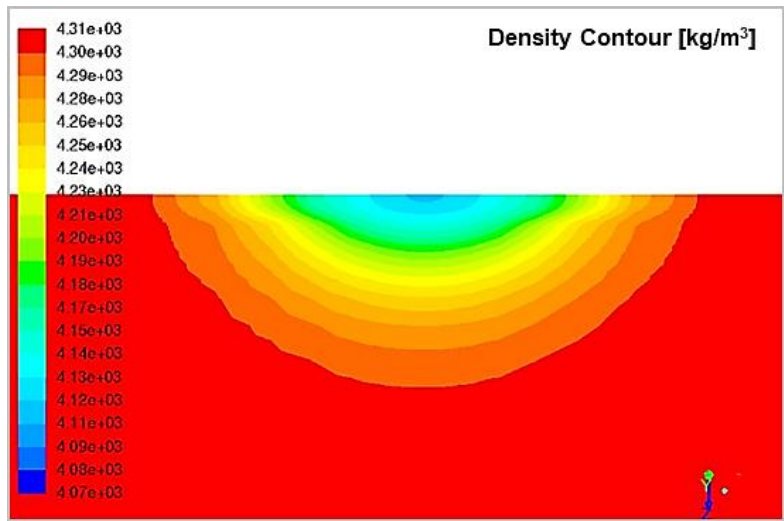


Figure 5.11: Contour plot for density (kg/m<sup>3</sup>) at the cross-section at  $t = 0.09$  s

On the other hand, the values of thermal conductivity, specific heat capacity, and enthalpy increased as the temperature increased. Since the liquid metal has higher values of these three thermal properties, the position of the melt pool and the estimation of its size can be identified from the contour plots along the longitudinal section and cross-section of the domain. Figures 5.12–5.14 show the variation of thermal conductivity, specific heat capacity, and enthalpy, respectively, along the longitudinal section in the  $y$ - $z$  plane at  $t = 0.09$  s. The UDFs containing macros of the temperature-dependent functions play a key role in the determination of these properties. When the Fluent solver solves the mathematical model, the solutions for temperature at various nodes are fed into the functions to generate the results for all the temperature-dependent properties. The thermal conductivity of the powder layer is significantly lower than that of the solid substrate. The porosity of powder is liable for the decreased value of thermal conductivity which can be seen in the powder zones around the melt pool.

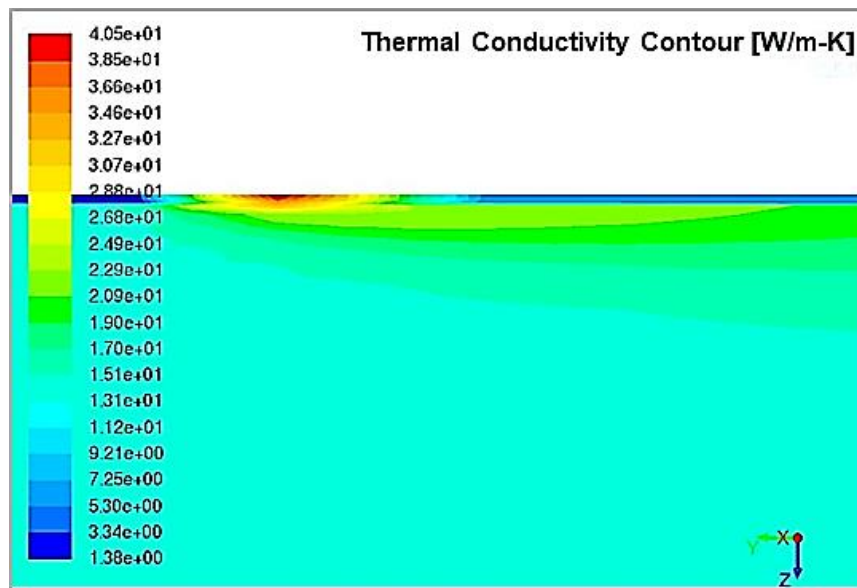


Figure 5.12: Contour plot for thermal conductivity (W/m-K) at the longitudinal section at  $t = 0.09$  s



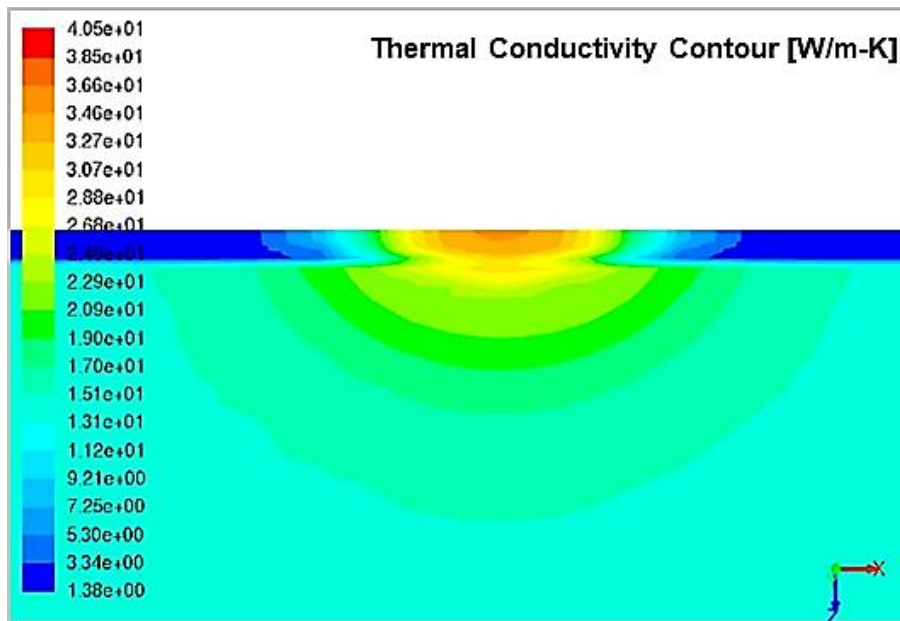


Figure 5.15: Contour plot for thermal conductivity (W/m-k) at the cross-section at  $t = 0.09$  s

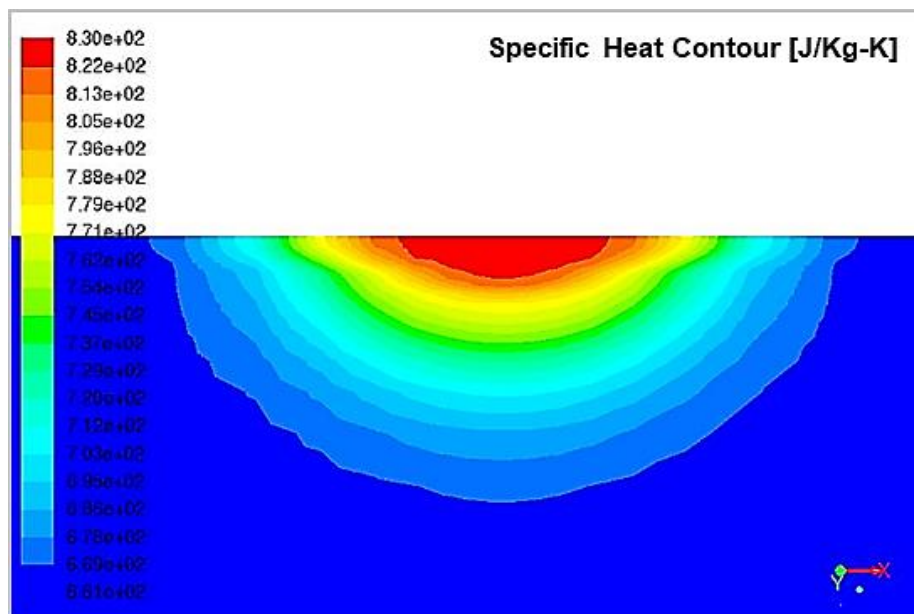


Figure 5.16: Contour plot for specific heat (J/kg-K) at the cross-section at  $t = 0.09$  s

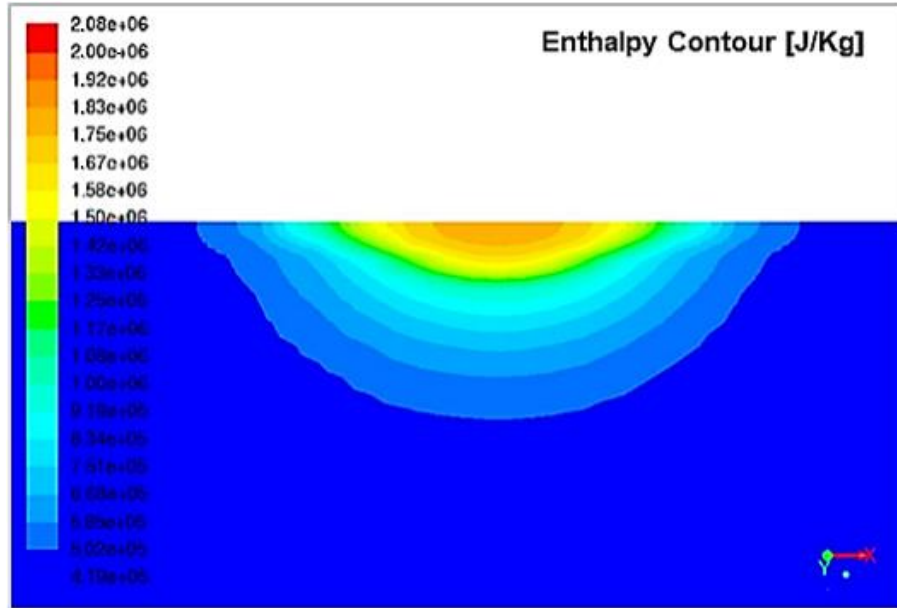


Figure 5.17: Contour plot for enthalpy (J/kg) at the cross-section at  $t = 0.09$  s

### 5.1.2.2 Melt-Pool Geometry for EBAM

The maximum width, depth, and length of the melt pool for a beam diameter of 0.4 mm with 240 W power and 330 mm/s scanning speed are 0.6 mm, 0.12 mm, and 2.1 mm, respectively at  $t = 0.09$  s. The maximum width of the melt pool during scanning is 0.6 mm which is wider than the electron beam diameter of 0.4 mm and the depth is also more than the powder layer thickness. However, obtaining very deep penetration, i.e., well below the powder layer thickness, is not necessary as the beam starts penetrating the substrate. The simulation results for the maximum length and width of the melt pool at the scanning speed of 330 mm/s are shown in Fig. 5.18 while the maximum depth at that speed is shown in Fig. 5.19. These results are obtained by the ANSYS CFD-Post which is a post-processing platform to visualize the results solved by the Fluent solver.

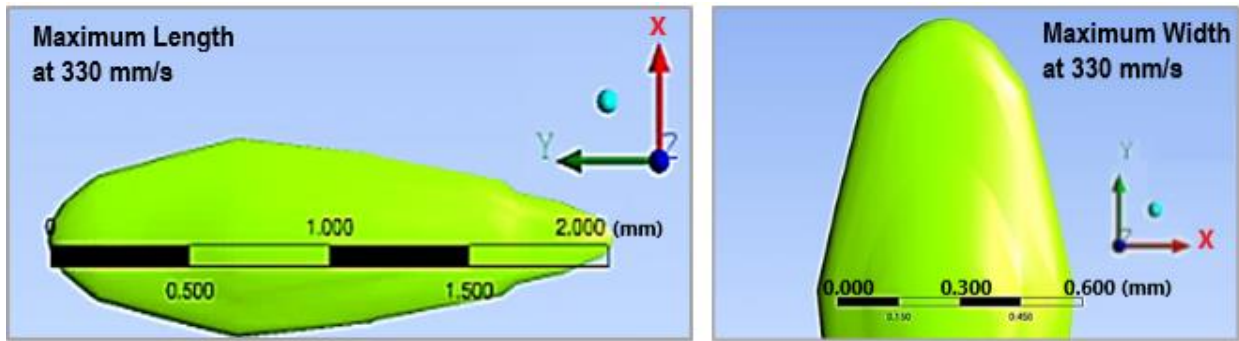


Figure 5.18: The maximum length and width of the melt pool at  $t = 0.09$  s as viewed from the top and bottom, respectively

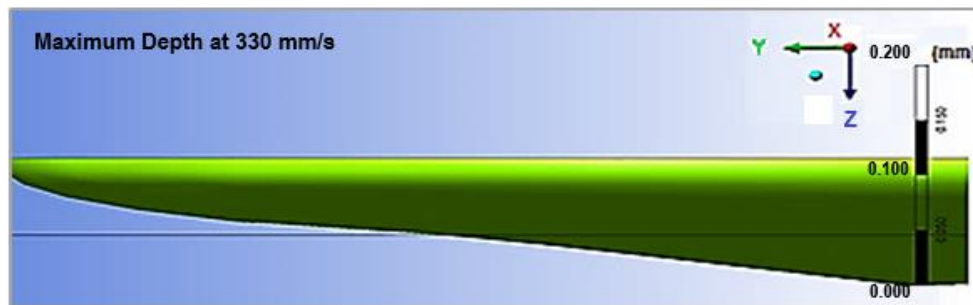


Figure 5.19: The maximum depth of the melt pool at  $t = 0.09$  s as viewed from the longitudinal section

Keeping the other parameters same, if the scanning speed is increased, the melt pool gets smaller in size, i.e., the volume decreases. The maximum width and depth decrease but the maximum length increases due to the tailing effect. Figure 5.20 shows the contour plots of temperature distribution at the top surface for two different scanning speeds (630 mm/s and 930 mm/s) where the effect of the increased scanning speed on the size of the melt pool is visible. The tailing effect along the scanning direction is comparatively long for 930 mm/s but the width became smaller than the one at 630 mm/s.

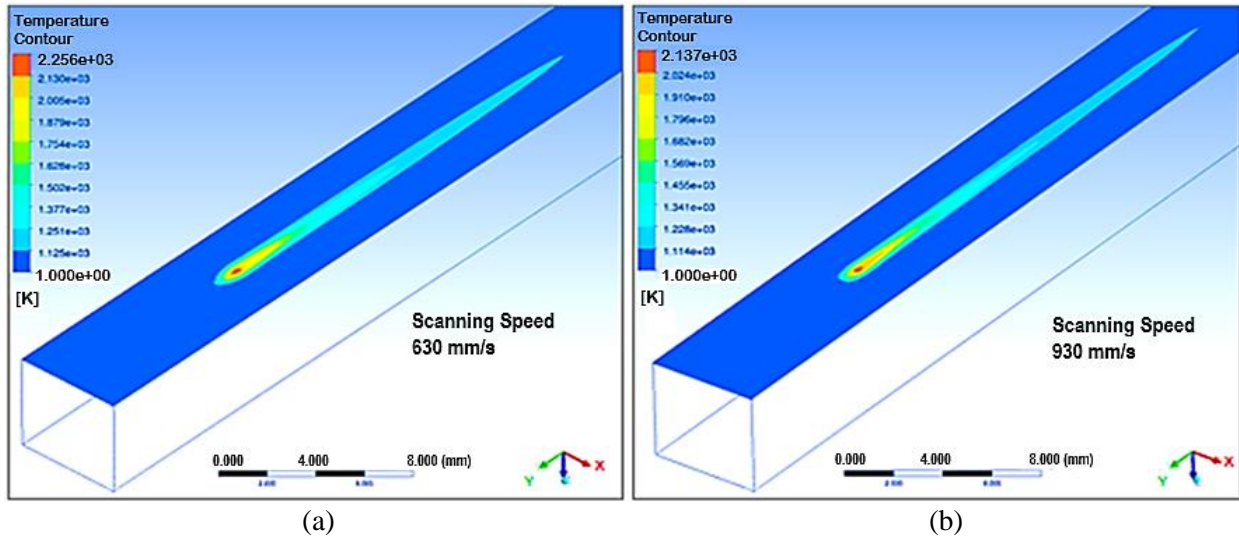


Figure 5.20: Estimation of the melt-pool size from the contour plot for temperature (K) on the scanning path of the beam at (a) 630 mm/s, and (b) 930 mm/s

A comparison of different melt-pool sizes at three different electron beam scanning speeds is shown in Fig. 5.21 where the beam diameter is kept at 0.4 mm and the beam power is set at 240 W. The maximum width and depth of the melt pool decreased as the scanning speed is increased. The melt-pool dimensions for these three cases are observed at  $t = 0.09$  s. The geometries of the melt pool are achieved for a powder porosity of 50%. The width of the melt pool does not significantly vary with the change in porosity due to the large thermal resistance [51, 62] of the porous powder on both sides of the scan path. However, length and depth can vary with the variation of the porosity. For a given scanning speed and diameter of the electron beam, significant increase in the melt-pool volume is found with the increase in beam power.

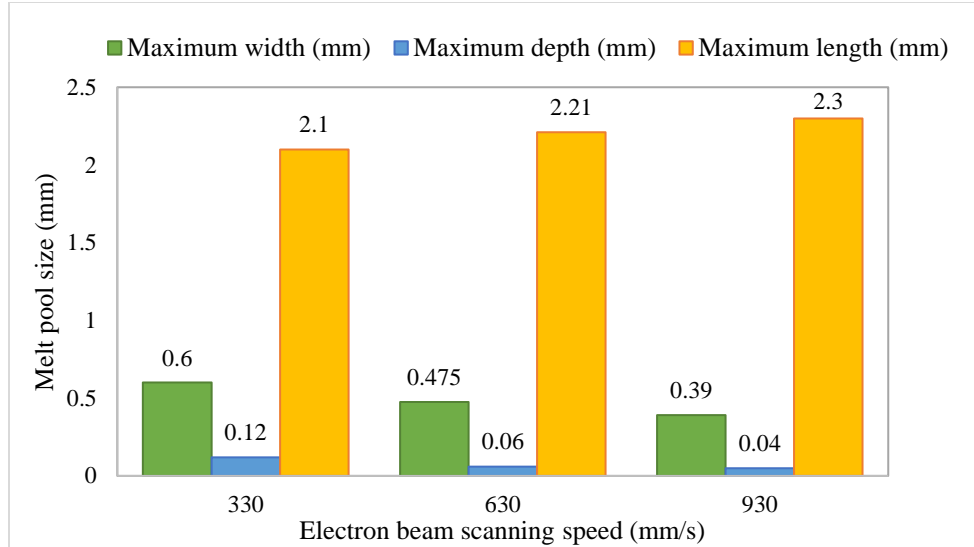


Figure 5.21: Variation of maximum width, depth, and length of the melt pool (mm) with the increase in the beam scanning speed (mm/s) at  $t = 0.09$  s

### 5.1.3 Comparison between the SLM and EBAM Processes

#### 5.1.3.1 Variation of Thermal Properties

The comparison between the SLM and EBAM processes is conducted using the geometry shown in Fig. 3.6 in Chapter 3 (which is same as the SLM model). To make a valid comparison, the same irradiation condition is obtained for both SLM and EBAM by choosing 240 W power, 0.4 mm beam diameter, and of 330 mm/s scanning speed. Figure 5.22 shows the contour of temperature along the scan path on the top surface of the powder-bed for both SLM and EBAM process. In both cases, the heat source scans the top surface in  $y$ -direction. For SLM, the temperature contour at the top surface when the laser beam is at  $y = 7.5$  mm ( $t = 0.0167$  s) is shown in Fig. 5.22 (a). Similarly, for EBAM, the temperature contour at the top surface when the electron beam is at  $y = 7.5$  mm is shown in Fig. 5.22 (b). The melt region is longer in the contour for EBAM than that in SLM.

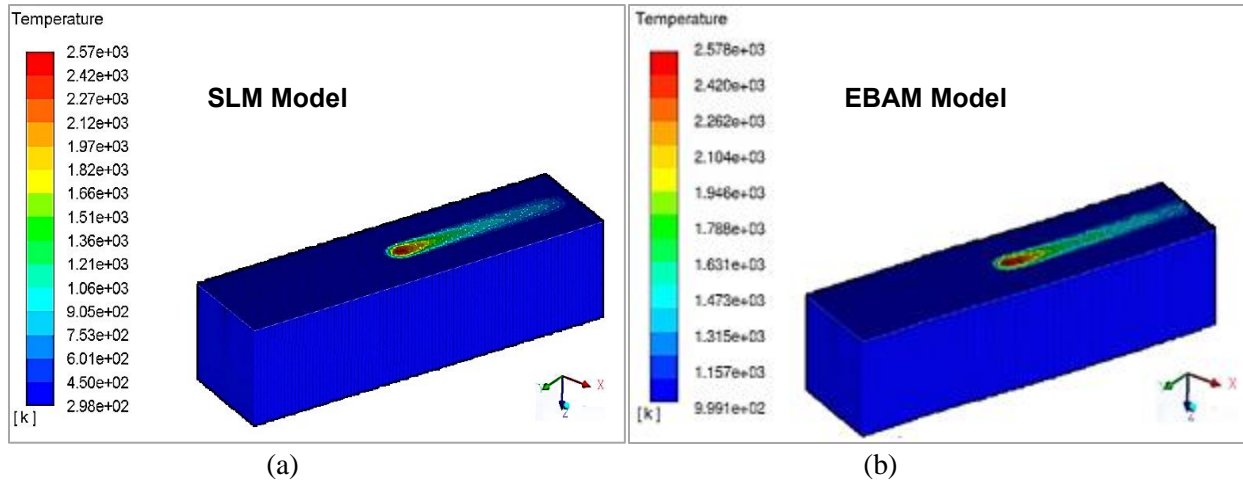


Figure 5.22: Contour plots for temperature (K) at the top surface at  $y = 7.5$  mm in the (a) SLM and (b) EBAM models

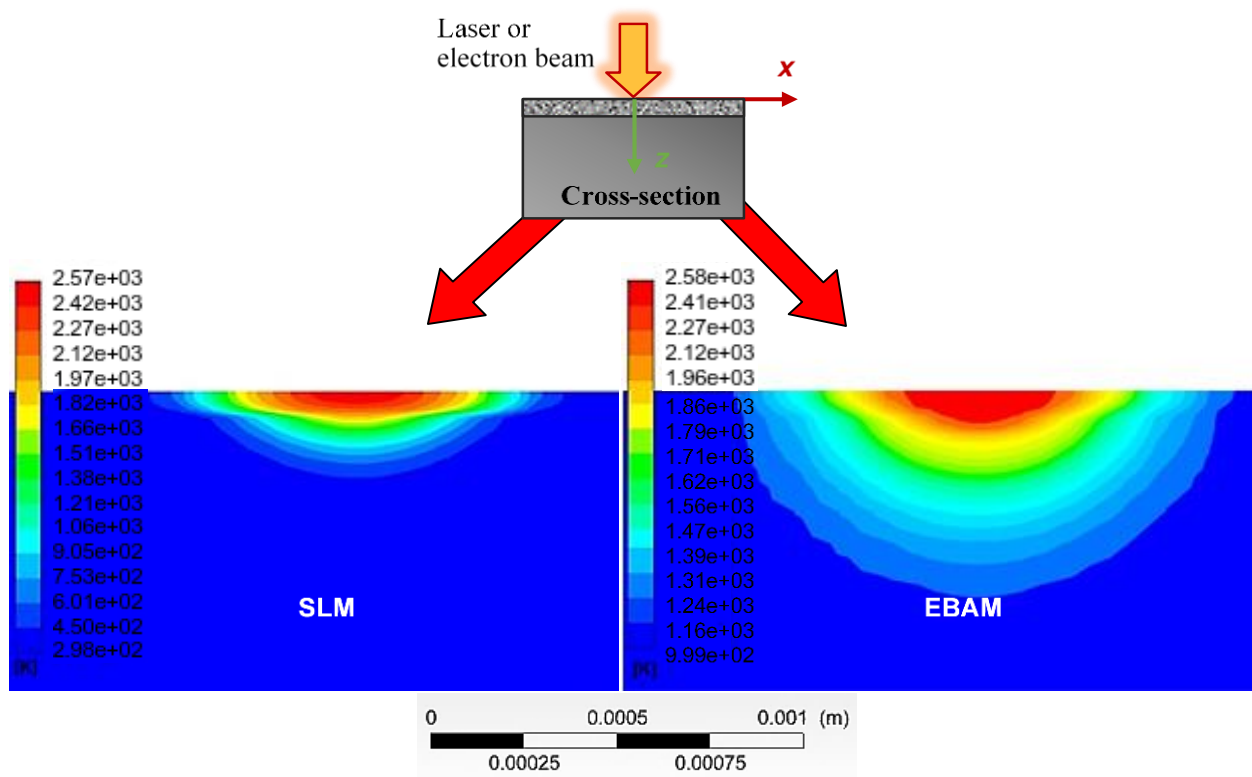


Figure 5.23: Contour plots for temperature (K) at the cross-section at  $y = 7.5$  mm in the SLM and EBAM models

In order to compare the results along the  $xz$ -plane, a cross-section is considered at  $y = 7.5$  mm ( $t = 0.0167$  s) which corresponds to a 2-D representation as shown in Figs. 5.23 to 5.25. The

temperature contour at the cross-section for SLM and EBAM are shown in Fig. 5.23. As the temperature increases, density decreases in the liquid melt pool. The results for density showed same pattern as presented by Rahman *et al.* [62]. Unlike density, the thermal conductivity, specific heat capacity, and enthalpy experienced an increase in their values as the temperature increased in the domain. The thermal conductivity of the powder layer is less than that of the solid substrate. The porosity of the powder reduces the thermal conductivity. Contour plots for thermal conductivity in SLM and EBAM are shown in Figs. 5.24 (a) and 5.24 (b), respectively.

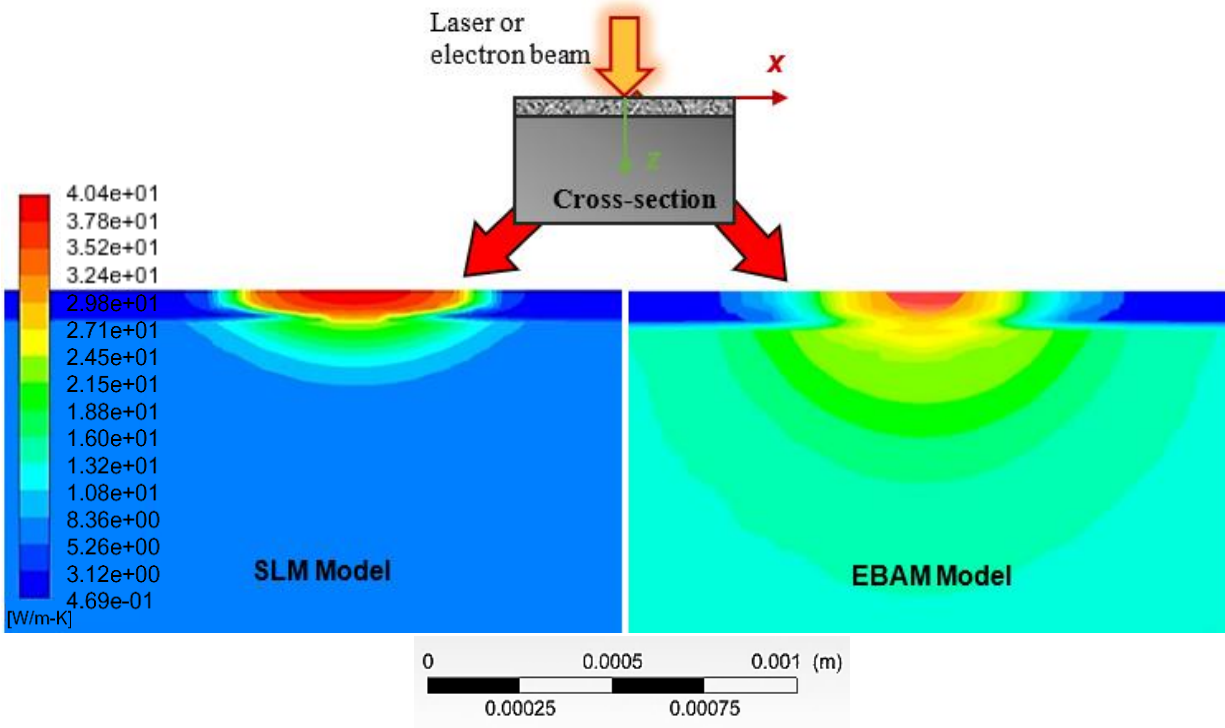


Figure 5.24: Contour plots for thermal conductivity (W/m.K) at the cross-section at  $y = 7.5$  mm in the SLM and EBAM models

As the enthalpy is proportional to temperature, the contour plots for enthalpy in SLM and EBAM have similar patterns as shown in Fig. 5.23. Figures 5.25 (a) and 5.25 (b) represent the enthalpy distributions along the cross-section in SLM and EBAM, respectively. All these SLM

and EBAM modeling results are obtained at similar irradiation conditions for laser and electron beam to show a valid comparison.

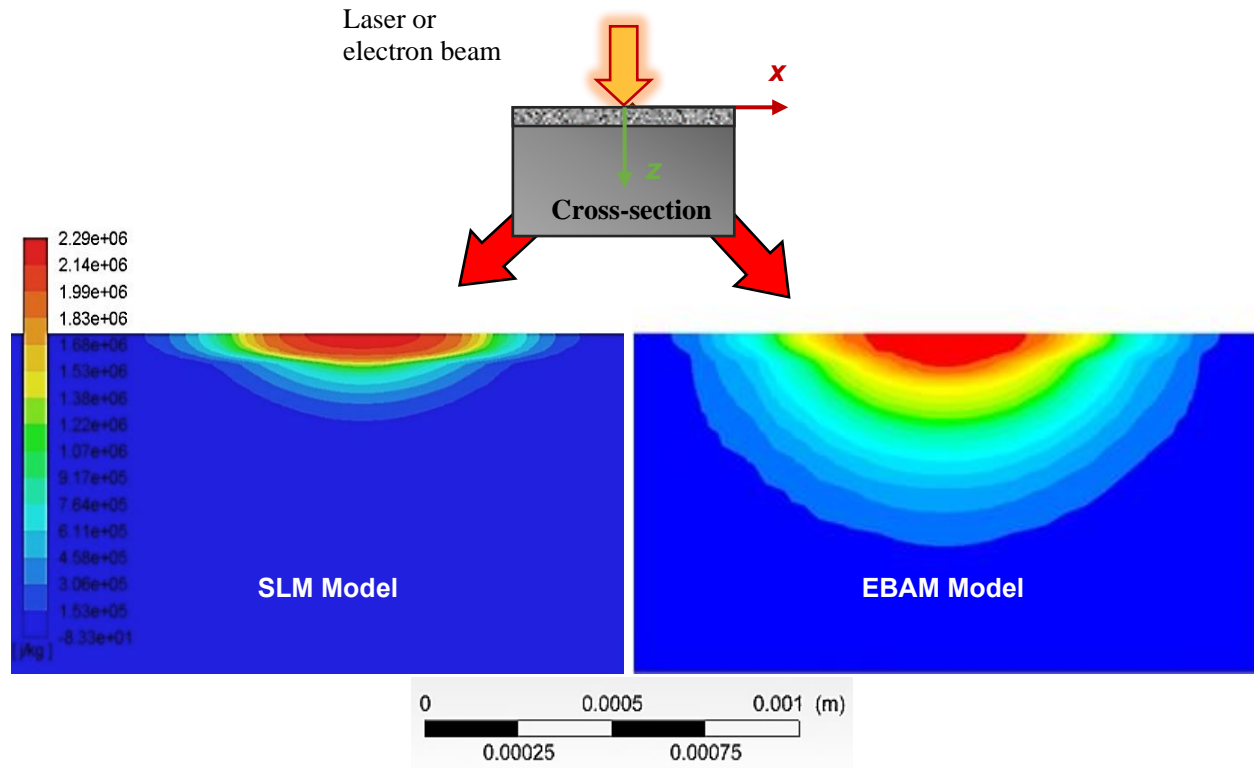


Figure 5.25: Contour plots for enthalpy (J/kg) at the cross-section at  $y = 7.5$  mm in the SLM and EBAM models

### 5.1.3.2 Melt-Pool Geometry

The size of the melt pool depends on the properties of the material, processing parameters, energy absorption, and thermo-fluid interactions. For a beam diameter of 0.4 mm with 240 W power and 330 mm/s scanning speed, i.e., under the same energy density of  $26 \text{ J/mm}^3$ , the results for the maximum length, width, and depth of penetration of the melt pool at  $y = 7.5$  mm ( $t = 0.0167$  s) for SLM and EBAM are shown in Table 5.5.

**Table 5.5: Comparison of melt-pool dimensions at  $y = 7.5$  mm**

Process	$E_D = 26 \text{ J/mm}^3$ and $t_i = 1.212 \text{ ms}$		
	Length (mm)	Width (mm)	Depth (mm)
SLM	1.2	0.6	0.08
EBAM	2.1	0.605	0.12

The simulation results for the lengths and widths of the melt pool in SLM and EBAM are shown in Fig. 5.26. The melt-pool geometries are achieved under the same irradiation conditions for both the SLM and EBAM processes.

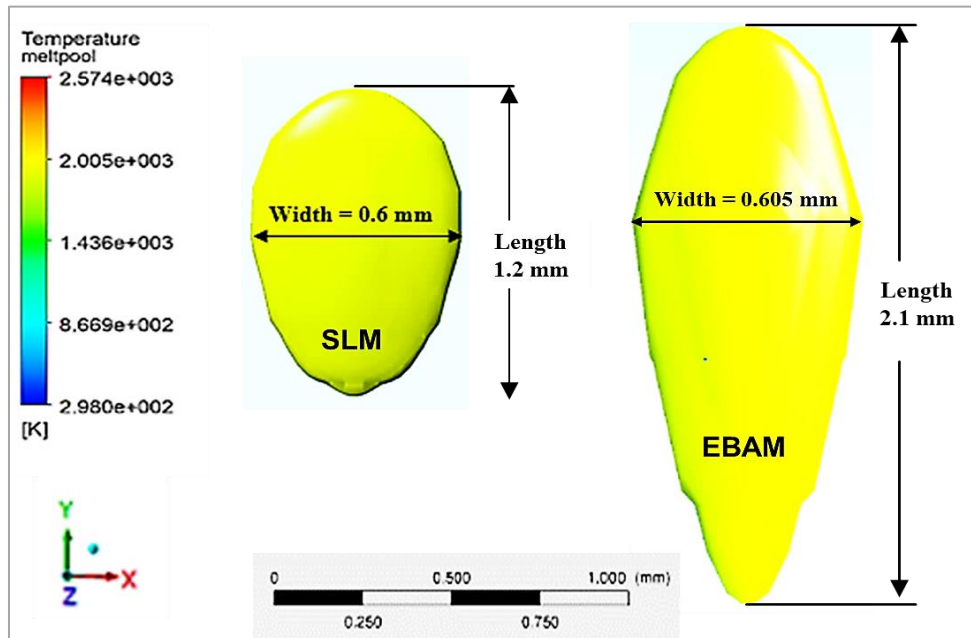


Figure 5.26: The maximum length and width (as viewed from the bottom) of the melt pool at  $y = 7.5$  mm

A parametric study on the effects of processing parameters on the evolution of the melt pool is also conducted with the numerical simulations for SLM and EBAM processes. First, the effect of increasing the power of the laser and electron beams on the depth of penetration of the melt pool is investigated while keeping the same spot size of 0.4 mm and scanning speed of 330

mm/s. As expected, the depth of the melt pool increases with the increase in beam power. The comparison of the melt-pool depth in EBAM and SLM processes are shown in Fig. 5.27.

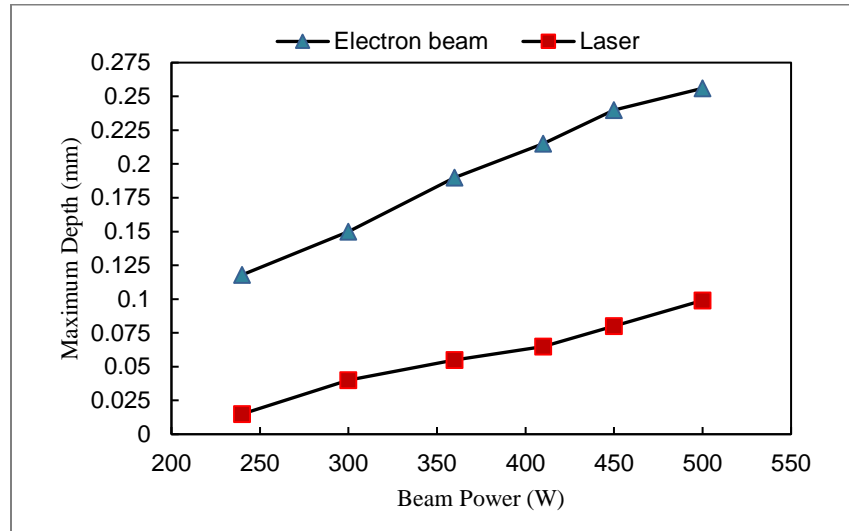


Figure 5.27: The maximum depths of the melt pool at different powers of the heat source

In contrast to the beam power, the depth of the melt pool decreases as the scanning speed increases at a given power and a spot size of the laser or electron beam. The simulation results for melt-pool depth versus scanning speed for SLM and EBAM at a power of 240 W and a spot size of 0.4 mm are shown in Fig. 5.28. Results show that the melt pool depth is more sensitive to the change in beam power as compared to the change in scanning speed at a given spot size. For instance, due to an increase of 127.27% of the scanning speed from 330 mm/s to 750 mm/s in the SLM model, the percentage of decrease in melt-pool depth is 55% (as shown in Fig. 5.28). However, a power increase of 87.5% from 240 W to 450 W in the SLM model results in a 433.33% increase in the melt-pool depth which is calculated from the values shown in Fig. 5.27. Therefore, the variation in melt-pool depth due to the change in power is significantly larger than the variation caused by the change in scanning speed.

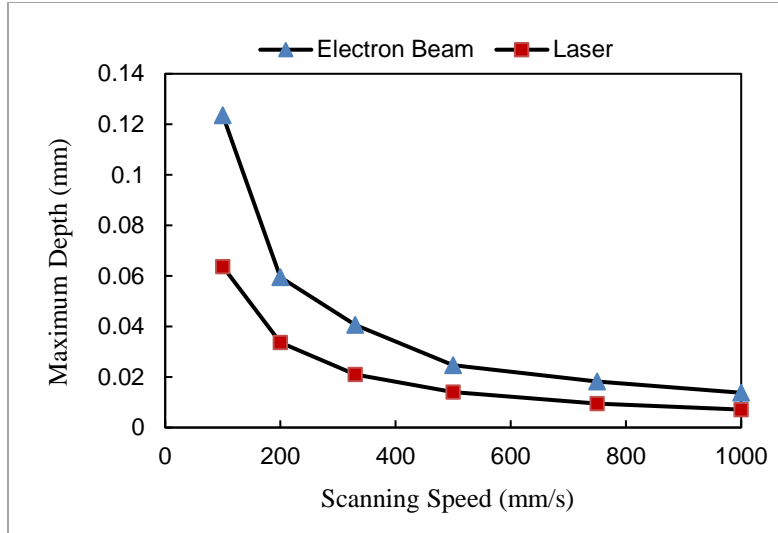


Figure 5.28: The maximum depths of the melt pool at different scanning speeds of the heat source

The powder porosity is considered 50% for both cases. The width of the melt pool does not significantly vary with porosity due to the large thermal resistance of the porous powder on both sides of the scan path. However, the length and depth of the melt pool can vary with the variation of the porosity and beam scanning speed.

### 5.1.3.3 Heating and Cooling Rates

In order to determine the heating and cooling rate for the given specifications of the laser and electron beam, a point at  $y = 5$  mm on the top surface along the scan path is selected to observe the variation of temperature with respect to time. If the temperature of the point is above the liquidus temperature (1938 K) then it is completely in the liquid state. On the contrary, any temperature below the solidus temperature (1878 K) indicates the solid state of that point. The Ti-6Al-4V melt pool in SLM and EBAM cools down rapidly due to the combined heat transfer. Figures 5.29 (a) and 5.29 (b) represent the heating and cooling of the point at  $(x, y, z) = (0, 5$  mm, 0) with respect to time for SLM and EBAM, respectively, where the time count starts when

the laser or electron beam strikes the point. The heating and cooling rates for SLM and EBAM are shown in Fig. 5.30 (a) and 5.30 (b), respectively.

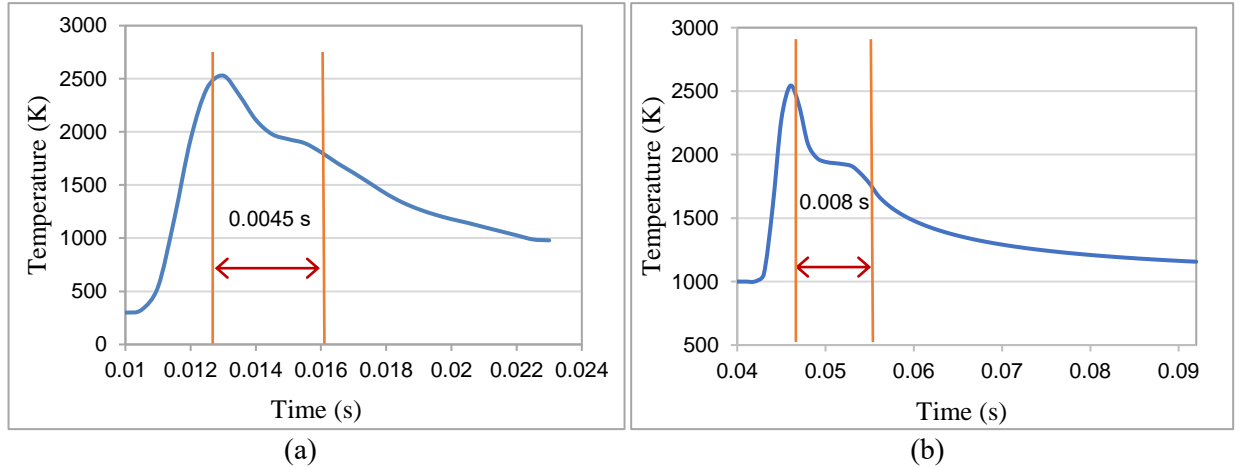


Figure 5.29: Variation of temperature with time at a fixed point during the (a) SLM and (b) EBAM processes

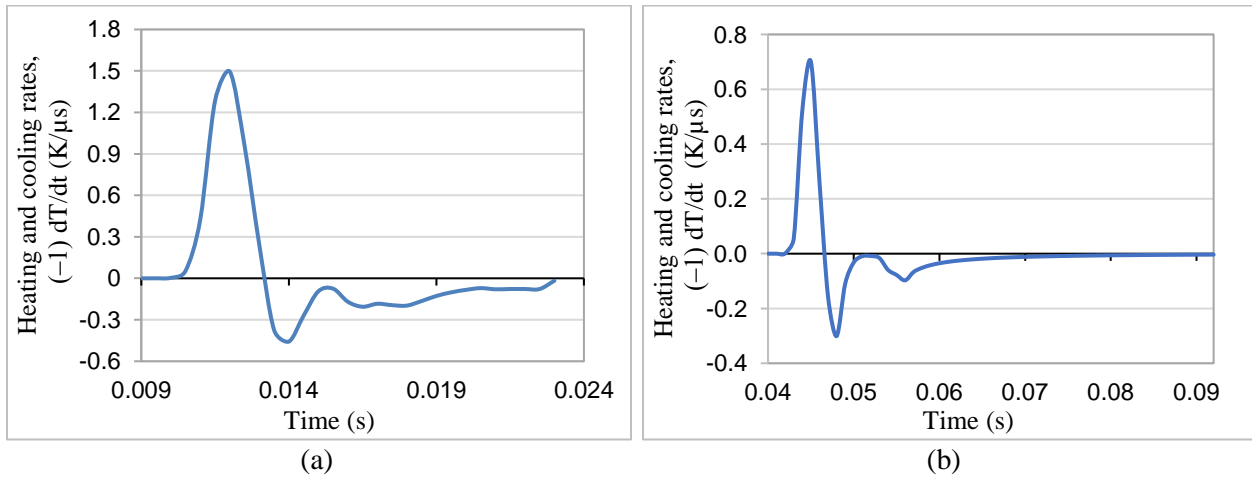


Figure 5.30: Heating and cooling rates versus time plots for the (a) SLM and (b) EBAM processes

Under the same energy density of  $26 \text{ J/mm}^3$  and laser interaction time of 1.212 ms, the liquid melt pool cooled down from the maximum temperature to the solidus temperature in 0.008 s for EBAM and in 0.0045 s for SLM. However, heat is generally trapped in the solidified scanned region which results in the trailing effect as shown earlier in the temperature contours on

the top surface. The liquid lifetime (i.e., the time duration from the start of melting to the beginning of solidification) decreases as the energy density or the laser interaction time decreases. The faster the scanning speed, the shorter the liquid lifetime.

#### 5.1.3.4 Velocity inside the Melt Pool

The simulation results for the velocity distribution inside the melt-pool obtained from the SLM and EBAM models are also compared under the same energy density of  $26 \text{ J/mm}^3$  and heat source interaction time of  $1.212 \text{ ms}$ . The velocity of liquid inside the melt pool in SLM is higher than that in EBAM due to greater convection in SLM. Along the  $yz$ -plane corresponding to the origin (i.e., the longitudinal section), the velocity contours inside the melt pool when the laser and electron beam are at  $y = 7.5 \text{ mm}$  ( $t = 0.0167 \text{ s}$ ) are shown in Fig. 5.31.

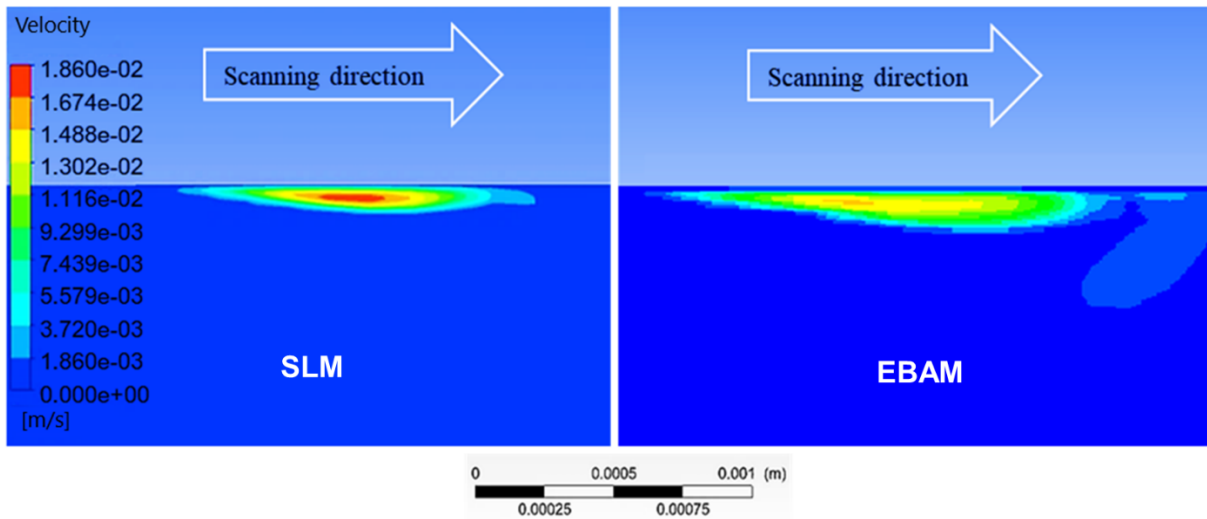
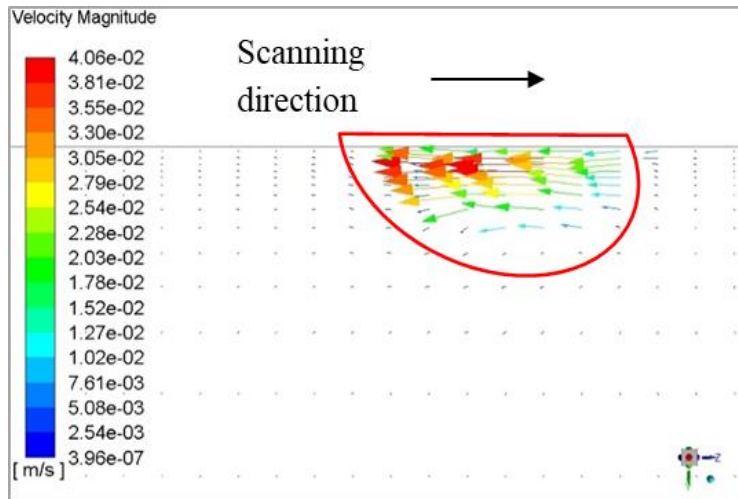


Figure 5.31: Contour plots for velocity (m/s) at the longitudinal section at  $y = 7.5 \text{ mm}$  in SLM and EBAM

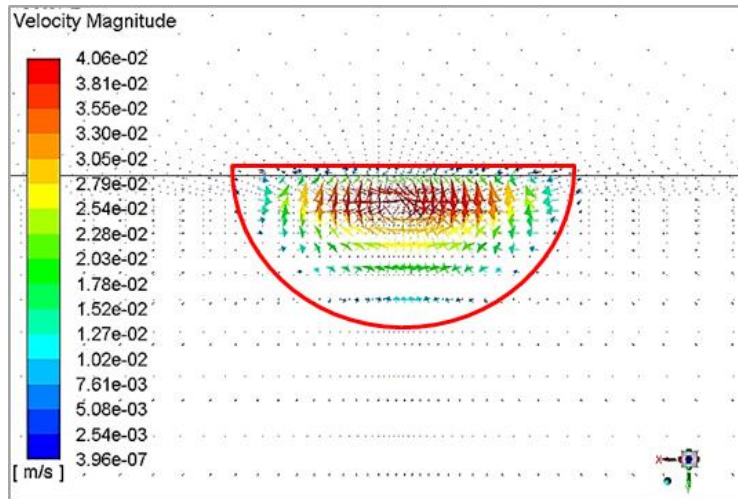
The maximum velocity for the SLM model is found in the middle of the melt-pool whereas the maximum melt-pool velocity in the EBAM model is detected towards the tail end from the center. The temperature gradient leads to a surface tension gradient, which causes a

Marangoni flow from low surface tension area to high surface tension area of the melt pool as described by Yuan and Gu [38]. The cooler liquid near the edge of the melt-pool having higher surface tension tends to pull the liquid away from the melt-pool center. However, the magnitudes of the maximum velocity in the melt pool for the SLM and the EBAM models are about 18.6 mm/s and 15.4 mm/s, respectively, which confirm that the values of the Reynolds number  $Re (= \rho u_i \Phi / \mu)$  are very low and the flow is laminar in both SLM and EBAM cases.

The fluid flow pattern inside the melt pool can be observed from the vector plots. The flow patterns for SLM and EBAM melt pools show similar nature although the velocity magnitudes are different. As a representative case, the fluid flow pattern observed in the SLM model at  $y = 7.5$  mm for 300 mm/s laser scanning speed with 200 W power and 58  $\mu\text{m}$  spot size is shown in Fig. 5.32. As it is shown, the melted material starts to move upwards from the melt-pool center, and it is directed towards its edges. The negative temperature coefficient of surface tension for Ti-6Al-4V means the surface tension value decreases by increasing the material temperature. The melt-pool center has a higher temperature than its surrounding area. This means that the net force applied on the material in the melt-pool center is toward the surrounding area which causes the material to flow outwards [57]. The flow is upwards in the center of the molten pool due to the combined effects of gravity and buoyancy forces. The circulation patterns in the longitudinal and cross-sectional planes are shown in Fig. 5.32. The convection effects and recoil pressure serve to generate a velocity vortex which tends to pull the liquid up and results in the characteristic melt-pool hump. The hump is not possible to show in the contour plots as the top surface of the domain is fixed (flat) and the external medium is not included in the domain.



(a)



(b)

Figure 5.32: Fluid flow patterns in the SLM model at (a) the longitudinal section, and (b) the cross-section for 300 mm/s scanning speed with 200 W power and 58  $\mu\text{m}$  spot size

## 5.2 Experimental Results

### 5.2.1 Effects of Changing Laser Scanning Speed

Setting the laser power of 200 W and the spot size of 58  $\mu\text{m}$ , four single laser scans are performed on the powder bed under pure argon environment with the scanning speeds of 100 mm/s, 300 mm/s, 750 mm/s, and 1000 mm/s, respectively, as shown in Fig. 5.33. The unprocessed powders are removed to observe the tracks on top of the substrate.

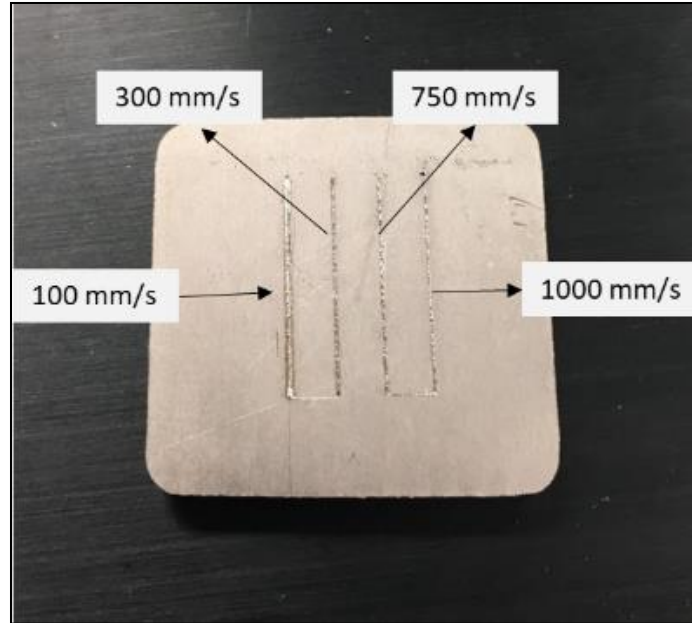


Figure 5.33: Ti-6Al-4V powder-bed specimen after laser scanning

Figure 5.34 shows the SEM images of the cross-sections of the single laser tracks on the Ti-6Al-4V powder-bed specimen at 200 W laser power and 58  $\mu\text{m}$  spot size. The images suggest that the higher the laser scanning speed, the smaller the melt-pool size. The slower laser scanning speed yields larger energy density input, leading to a deeper penetration depth. The melt-pool shape gradually changes from an inverted triangle to a semicircle as the laser scanning speed increases. The laser scanning tracks all bulge to some extent because of the effects of surface tension and variation of recoil pressure during the laser melting process. It is worth noting that the irregularities in the melting pool shape result due to the Marangoni force and recoil pressure in the melting pool during the melting and rapid consolidation in the gas environment.

### 5.2.2 Effects of Changing Laser Power

Setting the laser scanning speed at 100 mm/s and the spot size at 58  $\mu\text{m}$ , several single laser scans are performed on the powder bed specimen (with 58.76 % porosity level) under a pure argon environment. The SEM images of the cross-sectional microstructures are examined to

observe the melt-pool geometries and the heat-affected zones. Figure 5.35 shows the SEM images for the cases of 200 W, 150 W, and 100 W laser powers, respectively. As laser power decreases, the melt-pool volume decreases.

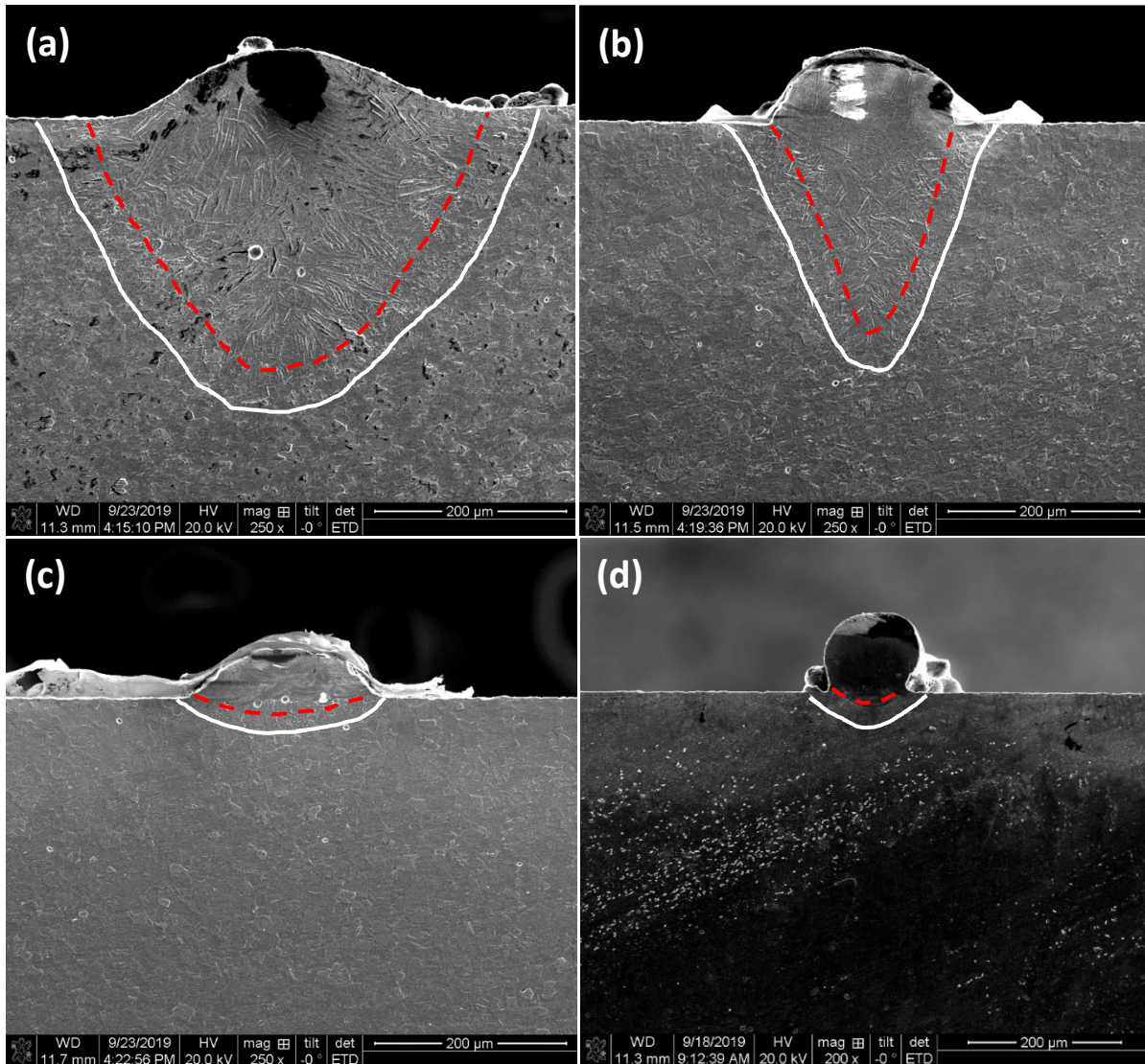


Figure 5.34: SEM images showing the melt-pool features of single tracks treated with varying laser scanning speeds – (a) 100 mm/s, (b) 300 mm/s, (c) 750 mm/s, and (d) 1000 mm/s. The white lines indicate the boundary between heat-affected zone and the substrate, while the red dashed line demonstrates the boundary of melt zone and heat-affected zone

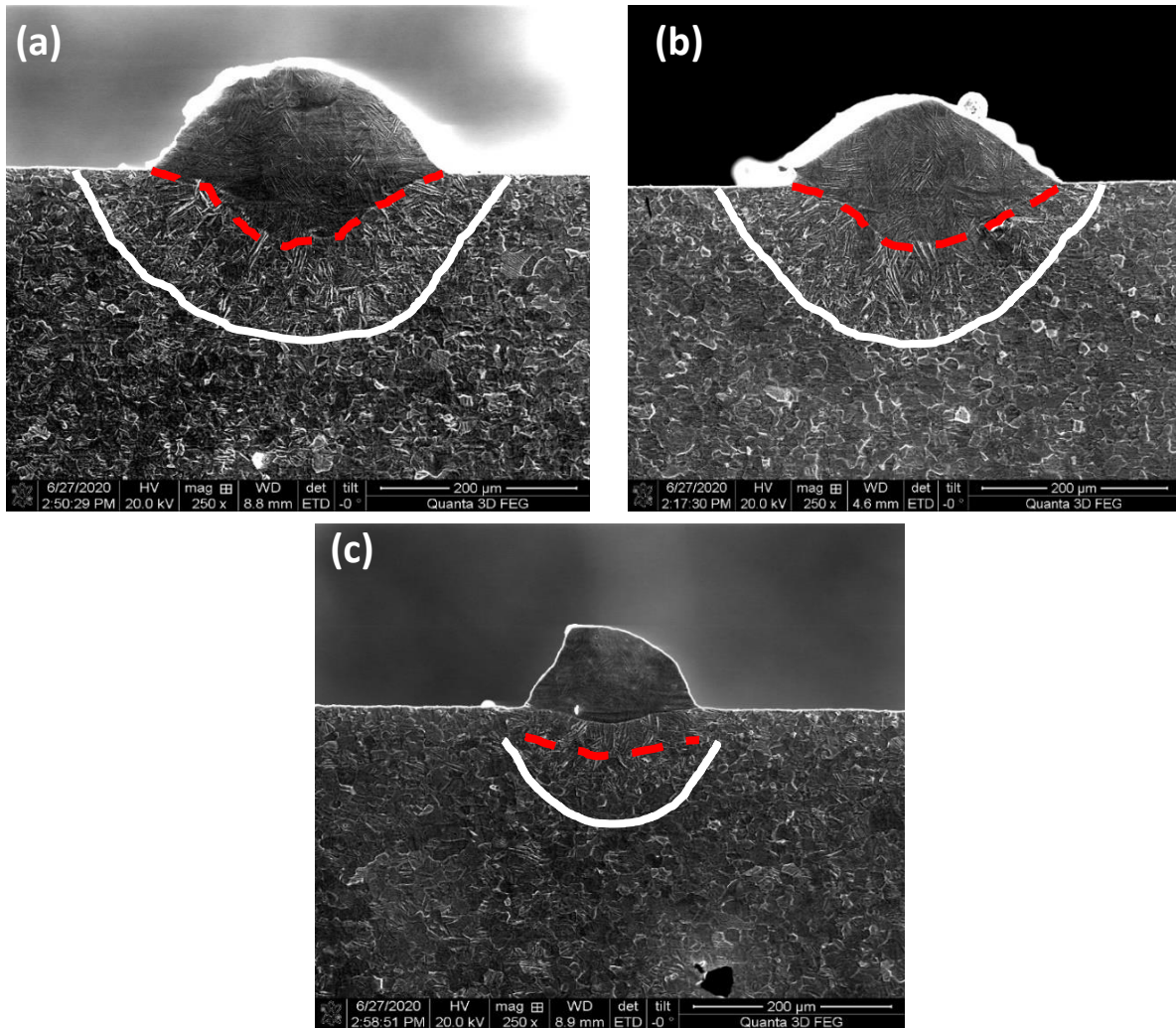


Figure 5.35: SEM images showing the melt-pool features of single tracks treated with varying laser powers – (a) 200 W, (b) 150 W, and (c) 100 W. The white line indicates the boundary between heat-affected zone and the substrate, while the red dashed line demonstrates the boundary of melt zone and heat-affected zone

### 5.2.3 Effects of Changing Laser Spot Size

Setting the laser power at 200 W and the scanning speed at 100 mm/s, several single laser scans are performed on the powder bed under pure argon environment. The SEM images of the cross-sectional microstructures are examined following the similar approach as sated above. Figure 5.36 shows the SEM images for the cases of 400  $\mu\text{m}$ , 300  $\mu\text{m}$ , and 200  $\mu\text{m}$  laser spot

sizes, respectively. As the laser spot size decreases, the melt-pool volume increases because of the increase in incident laser energy density.

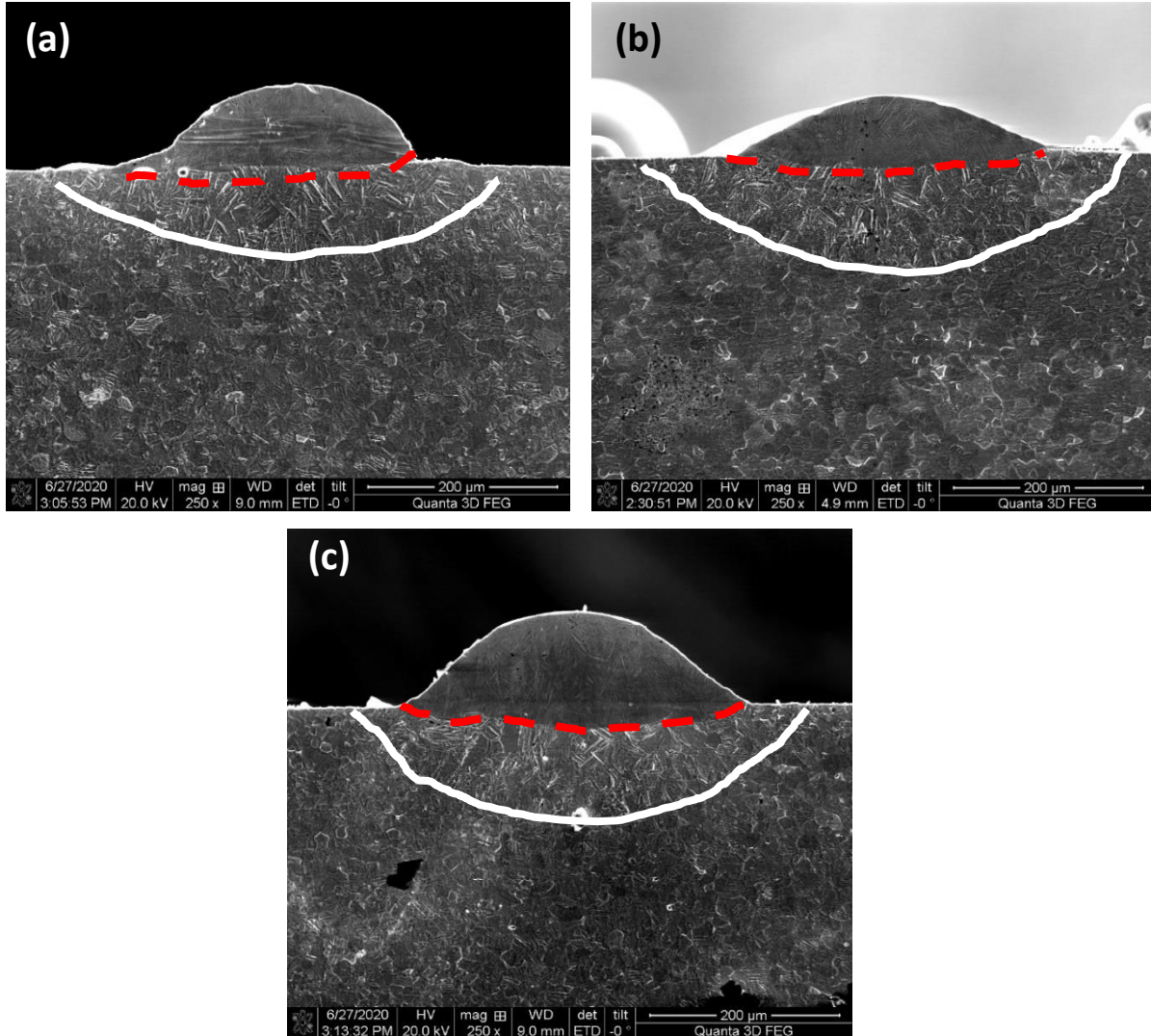


Figure 5.36: SEM images showing the melt-pool features of single tracks treated with varying laser spot sizes – (a) 400 μm, (b) 300 μm, and (c) 200 μm. The white line indicates the boundary between heat-affected zone and substrate, while the red dashed line demonstrates the boundary of melt zone and heat-affected zone

## Chapter 6

### Model Validation

#### 6.1 Validation with the Classical Stefan Problem of Melting

The results obtained from the Fluent simulation for melting of pure titanium (Ti) is compared with the analytical solution of the classical Stefan problem [63, 96] of melting of a phase change material (PCM) with pure conduction. Figure 6.1 shows the standard geometry for the Stefan problem where the PCM is semi-infinite and initially (at  $t = 0$ ) solid at its melting temperature  $T_m$  [63, 96]. The wall temperature  $T_w$  is raised to  $T_w > T_m$  for melting the PCM in a linear fashion starting at  $x = 0$ . The melting front moves forward in the  $x$ -direction as time increases.

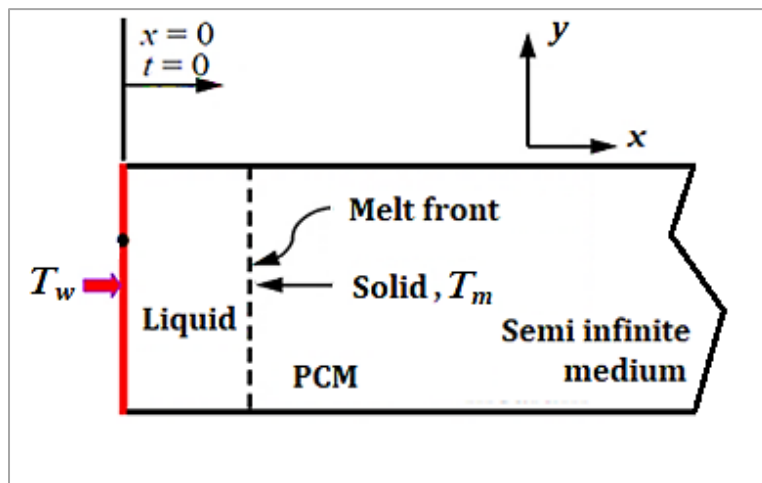


Figure 6.1: Schematic of the 1-D Stefan problem of solid-liquid phase change [63, 96]

According to the Stefan condition, the solution for the transient temperature distribution in the liquid is given by Eq. (23) [63, 96].

$$\frac{T_l(x, t) - T_w}{T_m - T_w} = \frac{\text{erf}(x/2\sqrt{\alpha_l t})}{\text{erf}(\lambda)} \quad (23)$$

where,  $\alpha_l = k_l/\rho_l c_{p,l}$  is the thermal diffusivity of the liquid PCM and  $\lambda$  is obtained from the interfacial melt-front equation [96] as follows

$$\lambda e^{\lambda^2} \text{erf}(\lambda) = \frac{Ste}{\sqrt{\pi}} \quad (24)$$

The Stefan number,  $Ste$  is defined as

$$Ste = \frac{c_{p,l}(T_w - T_m)}{L_f} \quad (25)$$

The position of the melting front, measured from  $x = 0$ , is given by

$$s(t) = 2\lambda \sqrt{\alpha_l t} \quad (26)$$

The validation of the Fluent result is conducted by predicting the motion of the liquid-solid interface during the melting of pure Ti. The parameters shown in Table 6.1 are used during the ANSYS Fluent simulation.

**Table 6.1: List of the simulation parameters for Ti melting [63]**

<b>Parameters</b>	<b>Values</b>
Density of liquid Ti, $\rho_l$ (kg/m <sup>3</sup> )	4500
Specific heat capacity of liquid Ti, $c_{p,l}$ (J/kg-K)	528
Effective viscosity, $\mu$ (kg/m-s)	4.3e-3
Thermal conductivity of liquid Ti, $k_l$ (W/m-K)	17
Latent heat of fusion, $L_f$ (kJ/kg)	435.4
Melting temperature, $T_m$ (K)	1923
Wall temperature, $T_w$ (K)	2073
Solidus temperature, $T_s$ (K)	1923
Liquidus temperature, $T_L$ (K)	1943

The simulation results of the change in interface position with respect to time during the melting of Ti show a good agreement with the analytical results. The liquid fraction contours obtained from the simulation at  $t = 0.37$  s and  $t = 1.8$  s are shown in Fig. 6.2.

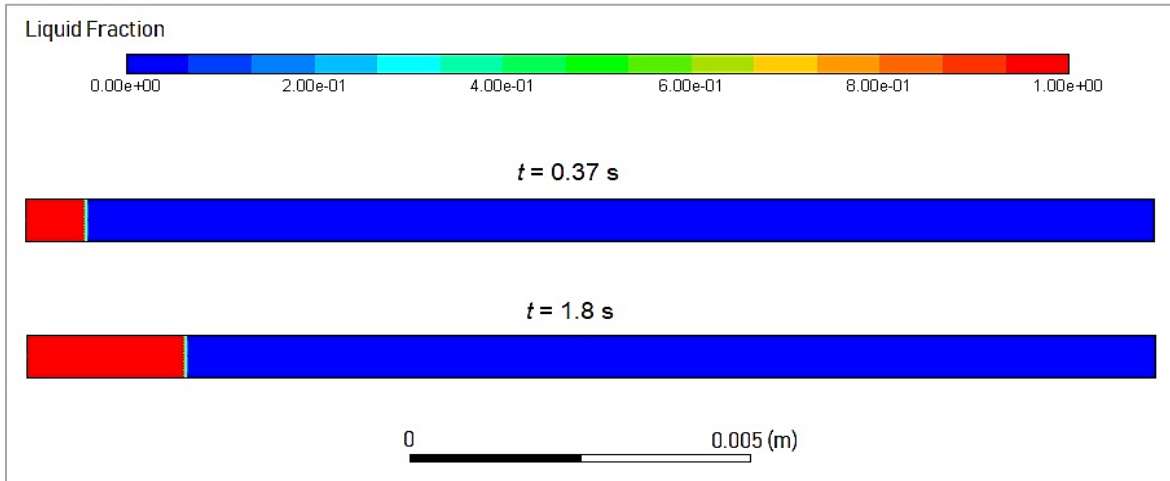


Figure 6.2: Contour plots for liquid fraction in melting of pure Ti at two different times

Figure 6.3 shows the comparison between the analytical and simulation results for the melt front position with respect to time at  $x = 1$  mm.

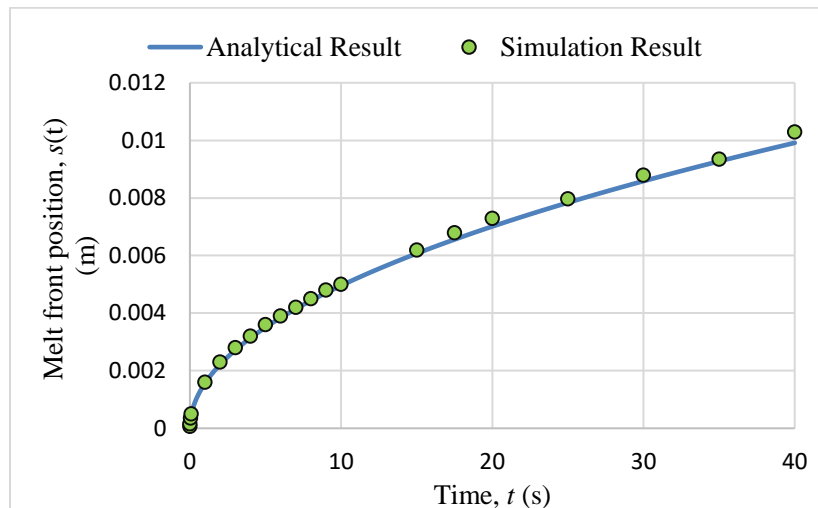


Figure 6.3: Change in melt front position with respect to time for melting of pure Ti

Results for temperature distribution also show a good match between the analytical and simulation results. At  $x = 1$  mm, the comparison between the analytical and simulation results for centerline temperature at three different times is shown in Table 6.2.

**Table 6.2: Comparison between analytical and numerical results for temperature**

Time (s)	Temperature (K)		
	Analytical	Numerical	Deviation (%)
0.5	1936.97	1940.50	0.182
1.0	1975.70	1979.45	0.189
10	2041.91	2048.07	0.300

## 6.2 Experimental Validation for the SLM Model

The SLM modeling results for melt-pool geometry are compared with the SLM experimental results. A piece of polished solid Ti-6Al-4V disk, having dimensions of 12.7 mm diameter and 2 mm thickness, is used as the target material in the custom YLR laser system. Setting a laser power of 200 W and considering a spot size of  $58 \mu\text{m}$ , four single laser scans are performed on the disk under argon environment with scanning speeds of 100 mm/s, 300 mm/s, 750 mm/s, and 1000 mm/s, respectively, as shown in Fig. 6.4.

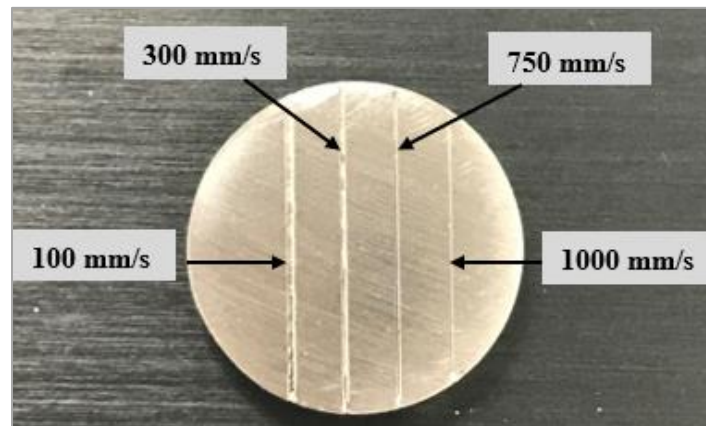


Figure 6.4: Solid Ti-6Al-4V disk specimen after laser scanning

After laser scanning, the Ti-6Al-4V disk is cut using low speed saw, grinded successively with SiC papers, polished with the MetaDi™ Supreme polycrystalline diamond suspension (1  $\mu\text{m}$ ), rinsed ultrasonically in acetone, ethanol, and deionized water, and finally etched with the Kroll's reagent to reveal the cross-section of the laser scanning tracks. The microstructures of the cross-section areas are examined by a Quanta™ 3D Dual Beam™ FEG FIB-SEM scanning electron microscope (SEM) with an accelerating voltage of 20 kV. Figure 6.5 shows the SEM images of the cross-section where the melt-pool size decreased with the increase in the scanning speed.

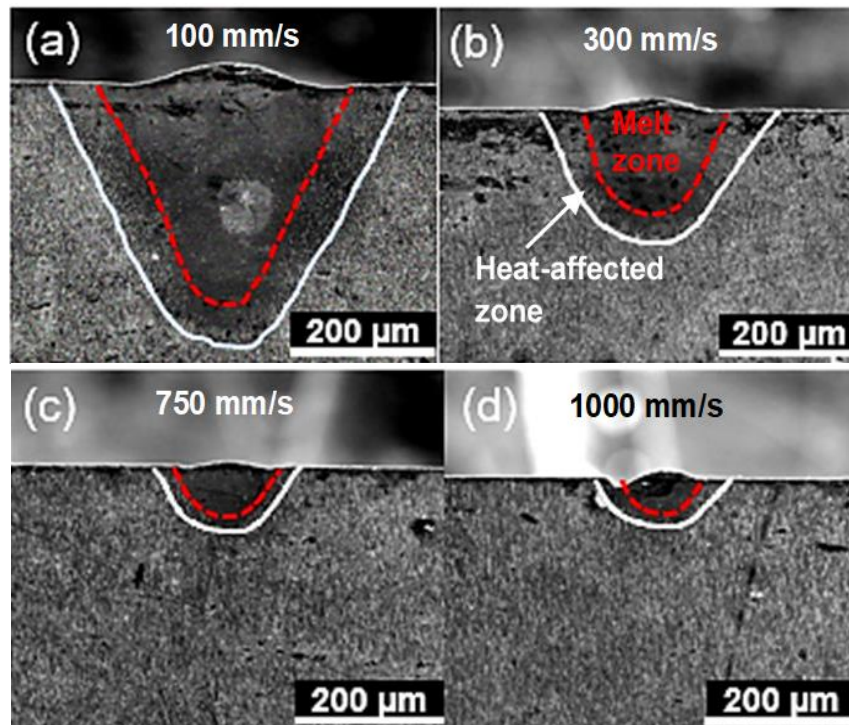


Figure 6.5: SEM images of the cross-sections of the single tracks on the solid Ti-6Al-4V specimen with different laser scanning speeds – (a) 100 mm/s, (b) 300 mm/s, (c) 750 mm/s, and (d) 1000 mm/s. The white lines indicate the boundary between heat-affected zone and the substrate, while the red dashed line shows the boundary of melt zone and the heat-affected zone

The laser scanning tracks all bulge to some extent, indicating the significant surface tension effect. The melt-pool shape for 1000 mm/s appeared inconsistent with the other shapes because of

the Marangoni force and recoil pressure [97–99] in the melt pool during the laser scanning and cooling at a fast rate.

For the demonstration purpose, the laser melting case of 100 mm/s scanning speed is chosen to represent the comparison between the experimental and the simulated results. This is the most extreme case in terms of energy density and forms the largest melt pool among the four conditions. The powder layer of the SLM model is converted to solid to run the simulations. A mesh convergence study is conducted for the structured mesh of the 3-D domain of the modified SLM model when the beam spot size is 58  $\mu\text{m}$ , scanning speed is 100 mm/s, and the effective power is 200 W. The temperature at location  $(x, y, z) = (0, 6 \text{ mm}, 0.02 \text{ mm})$  is monitored for several different mesh densities at  $t = 0.04 \text{ s}$ . The value of the maximum temperature inside the melt pool converges to 3279 K with the increase of the number of nodes in the domain. Figure 6.6 depicts the results for the mesh convergence study where the temperature at the fixed point remains unchanged after 201,089 nodes corresponding to 190,512 hexahedral cells. Results for the melt-pool geometry are obtained for the converged mesh.

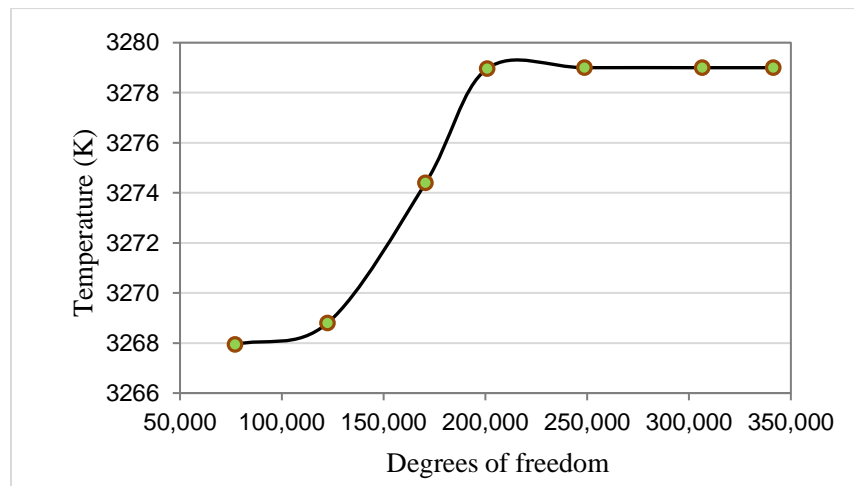


Figure 6.6: Mesh convergence plot for the modified SLM model considering the variation of melt-pool temperature with the increase of degrees of freedom at  $y = 6 \text{ mm}$ , and  $t = 0.04 \text{ s}$

The contour plots for temperature and liquid fraction from the CFD simulation are compared with the selective laser melted solid specimen's microstructure. Figure 6.7 depicts the comparison between the experimental and numerical results for  $492.61 \text{ J/mm}^3$  energy density and a laser interaction time of  $580 \mu\text{s}$ . These are calculated for a scanning speed of  $100 \text{ mm/s}$  with a beam power of  $200 \text{ W}$  and a spot size of  $58 \mu\text{m}$ . The bulge in the top surface in the SEM image is caused because of the surface tension and recoil pressure in the melt zone. Since the modeling domain is fixed with a continuum material, the top surface remains flat in the numerical model. However, the total area of the melt zone in the SEM image resembles the area of the liquid fraction contour obtained from the numerical simulation which gives a good prediction about the volume of the melt pool.

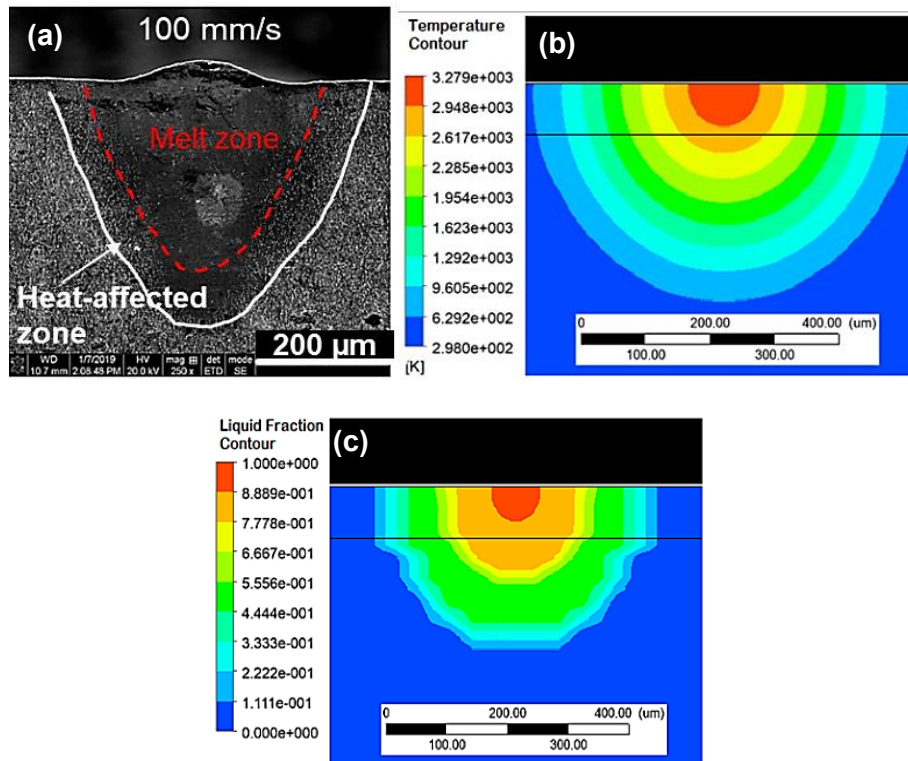


Figure 6.7: Comparison of the experimental results for  $100 \text{ mm/s}$  scanning speed with the modeling results at  $y = 6 \text{ mm}$ , and  $t = 0.04 \text{ s}$ , showing (a) the SEM image of the microstructure, (b) the temperature contour, and (c) the liquid fraction contour

Simulation results for the maximum melt-pool width and depth obtained at  $y = 6$  mm and  $t = 0.04$  s show a good agreement with the experimental results for the case of  $492.61 \text{ J/mm}^3$  energy density and a laser interaction time of  $580 \mu\text{s}$  (with  $100 \text{ mm/s}$  scanning speed). The change in microstructure in the cross-section of the test specimen is examined by the SEM to measure the maximum width and depth of the melt pool. Table 6.3 represents the comparative study for the maximum melt-pool width and depth, where 3.33 % deviation is found for width and 10.15 % deviation is recorded for the depth of the melt pool [65].

**Table 6.3: Melt-pool width and depth at 100 mm/s scanning speed [65]**

<b>Parameters at 200 W and 100 mm/s</b>	<b>Experimental result</b>	<b>Simulation result</b>	<b>Deviation %</b>
Width ( $\mu\text{m}$ )	377	390	3.33
Depth ( $\mu\text{m}$ )	345	310	10.15

### **6.3 Experimental Validation for the EBAM Model**

The numerical results for melt-pool geometry of the EBAM model are validated by comparing with experimental results. The experimental procedure for EBAM conducted by Jamshidinia *et al.* [58] with Ti-6Al-4V is followed to validate the proposed multiphysics model. Jamshidinia *et al.* [58] compared the results for the variation of average melt pool width and depth with the change in scanning speed. Using a constant electron beam diameter of  $0.4 \text{ mm}$ , beam current of  $14 \text{ mA}$ , and voltage of  $60 \text{ kV}$ , they applied three levels of scanning speed namely,  $100 \text{ mm/s}$ ,  $300 \text{ mm/s}$ , and  $500 \text{ mm/s}$  to measure the average melt-pool width and depth. They found that the differences between their modeling results and experimental results ranged from  $-3.5 \%$  to  $+3 \%$  for the melt-pool width, and from  $+2.1 \%$  to  $+3.5 \%$  for the melt-pool depth. Following a similar approach, the simulation results for melt-pool geometry obtained from

the proposed multiphysics model with the converged mesh having 190,040 hexahedral cells with 200,889 nodes provide a good agreement with the experimental results presented by Jamshidinia *et al.* [58]. The comparison gives a maximum deviation of 3.73 %, which indicates a good accuracy to predict the thermal properties using the model. The validation of the proposed multiphysics EBAM model is illustrated in Fig. 6.8.

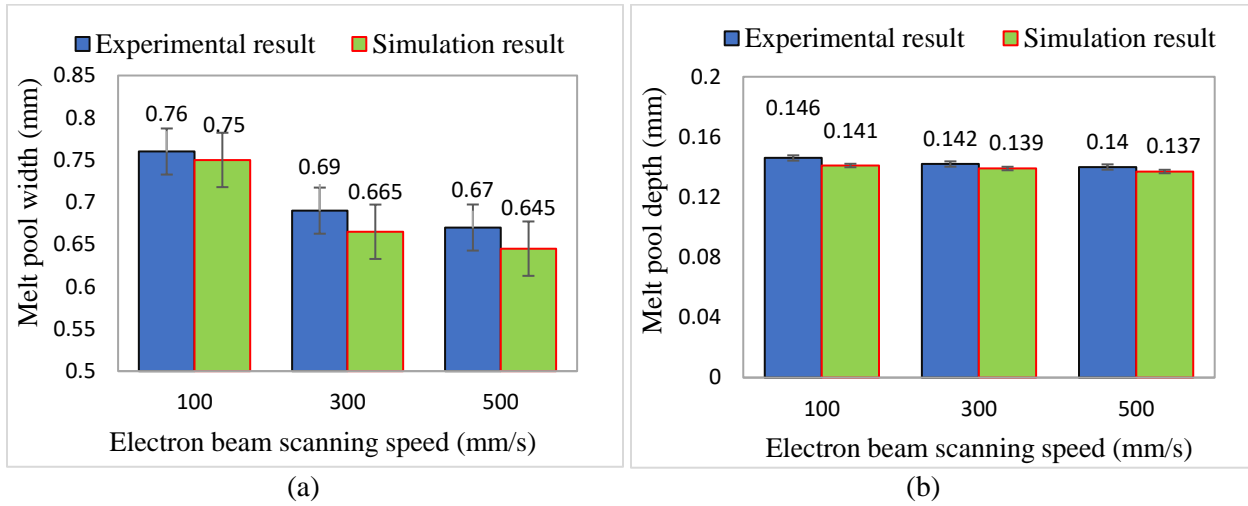


Figure 6.8: EBAM model validation by comparing the numerical results for (a) melt-pool width versus scanning speed, and (b) melt-pool depth versus scanning speed with the EBAM experimental results [58, 63]

#### 6.4 Validation with a Lid Driven Cavity Problem

As a benchmark case for studying the numerical methods to solve the Navier-Stokes equations, driven cavity flow is used extensively by many researchers [100–103]. In most cases, the problem is dealt with considering a cavity with a stationary side and bottom walls where the top surface (lid) is moved at a uniform velocity. Assuming incompressible flow inside the cavity, numerous investigations have been done [100–103] with low Mach numbers and variable Reynolds numbers to solve the problem. This study of incompressible flow has been the benchmark for years with widespread applications for researchers including the study of channel flows, cavity flows, and low and high Mach number laminar compressible flows.

A 2-D square cavity having dimensions of 25.4 mm  $\times$  25.4 mm is considered to investigate the development of circulation pattern for the compressible flow of ideal gas inside it due to the motion of the lid. The simulations are carried out in the CFD solver of ANSYS Fluent. Figure 6.9 shows the physical domain and comparison between the benchmark [100] and Fluent results for the velocity streamline inside the cavity for a lid velocity of 0.23 m/s (i.e., Re = 400).

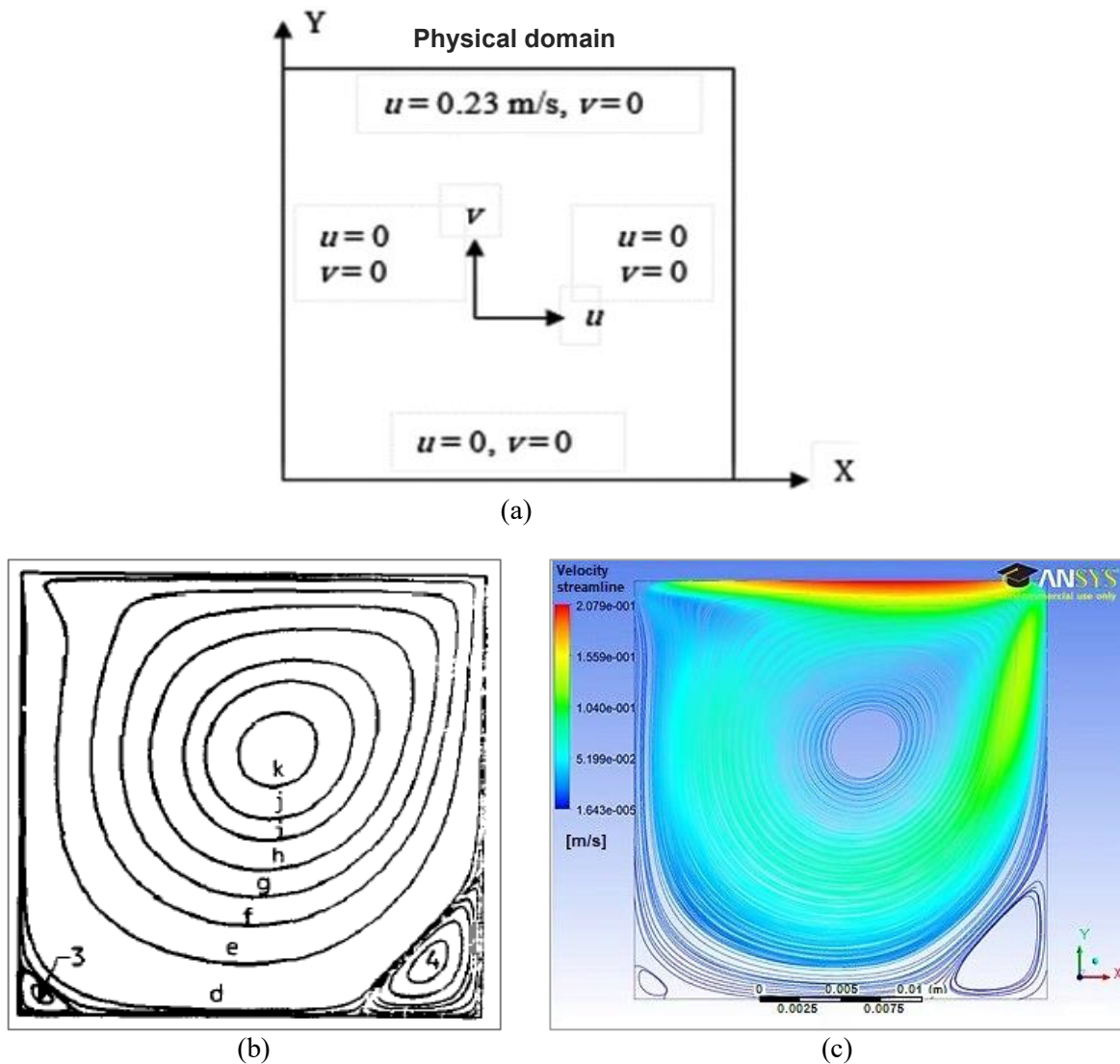


Figure 6.9: (a) Physical domain of the square cavity, (b) velocity streamline for the benchmark case at Re = 400, and (c) velocity streamline obtained from Fluent simulation at Re = 400

The side walls and the bottom wall of the cavity are assumed to be stationary and the top surface (lid) is moved with a uniform translational velocity in horizontal direction. The cavity is filled with compressible ideal gas having a Prandtl number of 1 and Mach number of 0.05. Numerical experiments are carried out to simulate the development of shear driven circulation patterns inside the cavity for various Reynolds numbers ( $Re = 400$  to  $3200$ ). The results for velocity distribution and vorticity are obtained for both steady and unsteady conditions. The results indicate that a primary circulation is formed at the center of the cavity with secondary circulation patterns developing at the bottom corner of the cavity.

The Fluent results for  $u$  and  $v$  velocities along the normalized vertical length and the normalized horizontal length, respectively, for  $Re = 1000$  and a lid velocity of  $0.575$  m/s show very good agreement with the benchmark results established by Ghia *et al.* [100]. Figure 6.10 shows the comparison between the Fluent results and benchmark results for the normalized  $u$  and  $v$  velocities inside the cavity [104].

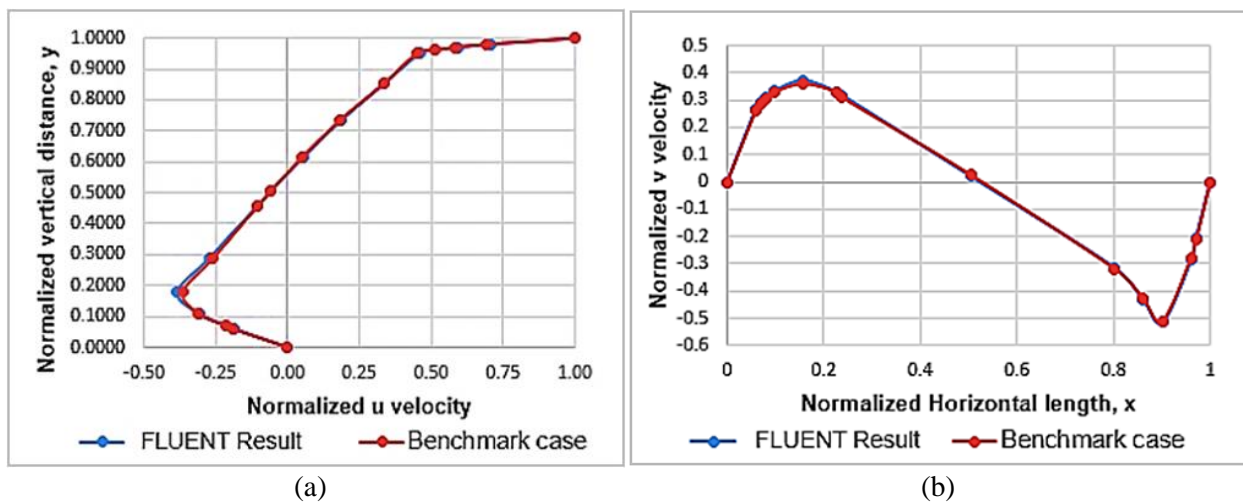


Figure 6.10: Comparison of Fluent results with the benchmark case for (a) normalized  $u$ , and (b) normalized  $v$  velocities

## Chapter 7

### Conclusions

#### 7.1 Concluding Remarks

A transient three-dimensional (3-D) computational fluid dynamics (CFD) model with Ti-6Al-4V powder-bed is developed and validated experimentally and analytically to investigate the thermo-fluid properties of a Ti-6Al-4V in the powder-bed fusion (PBF) process. The comparison between the selective laser melting (SLM) and electron beam additive manufacturing (EBAM) processes is outlined by studying the laser-material and electron beam-material interactions under similar irradiation conditions. The information obtained from the modeling results provides a guide to control the process parameters for obtaining desired properties of the build part with a detailed understanding of the thermal history and melt-pool dynamics. Numerical simulation of the thermal behavior and melt-pool evolution as a result of the interaction between the moving heat source and powder zone is the foundation for obtaining feedback of laser or electron beam processing parameters in the PBF process. The residual stress analyses of the build part and shape optimization of the melt zone also depend on the thermal history and melt-pool evolution along the melt scan. Therefore, the objective of the study is to characterize the process parameters of both SLM and EBAM and compare the melt-pool geometries, temperature distributions, and thermal properties along the melt scan under the same irradiation condition. Both the laser and electron beams are designed as a Gaussian moving heat source. The heat source specifications and temperature-dependent parameters are assigned as user-defined functions in the CFD modeling. The 3-D geometry of the melt pool is identified, and the correlation between the size of the melt pool with various beam specifications is outlined. The following conclusions can be drawn based on the comparative study.

- From the simulations, it is found that the liquid domain cools down in 0.008 s for EBAM. On the other hand, the melt pool cools down in 0.0045 s in the SLM process, which is faster than EBAM. The additional heat transfer due to convection on the top surface in SLM makes the cooling process faster, although radiation is present in both cases. The same maximum temperature of 2578 K is obtained by considering an irradiance level of  $26 \text{ J/mm}^3$  and an interaction time of 1.212 ms for both the SLM and EBAM models.
- At the same scanning speed and beam spot size, the depth of the melt pool in EBAM is higher than that in SLM. The lack of penetration of laser causes shallow melt-pool depth in SLM. Although the length and depth are significantly different, the width of the melt pool is almost the same in both SLM and EBAM for similar operating conditions.
- The melt-pool volume is larger in EBAM than that in SLM. The preheating and the vacuum help obtain a larger volume of melt pool in EBAM than that in SLM. At a given scanning speed, the melt-pool volume increases as the power of the heat source increases. If the scanning speed increases at constant power, the melt-pool volume decreases.
- Due to the consistency of the comparison, a fixed powder porosity level of 50% is considered. However, if the powder porosity is increased, the maximum temperature in the melt pool becomes higher due to the lower density of powder. This eventually makes the cooling rate slower than in the current cases.
- Due to greater convection, the melt-pool velocity in SLM is higher than that in EBAM. The Marangoni convection affects the mass and heat transfer within the melt-pool and eventually, the melt-pool geometry. The wide and shallow shape of the melt pool is due to the presence of the Marangoni effect. The fluid flow is laminar in both cases and values of the Reynolds number and Mach number are very low.

- A customized ytterbium fiber laser system is applied to perform the laser melting experiments. Microstructures of the melt zone and heat-affected zone are studied with scanning electron microscope (SEM) images and the melt-pool geometry is compared with the numerical results to validate the CFD model. The numerical results for melt-pool geometry show a good agreement with the experimental results.
- A comparative study, differentiating the effects of the laser and electron beams under similar irradiation conditions, provides a thorough understanding of the physics involved in the two processes. The study facilitates the design for correct experiments prior to the actual production by giving room to optimize the process parameters and control the energy transfers in the SLM and EBAM processes.

The thermo-fluid model presented in this study characterizes the thermal behavior and dynamics of the melt-pool in the SLM and EBAM processes and can incorporate various materials and operating conditions for further analyses of the powder-bed fusion process. The numerical simulation and experimental analysis of temperature history and melt-pool dynamics provide useful guidance for choosing the appropriate processing parameters to establish a feasible operating condition during the PBF process. A comprehensive study on the comparison between SLM and EBAM processes can establish a standard to choose the appropriate technique in the fusion-based additive manufacturing industry.

## **7.2 Proposed Future Work**

Several modifications can be done in the thermal modeling of the 3-D configuration in order to extend the scope of the study. The possible modifications and future works are provided below.

1. 3-D simulations can be carried out with various powder-porosity levels (i.e., various packing densities) to investigate the effect of changing porosity on the heat transfer phenomena and melt-pool dynamics. Besides, multiple scans can be considered to see the effect of the hatching spaces on the melt pool.
2. Instead of Ti alloy, the model can be applied for other metals and alloys (e.g., Cu alloys) suitable for the PBF process. The user-defined function (UDF) needs to be updated based on the material to be selected.
3. A volume-of-fluid (VOF) model can be developed keeping a vacuum or a convective medium at the top of the domain to investigate the surface formation and roughness properties of the PBF process.
4. A numerical code using finite element or finite volume method can be developed based on the governing equations of the process to study the temperature-dependent properties. Results generated from the commercially available software can be compared with the in-house numerical code for checking the accuracy.
5. Electron beam melting experiments can be conducted using Ti-6Al-4V specimens or other materials of interest for the experimental validation of the results obtained from the EBAM model.
6. A machine learning approach based on the regression analysis (both linear and logistic) can be developed with the experimental data to optimize the processing parameters and find out the dominant factors affecting the thermal history and melt-pool evolution in the PBF process.

## References

- [1] Vaezi, M., Seitz, H., and Yang, S., 2013, “A review on 3D micro-additive manufacturing technologies,” *Int. J. Adv. Manuf. Technol.*, **67**, pp. 1721–1754.
- [2] Goodridge, R., and Ziegelmeier, S., 2017, “7 - Powder Bed Fusion of Polymers,” in *Laser Additive Manufacturing*, Woodhead Publishing, Duxford, UK, 2017, pp. 181–204.
- [3] <https://wohlersassociates.com/blog/2013/05/wohlers-report-2013/>
- [4] <https://www.grandviewresearch.com/press-release/global-3d-metal-printing-market>
- [5] Cook, P. S., and Murphy, A. B., 2020, “Simulation of melt pool behaviour during additive manufacturing: Underlying physics and progress,” *Addit. Manuf.*, **31**, 100909, pp. 1–23.
- [6] Everton, S. K., Hirsch, M., Stravroulakis, P., Leach, R. K., and Clare, A. T., 2016, “Review of in-situ process monitoring and in-situ metrology for metal additive manufacturing,” *Mater. Des.*, **95**, pp. 431–445.
- [7] Fotovvati, B., Wayne, S. F., Lewis, G., and Asadi, E., 2018, “A Review on Melt-Pool Characteristics in Laser Welding of Metals,” *Adv. Mater. Sci. Eng.*, **2018**, 4920718, pp.1–18.
- [8] DebRoy, T., Wei, H. L., Zuback, J. S., Mukherjee, T., Elmer, J. W., Milewski, J. O., Beese, A. M., Wilson-Heid, A., De, A., and Zhang, W., 2018, “Additive manufacturing of metallic components - Process, structure and properties,” *Prog. Mater. Sci.*, **92**, pp. 112–224.
- [9] Sames, W. J., List, F. A., Pannala, S., Dehoff, R. R., and Babu, S. S., 2016, “The metallurgy and processing science of metal additive manufacturing” *Int. Mater. Rev.*, **6608**, pp. 315–360.
- [10] Bikas, H., Stavropoulos, P., and Chryssolouris, G., 2015, “Additive manufacturing methods and modelling approaches: a critical review,” *Int. J. Adv. Manuf. Technol.*, **83**(1), pp. 389–405.
- [11] Sing, S. L., An, J., Yeong, W. Y., and Wiria, F. E., 2015, “Laser and electron-beam powder-bed additive manufacturing of metallic implants: A review on processes, materials and designs,” *J. Orthop. Res.*, **34**, pp. 369–385.
- [12] Zhao, X., Li, S., Zhang, M., Liu, Y., Sercombe, T. B., and Wang, S., 2016, “Comparison of the microstructures and mechanical properties of Ti–6Al–4V fabricated by selective laser melting and electron beam melting,” *Mater. Des.*, **95**, pp. 21–31.

- [13] Gong, H., Rafi, K., Gu, H., Janaki Ram, G.D., Starr, T., and Stucker, B., 2015, "Influence of defects on mechanical properties of Ti-6Al-4 V components produced by selective laser melting and electron beam melting," *Mater. Des.*, **86**, pp. 545–554.
- [14] Rafi, K., Karthik, N. V., Gong, H., Starr, T., and Stucker, B., 2013, "Microstructures and mechanical properties of Ti-6Al-4 V parts made by selective laser melting and electron beam melting," *J. Mater. Eng. Perform.*, **22**, pp. 3872–3883.
- [15] Chastand, V., Quaegebeur, P., Maia, W., and Charkaluk, E., 2018, "Comparative study of fatigue properties of Ti-6Al-4V specimens built by electron beam melting (EBM) and laser PBF (L-PBF)," *Mater. Charact.*, **143**, pp. 76–81.
- [16] Wysocki, B., Maj, P., Sitek, R., Buhagiar, J., Kurzydłowski, K.J., and Świąszkowski, W., 2017, "Laser and Electron Beam Additive Manufacturing Methods of Fabricating Titanium Bone Implants," *Appl. Sci.*, **7**(7): 657, pp. 1–20.
- [17] Gokuldoss, P. K., Kolla, S., and Eckert, J., 2017, "Additive Manufacturing Processes: Selective Laser Melting, Electron Beam Melting and Binder Jetting-Selection Guidelines," *Materials (Basel, Switzerland)*, **10**(6):672, pp. 1–12.
- [18] Rahman, M. S., Schilling, P. J., Herrington, P. D., and Chakravarty, U. K., 2018, "A Comparative Study Between Selective Laser Melting and Electron Beam Additive Manufacturing Based on Thermal Modeling," *Proc. ASME International Mechanical Engineering Congress and Exposition, Vol. 1, Advances in Aerospace Technology, Pittsburgh, PA, Nov 9–15, 2018, IMECE2018-86428*, pp. 1–13.
- [19] Roehling, T. T., Wu, S. S. Q., Khairallah, S. A., Roehling, J. D., Soezeri, S. S., Crumb, M. F., and Matthews, M. J., 2017, "Modulating laser intensity profile ellipticity for microstructural control during metal additive manufacturing," *Acta Mater.*, **128**, pp. 197–206.
- [20] Qi, H., Mazumder, J., and Ki, H., 2006, "Numerical Simulation of Heat Transfer and Fluid Flow in Coaxial Laser Cladding Process for Direct Metal Deposition," *J. Appl. Phys.*, **100**(2), 024903, pp. 1–11.
- [21] Cho, W., Na, S., Thomy, C., and Vollertsen, F., 2012, "Numerical Simulation of Molten Pool Dynamics in High Power Disk Laser Welding," *J. Mater. Process. Technol.*, **212**(1), pp. 262–275.
- [22] Moraitis, G. A., and Labeas, G. N., 2008, "Residual stress and distortion calculation of laser beam welding for aluminum lap joints," *J. Mater. Process. Technol.*, **198**, pp. 260–269.

- [23] Wang, L., Felicelli, S., Gooroochurn, Y., Wang, P. T., and Horstemeyer, M. F., 2008, "Optimization of the LENS<sup>®</sup> process for steady molten pool size," *Mater. Sci. Eng., A*, **474**(1–2), pp. 148–156.
- [24] Lankalapalli, K., Tu, J. F., and Gartner, M., 1996, "A model for estimating penetration depth of laser welding processes," *J. Phys. D: Appl. Phys.*, **29**, pp. 1831–1841.
- [25] Roberts, I. A., Wang, C. J., Esterlein, R., Stanford, M., and Mynors, D. J., 2009, "A Three-Dimensional Finite Element Analysis of the Temperature Field During Laser Melting of Metal Powders in Additive Layer Manufacturing," *Int. J. Mach. Tools Manuf.*, **49**(12–13), pp. 916–923.
- [26] Yang, J., Sun, S., Brandt, M., and Yan, W., 2010, "Experimental Investigation and 3D Finite Element Prediction of the Heat Affected Zone During Laser Assisted Machining of Ti–6Al–4V Alloy," *J. Mater. Process. Technol.*, **210**(15), pp. 2215–2222.
- [27] Andreotta, R., Ladani, L., and Brindley, W., 2017, "Finite element simulation of laser additive melting and solidification of Inconel 718 with experimentally tested thermal properties," *Finite Elem. Anal. Des.*, **135**, pp. 36–43.
- [28] Sadowski, M., Ladani, L., Brindley, W., and Romano, J., 2017, "Optimizing quality of additively manufactured Inconel 718 using powder bed laser melting process," *Addit. Manuf.*, **11**, pp. 60–70.
- [29] Ladani, L., Romano, J., Brindley, W., and Burlatsky, S., 2017, "Effective Liquid Conductivity for Improved Simulation of Thermal Transport in Laser Beam Melting Powder Bed Technology," *Addit. Manuf.*, **14**, pp. 13–23.
- [30] Ladani, L., and Ahsan, F., 2019, "Laser Interaction with Surface in Powder Bed Melting Process and Its Impact on Temperature Profile, Bead and Melt Pool Geometry," *The Minerals, Metals & Materials Series* (eds), TMS 2019 148<sup>th</sup> Annual Meeting & Exhibition Supplemental Proceedings, The Minerals, Metals & Materials Series, Springer, Cham, pp. 319–329.
- [31] Ahsan, F., and Ladani, L., 2020, "Temperature Profile, Bead Geometry, and Elemental Evaporation in Laser Powder Bed Fusion Additive Manufacturing Process," *JOM*, **72**(1), pp. 429–439.
- [32] Riedlbauer, D., Scharowsky, T., Singer, R. F., Steinmann, P., Körner, C., and Mergheim, J., 2017, "Macroscopic simulation and experimental measurement of melt pool characteristics in selective electron beam melting of Ti-6Al-4V," *Int. J. Adv. Manuf. Technol.*, **88**, pp. 1309–1317.
- [33] Wen, S., and Shin, Y. C., 2010, "Modeling of Transport Phenomena During the Coaxial Laser Direct Deposition Process," *J. Appl. Phys.*, **108**, 044908, pp. 1–9.

- [34] Wang, R., Lei, Y., and Shi, Y., 2011, “Numerical Simulation of Transient Temperature Field during Laser Keyhole Welding of 304 Stainless Steel Sheet,” *Opt. Laser Technol.*, **43**, pp. 870–873.
- [35] Rai, R., Elmer, J. W., Palmer, T. A., and Debroy, T., 2007, “Heat Transfer and Fluid Flow During Keyhole Mode Laser Welding of Tantalum, Ti–6Al–4V, 304L Stainless Steel and Vanadium,” *J. Phys. D: Appl. Phys.*, **40**(18), pp. 5753–5766.
- [36] Raplee, J., Plotkowski, A., Kirka M. M., Dinwiddie R., Okello, Dehoff R. R., and Babu, S. S., 2017, “Thermographic Microstructure Monitoring in Electron beam Additive Manufacturing,” *Sci. Rep.*, **7**, 43554, pp. 1–16.
- [37] Li, J. F., Li, L., and Stott, F. H., 2004, “A Three-Dimensional Numerical Model for a Convection-Diffusion Phase Change Process During Laser Melting of Ceramic Materials,” *Int. J. Heat Mass Tran.*, **47**(25), pp. 5523–5539.
- [38] Yuan, P., and Gu, D., 2015 “Molten pool behaviour and its physical mechanism during laser PBF of TiC/AlSi10Mg nanocomposites: simulation and experiments,” *J. Phys. D: Appl. Phys.* **48**, 035303, pp. 1–16.
- [39] Le, T., Lo, Y., and Lin, Z., 2020, “Numerical simulation and experimental validation of melting and solidification process in selective laser melting of IN718 alloy,” *Addit. Manuf.*, **36**, 101519 (In Press).
- [40] Roy, L., 2013, “Variation in mechanical behavior due to different build directions of ti6al4v fabricated by electron beam additive manufacturing technology,” Master’s thesis, University of Alabama, USA.
- [41] Liu, C., Wu, B., and Zhang, J., 2010, “Numerical Investigation of Residual Stress in Thick Titanium Alloy Plate Joined With Electron Beam Welding,” *Metall. Mater. Trans. B*, **41**(5), pp. 1129–1138.
- [42] Lacki, P., and Adamus, K., 2011, “Numerical Simulation of the Electron Beam Welding Process,” *Comput. Struct.*, **89**(11–12), pp. 977–985.
- [43] Shen, N., and Chou, K., 2012, “Thermal Modeling of Electron Beam Additive Manufacturing Process: Powder Sintering Effects,” *Proc. ASME Manufacturing Science and Engineering Conference*, June 4–8, 2012, Notre Dame, IN, MSEC2012-7253, pp. 287–295.
- [44] Gong, X., Anderson, T., and Chou, K., 2014, “Review on Powder-Based Electron Beam Additive Manufacturing Technology,” *Manuf. Rev.*, **1**, pp. 1–12.

- [45] Murr, L., Martinez, E., Gaytan, S. M., Ramirez, D. A., Machado, B. I., Shindo, P. W., Martinez, J. L., Medina, F., Wooten, J., Ciscel, D., Ackelid, U., and Wicker, R. B., 2011, "Microstructural architecture, microstructures, and mechanical properties for a nickel-base superalloy fabricated by electron beam melting," *Metallurg. Mater. Trans. A*, **42**(11), pp. 3491–3508.
- [46] Gong, X., Cheng, B., Price, S., and Chou, K., 2013, "Powder-bed Electron-beam-Melting Additive Manufacturing: Powder Characterization, Process Simulation and Metrology," ASME District F-ECTC 2013, Birmingham, Alabama, Vol. 12, November 2–3, 2013, pp. 59–66.
- [47] Galati, M., Di Mauro, O., and Iuliano, L., 2020, "Finite Element Simulation of Multilayer Electron Beam Melting for the Improvement of Build Quality," *Crystals*, **10**(6): 532, pp. 1–18.
- [48] Rouquette, S., Guo, J., and Le Masson, P., 2007, "Estimation of the Parameters of a Gaussian Heat Source by the Levenberg–Marquardt Method: Application to the Electron Beam Welding," *Int. J. Therm. Sci.*, **46**(2), pp. 128–138.
- [49] Attar, E., 2011, "Simulation of Selective Electron Beam Melting Processes," Ph.D. thesis, University of Erlangen-Nürnberg, Germany.
- [50] Biamino, S., Penna, A., Ackelid, U., Sabbadini, S., Tassa, O., Fino, P., Pavese, M., Gennaro, P., and Badini, C., 2010, "Electron beam melting of Ti-48Al-2Cr-2Nb alloy: Microstructure and mechanical properties investigation," *Intermetallics*, **19**(6), pp. 776–781.
- [51] Cheng, B., Price, S., Lydon, J., Cooper, K., and Chou, K., 2014, "On Process Temperature in Powder-Bed Electron Beam Additive Manufacturing: Model Development and Validation," *ASME J. Manuf. Sci. Eng.*, **136**, 061018, pp. 1–12.
- [52] Chen, Y. X., Wang, X. J., and Chen, S. B., 2014, "The effect of electron beam energy density on temperature field for electron beam melting," *Adv. Mater. Res.*, **900**, pp. 631–638.
- [53] Zäh, M. F., and Lutzmann, S., 2010, "Modelling and simulation of electron beam melting," *Product. Eng. Res. Develop.*, **4**(1), pp. 15–23.
- [54] Rai, R., Burgardt, P., Milewski, J., Lienert, T., and DebRoy, T., 2009, "Heat transfer and fluid flow during electron beam welding of 21Cr–6Ni–9Mn steel and Ti–6Al–4V alloy," *J. Phys. D: Appl. Phys.*, **42**(2), 02550, pp. 1–12.
- [55] Rai, R., Palmer, T. A., Elmer, J. W., Debroy, T., 2009, "Heat Transfer and Fluid Flow During Electron Beam Welding of 304L Stainless Steel Alloy", *Weld. J.*, **88**(3), pp. 54–61.
- [56] Chahine, G., 2011, "Application of Digital Engineering in the Development of a Bio-Adaptable Dental Implant," Ph.D. thesis, Southern Methodist University, Dallas, TX.

[57] Jamshidinia, M., Kong, F., and Kovacevic, R., 2012, “Temperature distribution and fluid flow modeling of electron beam melting® (EBM),” Proc. ASME 2012 International Mechanical Engineering Congress and Exposition, Vol. 7, Part D, Fluid and Heat Transfer, Houston, TX, Nov 9–15, 2012, IMECE2012-89440, pp. 3089–3102.

[58] Jamshidinia, M., Kong, F., and Kovacevic, R., 2013, “Numerical Modeling of Heat Distribution in the Electron Beam Melting of Ti–6Al–4V,” ASME J. Manuf. Sci. Eng., **135**(6), 061010, pp. 1–14.

[59] Jamshidinia, M., Kong, F., and Kovacevic, R., 2013, “The coupled CFD-FEM model of electron beam melting® (EBM),” Proc. ASME District F-ECTC 2013 (Birmingham, Alabama, USA), Vol. 12, pp. 163–71.

[60] Rahman, M. S., Schilling, P. J., Herrington, P. D., and Chakravarty, U. K., 2016, “Thermo-Fluid Characterizations of Ti-6Al-4V Melt Pool in Powder-Bed Electron Beam Additive Manufacturing,” Proc. ASME 2016 International Mechanical Engineering Congress and Exposition, Vol. 1, Advances in Aerospace Technology, Phoenix, AZ, Nov 11–17, 2016, IMECE2016-65854, pp. 1–9.

[61] Rahman, M. S., Schilling, P. J., Herrington, P. D., and Chakravarty, U. K., 2017, “Thermal Analysis of Electron beam PBF Using Ti-6Al-4V Powder-bed,” Proc. ASME 2017 International Mechanical Engineering Congress and Exposition, Vol. 1, Advances in Aerospace Technology, Tampa, FL, Nov 3–9, 2017, IMECE2017-71663, pp. 1–13.

[62] Rahman, M. S., Schilling, P. J., Herrington, P. D., and Chakravarty, U. K., 2019, “Thermofluid Properties of Ti-6Al-4V Melt Pool in Powder-Bed Electron beam Additive Manufacturing,” ASME J. Eng. Mater. Technol., **141**(4), 041006, pp. 1–12.

[63] Rahman, M. S., Schilling, P. J., Herrington, P. D., and Chakravarty, U. K., 2021, “A Comparison of the Thermo-Fluid Properties of Ti-6Al-4V Melt Pools Formed by Laser and Electron-Beam Powder-Bed Fusion Processes,” ASME J. Eng. Mater. Technol., **143**(2), 021003. (In Press).

[64] Rahman, M. S., Schilling, P. J., Herrington, P. D., and Chakravarty, U. K., 2019, “Thermal Behavior and Melt-Pool Dynamics of Cu-Cr-Zr Alloy in Powder-Bed Selective Laser Melting Process,” Proceedings of the ASME International Mechanical Engineering Congress and Exposition, Vol. 1, Advances in Aerospace Technology, Salt Lake City, UT, Nov 11–14, 2019, IMECE2019-11581, pp. 1–9.

[65] Rahman, M. S., Schilling, P. J., Herrington, P. D., and Chakravarty, U. K., 2020, “Heat Transfer and Melt-Pool Evolution During Powder-Bed Fusion of Ti-6Al-4V Parts Under Various Laser Irradiation Conditions,” Proc. ASME 2020 International Mechanical Engineering Congress and Exposition, Vol. 1, Advances in Aerospace Technology, Portland, OR, Nov 16–19, 2020, IMECE2020-23838, pp. 1–10.

- [66] Rahman, M. S., Zeng, C., Wen, H., Guo, S., Schilling, P. J., Herrington, P. D., and Chakravarty, U. K., 2019, “Thermal Behavior and Melt Pool Dynamics in Powder-bed Fusion-based Additive Manufacturing Process,” Proc. Louisiana EPSCoR RII CIMM 2019 Symposium, Baton Rouge, LA, Jun 03, 2019, pp. 121–124.
- [67] Rahman, M. S., Zeng, C., Wen, H., Guo, S., Schilling, P. J., Herrington, P. D., and Chakravarty, U. K., 2020, “An Investigation on the Melting and Solidification Behavior of Ti64 Powder in the Laser Powder-Bed Fusion Process,” Proceedings of the Louisiana EPSCoR RII CIMM 2020 Symposium, Baton Rouge, LA, July 20, 2020, pp. 9–12.
- [68] Rigo, O., and Engel, C., 2013, “Selective Laser Melting versus Electron Beam Melting,” <http://www.slideshare.net/carstenengel/selective-laser-melting-versus-electron-beam-melting>.
- [69] <https://www.metal-am.com/metal-additive-manufacturing-magazine-archive/metal-additive-manufacturing-vol-4-no-2-summer-2018/> Accessed on 04/30/2020.
- [70] Cambridge Vacuum Engineering. <http://www.camvaceng.com/electron-beam-welding>. (accessed on 21 April 2018)
- [71] Lavery, N. P., Brown, S. G. R., Sienz, J., and Belblidia, F., 2014, “A Review of Computational Modelling of Additive Layer Manufacturing – Multi-Scale and Multi-Physics,” International Conference of Sustainable Design and Manufacturing, Cardiff, Wales, April 28–30, 2014.
- [72] Sih, S. S., and Barlow, J. W., 2004, “The Prediction of the Emissivity and Thermal Conductivity of Powder Beds,” Part. Sci. Technol., **22**(3), pp. 291–304.
- [73] Lin, T. H., Watson, J. S., and Fisher, P. W., 1985, “Thermal Conductivity of Iron-Titanium Powders,” J. Chem. Eng. Data, **30**(4), pp. 369–372.
- [74] Kolossov, S., Boillat, E., Glardon, R., Fischer, P., and Locher, M., 2004, “3D FE Simulation for Temperature Evolution in the Selective Laser Sintering Process,” Int. J. Mach. Tools Manuf., **44**(2–3), pp. 117–123.
- [75] Li, J., Johnson, W., and Rhim, W., 2006, “Thermal expansion of liquid Ti–6Al–4V measured by electrostatic levitation,” Appl. Phys. Lett., **89**, 111913, pp. 1, 2.
- [76] Mills, K. C., 2002, “Recommended Values of Thermophysical Properties for Selected Commercial Alloys,” Woodhead Publishing, Cambridge, UK, pp. 211–216.
- [77] Dai, K., Li, X., and Shaw, L., 2004, “Thermal Analysis of Laser-Densified Dental Porcelain Bodies: Modeling and Experiments,” ASME J. Heat Transfer, **126**(5), pp. 818–825.

[78] Arce, A. N., 2012, “Thermal Modeling and Simulation of Electron Beam Melting for Rapid Prototyping on Ti6Al4V Alloys,” Ph.D. thesis, North Carolina State University, Raleigh, NC.

[79] Wen, H., Zeng, C., Etefagh, A. H., Gao, J., and Guo, S., 2019, “Laser surface treatment of Ti-10Mo alloy under Ar and N<sub>2</sub> environment for biomedical application,” *J. Laser Appl.*, **31**, 022012, pp. 1–9.

[80] Brown, M. S., and Arnold, C. B., 2010, “Fundamentals of laser-material interaction and application to multiscale surface modification, *Laser Precision Microfabrication*,” Springer Series in Materials Science, Vol. 135, Springer, Berlin, Germany, 2010, pp. 91–120.

[81] Carriere, P. R., and Yue, S., 2017, “Energy absorption during pulsed electron beam spot melting of 304 stainless steel: Monte-Carlo simulations and in-situ temperature measurements,” *Vacuum*, **142**, pp. 114–122.

[82] Yan, W., Ge, W., Smith, J., Lin, S., Kafka, O. L., Lin, F., and Liu, W. K., 2016, “Multi-scale modeling of electron beam melting of functionally graded materials,” *Acta Mater.*, **115**, pp. 403–412.

[83] Ilican, S., Caglar, M., and Caglar, Y., 2007, “Determination of the Thickness and Optical Constants of Transparent Indium-Doped ZnO Thin Films by the Envelope Method,” *Materials Science-Poland*, **25**(3), pp. 709–718.

[84] Yan, W., Smith, J., Ge, W., Lin, F., and Liu, W. K., 2015, “Multiscale modeling of electron beam and substrate interaction: a new heat source model,” *Comput. Mech.*, **56**(2), pp. 265–276.

[85] Lisiecki, A., 2019, “Study of Optical Properties of Surface Layers Produced by Laser Surface Melting and Laser Surface Nitriding of Titanium Alloy,” *Materials*, **12**, 3112, pp. 1–14.

[86] Dilip, J. J. S., Zhang, S., Teng, C., Zeng, K., Robinson, C., Pal, D., and Stucker, B., 2017, “Influence of processing parameters on the evolution of melt pool, porosity, and microstructures in Ti-6Al-4V alloy parts fabricated by selective laser melting,” *Prog. Addit. Manuf.*, **2**(3), pp. 157–167.

[87] Matilainen, V., Piili, H., Salminen, A., and Nyrhilä, O., 2015, “Preliminary Investigation of Keyhole Phenomena during Single Layer Fabrication in Laser Additive Manufacturing of Stainless Steel,” *Phys. Procedia*, **78**, pp. 377–387.

[88] <https://amadaweldtech.com/blog/laser-welding-modes-conduction-transition-keyhole-welding/> Accessed on 11/20/2020.

[89] King, W. E., Barth, H. D., Castillo, V. M., Gallegos, G. F., Gibbs, J. W., Hahn, D. E., Kamath, C., and Rubenchik, A. M., 2014, “Observation of keyhole-mode laser melting in laser

powder-bed fusion additive manufacturing,” *J. Mater. Process. Technol.*, **214**(12), pp. 2915–2925.

[90] Bird, R. B., Stewart, W. E., and Lightfoot, E.N., 2006, “Transport Phenomena,” 2<sup>nd</sup> ed., John Wiley & Sons, New York.

[91] Schlichting, H., 1975, “Boundary Layer Theory,” 7<sup>th</sup> ed, McGraw-Hill, New York.

[92] Shrestha, S., and Chou, K., 2017, “A build surface study of Powder-Bed Electron Beam Additive Manufacturing by 3D thermo-fluid simulation and white-light interferometry,” *Int. J. Mach. Tools Manuf.*, **121**, pp. 37–49.

[93] Esen, A., and Kutluay, S., 2004, “A numerical solution of the Stefan problem with a Neumann-type boundary condition by enthalpy method,” *Appl. Math. Comput.*, **148**(2), pp. 321–329.

[94] Shen, H., Yan, J., and Niu, X., 2020, “Thermo-Fluid-Dynamic Modeling of the Melt Pool during Selective Laser Melting for AZ91D Magnesium Alloy,” *Materials*, **13**(18): 4157, pp. 1–19.

[95] Pei, Y. T., Ocelik, V., and Hosson, J. T. M. D., 2002, “SiCp/Ti6Al4V functionally graded materials produced by laser melt injection,” *Acta Mater.*, **50**(8), pp. 2035–51.

[96] Ogoh, W., and Groulx, D., 2010, “Stefan’s problem: validation of a one-dimensional solidliquid phase change heat transfer process,” *Proc. COMSOL Conference*, October 7–9, 2010, Boston, MA, pp.1–6.

[97] Chen, Z., Wu, X., Tomus, D., and Davies, C. H. J., 2018, “Surface roughness of Selective Laser Melted Ti-6Al-4V alloy components,” *Addit. Manuf.*, **22**, pp. 91–103.

[98] Qiu, C., Panwisawas, C., Ward, M., Basoalto, H. C., Brooks, J.W., and Attallah, M. M., 2015, “On the role of melt flow into the surface structure and porosity development during selective laser melting,” *Acta Mater.*, **96**, pp. 72–79.

[99] Zhou, X., Li, K., Zhang, D., Liu, X., Ma, J., Liu, W., and Shen, Z., 2015, “Textures formed in a CoCrMo alloy by selective laser melting,” *J. Alloys Compd.*, **631**, pp. 153–164.

[100] Ghia, U., Ghia, K. N., and Shin, C. T., 1982, “High-Re Solutions for Incompressible Flow Using the Navier-Stokes Equations and a Multigrid Method,” *J. Comput. Phys.*, **48**, pp. 387–411.

[101] Burggraf, O. F., 1966, “Analytical and Numerical Studies of the Structures of Steady Separated Flows,” *J. Fluid Mech.*, **24**, pp. 113–151.

[102] Bozeman, J. D. and Dalton, C., 1973, “Numerical Study of Viscous Flows in a Cavity,” *J. Comput. Phys.*, **12**, pp. 348–363.

[103] Akyuzlu, K. M., 2017, “A Numerical and Experimental Study of Laminar Unsteady Lid-Driven Cavity Flows,” *Proc. ASME 2017 International Mechanical Engineering Congress and Exposition*, Vol. 7, Fluids Engineering. Tampa, Florida, USA. Nov 3–9, 2017, IMECE2017-70145, pp. 1–11.

[104] Rahman, M. S., and Chakravarty, U. K., 2019, “Characterizations of the Paper-Based Microfluidic Devices Used for Detecting Fentanyl and Related Synthetic Opioids,” *Proc. ASME 2019 International Mechanical Engineering Congress and Exposition*. Vol. 1, Advances in Aerospace Technology, Salt Lake City, Utah, Nov 11–14, 2019, IMECE2019-11581, pp. 1–9.

## **Vita**

Mr. M Shafiqur Rahman was born in the city of Brahmanbaria, Bangladesh. He completed his Bachelor of Science in Mechanical Engineering in 2011 from the Islamic University of Technology, Bangladesh. After graduation, Mr. Rahman joined the People's University of Bangladesh, Dhaka, Bangladesh, and served there up to May 2012 as a Lecturer in Mechanical Engineering. Then he joined Primeasia University in June 2012 and worked as a lecturer in the Department of Textile Engineering for over two years before coming to the USA. In Fall 2014, Mr. Rahman joined the University of New Orleans to pursue his Ph.D. in Mechanical Engineering. He received his Master of Science and Ph.D. degrees in Mechanical Engineering from the University of New Orleans in August 2016 and December 2020, respectively. His area of research covers additive manufacturing, heat transfer, computational fluid dynamics, and solid mechanics.